

2001

# An experimental and numerical investigation of stator-rotor interactions in a transonic compressor

Steven Ernest Gorrell  
*Iowa State University*

Follow this and additional works at: <https://lib.dr.iastate.edu/rtd>

 Part of the [Mechanical Engineering Commons](#)

## Recommended Citation

Gorrell, Steven Ernest, "An experimental and numerical investigation of stator-rotor interactions in a transonic compressor" (2001).  
*Retrospective Theses and Dissertations*. 642.  
<https://lib.dr.iastate.edu/rtd/642>

This Dissertation is brought to you for free and open access by the Iowa State University Capstones, Theses and Dissertations at Iowa State University Digital Repository. It has been accepted for inclusion in Retrospective Theses and Dissertations by an authorized administrator of Iowa State University Digital Repository. For more information, please contact [digirep@iastate.edu](mailto:digirep@iastate.edu).

## **INFORMATION TO USERS**

**This manuscript has been reproduced from the microfilm master. UMI films the text directly from the original or copy submitted. Thus, some thesis and dissertation copies are in typewriter face, while others may be from any type of computer printer.**

**The quality of this reproduction is dependent upon the quality of the copy submitted. Broken or indistinct print, colored or poor quality illustrations and photographs, print bleedthrough, substandard margins, and improper alignment can adversely affect reproduction.**

**In the unlikely event that the author did not send UMI a complete manuscript and there are missing pages, these will be noted. Also, if unauthorized copyright material had to be removed, a note will indicate the deletion.**

**Oversize materials (e.g., maps, drawings, charts) are reproduced by sectioning the original, beginning at the upper left-hand corner and continuing from left to right in equal sections with small overlaps.**

**Photographs included in the original manuscript have been reproduced xerographically in this copy. Higher quality 6" x 9" black and white photographic prints are available for any photographs or illustrations appearing in this copy for an additional charge. Contact UMI directly to order.**

**ProQuest Information and Learning  
300 North Zeeb Road, Ann Arbor, MI 48106-1346 USA  
800-521-0600**

**UMI<sup>®</sup>**



## **NOTE TO USER**

**This reproduction is the best copy available.**

UMI<sup>®</sup>



**An Experimental and Numerical Investigation of Stator-Rotor Interactions in  
a Transonic Compressor**

**by**

**Steven Ernst Gorrell**

**A dissertation submitted to the graduate faculty  
in partial fulfillment of the requirements for the degree of  
DOCTOR OF PHILOSOPHY**

**Major: Mechanical Engineering**

**Program of Study Committee:  
Theodore H. Okiishi, Major Professor  
R. Ganesh Rajagopalan  
Gerald M. Colver  
Ron M. Nelson  
Bruce R. Munson  
William W. Copenhaver**

**Iowa State University**

**Ames, Iowa**

**2001**

**UMI Number: 3034186**

**UMI<sup>®</sup>**

---

**UMI Microform 3034186**

**Copyright 2002 by ProQuest Information and Learning Company.  
All rights reserved. This microform edition is protected against  
unauthorized copying under Title 17, United States Code.**

---

**ProQuest Information and Learning Company  
300 North Zeeb Road  
P.O. Box 1346  
Ann Arbor, MI 48106-1346**

**Graduate College  
Iowa State University**

**This is to certify that the Doctoral Dissertation of  
Steven Ernest Gorrell  
has met the dissertation requirements of Iowa State University**

Signature was redacted for privacy.

**Major Professor**

Signature was redacted for privacy.

**For the Major Program**

## TABLE OF CONTENTS

<b>NOMENCLATURE</b>	<b>v</b>
<b>ACKNOWLEDGMENTS</b>	<b>viii</b>
<b>ABSTRACT</b>	<b>x</b>
<b>INTRODUCTION</b>	<b>1</b>
<b>Subsonic Rotor-Stator Interactions</b>	<b>3</b>
<b>Stator-Rotor Interactions</b>	<b>5</b>
<b>Numerical Modeling of Stator-Rotor Interactions</b>	<b>6</b>
<b>Value of Present Research</b>	<b>7</b>
<b>STAGE MATCHING INVESTIGATION RIG</b>	<b>9</b>
<b>Compressor Stage</b>	<b>10</b>
<b>Wake Generators</b>	<b>11</b>
<b>Test Facility</b>	<b>13</b>
<b>Test Article Instrumentation</b>	<b>15</b>
<b>Aliasing</b>	<b>16</b>
<b>Experimental Repeatability</b>	<b>20</b>
<b>Wake Generator/Rotor Only Configuration</b>	<b>22</b>
<b>WAKE CALIBRATION</b>	<b>24</b>
<b>Wake Calibration Instrumentation</b>	<b>24</b>
<b>Wake Calibration Procedure</b>	<b>27</b>
<b>Wake Calibration Results</b>	<b>30</b>
<b>SMI AND WAKE GENERATOR/ROTOR ONLY PERFORMANCE</b>	<b>40</b>
<b>SMI Results</b>	<b>40</b>
<b>Part Speed SMI Performance</b>	<b>42</b>
<b>Wake Generator/Rotor Only Results</b>	<b>46</b>
<b>Performance Summary</b>	<b>49</b>
<b>Wake Recovery Analysis</b>	<b>54</b>
<b>STEADY-STATE DATA ANALYSIS</b>	<b>56</b>
<b>Loss Overview</b>	<b>56</b>
<b>Flow Capacity Experiment</b>	<b>56</b>
<b>Wake Generator/Rotor Only Analysis</b>	<b>59</b>
<b>Contour Plots of Pressure Ratio and Efficiency</b>	<b>62</b>
<b>NUMERICAL APPROACH</b>	<b>70</b>
<b>MSU-TURBO</b>	<b>70</b>

Phase-Lag Boundary Conditions	71
Initial Solution	71
Meshes	72
Flow Field Construction	73
SMI Simulations	74
Solution Convergence	75
<b>NUMERICAL RESULTS</b>	<b>79</b>
Time-Average Results	79
Time-Average Loss Comparison	82
Time-Accurate Results	83
Close Spacing Loss	85
Far Spacing Loss	88
Static Pressure Contours	88
Far Spacing Static Pressure	94
Close and Far Spacing Comparison	96
Numerical Model Improvements	98
<b>BLADE-ROW INTERACTION LOSS PRODUCTION</b>	<b>99</b>
Relationship Between Loss and Wake Generator Pressure Wave	99
Wake Generator Unsteady Static Pressure Measurements	100
Spanwise Extent of Loss Production	104
29% Span Analysis	107
Design Implications	110
Additional Research	112
<b>CONCLUSIONS</b>	<b>115</b>
<b>APPENDIX A. CTA RAKE DRAWINGS</b>	<b>119</b>
<b>APPENDIX B. 24 WAKE GENERATOR PERFORMANCE PROFILES</b>	<b>122</b>
<b>APPENDIX C. MOVIES FROM MSU-TURBO SIMULATIONS</b>	<b>125</b>
<b>REFERENCES</b>	<b>127</b>

**NOMENCLATURE**

$a_\infty$	free stream speed of sound, $a_\infty = \sqrt{\gamma RT_\infty}$
$a_x$	axial chord
$c$	chord
$C_p$	specific heat at constant pressure
$D$	diffusion factor
$g_c$	constant, $g_c = 32.174 \frac{\text{lbm} - \text{ft}}{\text{lbf} - \text{s}^2}$
$H_{\text{inlet}}$	total enthalpy at compressor inlet
$H_2$	total enthalpy at compressor exit
$H_{2s}$	isentropic total enthalpy at compressor exit
$\text{hp}$	horsepower
$\text{in}$	inches
$\text{lbm}$	pounds mass
$\text{lbf}$	pounds force
$\text{LE}$	leading edge
$M$	Mach number
$M_{\text{in}}$	Mach number at wake generator inlet
$M_{\text{REL}}$	rotor relative Mach number
$M_{\text{wave}}$	wake generator pressure wave Mach number, $M_{\text{wave}} = \frac{V_{\text{wave}} + V_\infty}{a_\infty}$
$N_c$	corrected speed
$p$	static pressure

$P_{inlet}$	static pressure measured at inlet
$P$	total pressure
$P_{inlet}$	total pressure measured at inlet
$P_{rake}$	total pressure measured by wake calibration rake
$PR$	pressure ratio
$P_{ref}$	reference total pressure, $P_{ref} = 14.694 \text{ lbf/in}^2$
$R$	gas constant
$s$	seconds or entropy
$t$	static temperature
$t_{\infty}$	free stream static temperature
$T_{\infty}$	free stream total temperature
$TE$	trailing edge
$T_{ref}$	reference total temperature, $T_{ref} = 518.688 \text{ }^{\circ}\text{R}$
$u$	axial component of velocity
$v$	tangential component of velocity
$V$	velocity
$V_{\infty}$	free stream velocity
$w$	radial component of velocity
$\gamma$	ratio of specific heats, $\gamma = C_p/C_v$
$\eta$	isentropic efficiency, $\eta = \frac{H_{2s} - H_{inlet}}{H_2 - H_{inlet}}$
$\rho$	density

$\rho u \Delta s / C_p$     **loss parameter**

$\omega$             **mass average loss coefficient**

## **ACKNOWLEDGMENTS**

The research reported in this dissertation was accomplished with the help and support of many individuals. Without the love and sacrifices made by my wife Angie I would have never finished the task. I also wish to acknowledge the support and encouragement offered by my parents, brother and sisters, and in-laws. The patience and encouragement offered by my Major Professor, Ted Okiishi, is greatly appreciated. His suggestions to seek input from other experts as well as his own technical insights improved the research effort substantially.

Many individuals contributed to the research supporting this dissertation. From the CARL group at Wright-Patterson AFB I would like to recognize Dr. Herb Law, Robert Wirrig, Ron Berger, Terry Norris, Bill Ullman, and Chris Blackwell for their assistance in gathering the experimental data. The use of the MSU-TURBO code contributed immensely to the quality of this dissertation. I would like to thank Dr. Dale Van Zante from NASA Glenn Research Center, Dr. J. P. Chen from Mississippi State University, and Dave Car from CARL for their help in getting MSU-TURBO running and in post-processing and interpreting the data. The support and assistance from the Naval Oceanographic Office Major Shared Resource Center (NAVO MSRC) where the code was run is also greatly appreciated.

Many of the ideas presented in the dissertation were arrived at after discussion with others that showed interest in this research. I would like to recognize Dr. Steve Puterbaugh, Dr. Bill Copenhaver, Dr. Greg Bloch, and Dave Car from the CARL group, from NASA Glenn Research Center Dr. John Adamczyk, Dr. Tony Strazisar, Dr. Randy Chriss, and Dr. Dale Van Zante, and my Program of Study Committee. In conclusion I would like to thank the Propulsion Directorate management and my Branch Chief, Marv Stibich,

**for their support in allowing me to pursue and complete the Doctorate degree.**

**ABSTRACT**

Although it is known that the flow field in a turbomachine is unsteady, current design tools do not explicitly account for it. One area of current interest is to evaluate the impact of unsteady flows on turbomachine performance in order to determine if an understanding of unsteady fluid dynamics can be used to improve performance and is it advantageous for this unsteadiness to be accounted for in the design of turbomachine components.

In this dissertation blade-row interactions between an upstream stator row and downstream transonic rotor row are investigated. Experimental data acquired from a transonic compressor rig is presented that documents how changes in axial blade-row spacing and stator solidity affect compressor performance. Unsteady CFD simulations of the compressor are used to show what part of the compressor is responsible for performance changes and how unsteady fluid mechanics cause these changes.

Mass flow rate, pressure ratio, and efficiency all decreased as the spacing between the wake generator and rotor was reduced. Reductions as much as 3.29% in pressure ratio and 1.26 points efficiency were observed as spacing between the blade-row was decreased from far to close. The number of blades in the wake generator blade-row also affected the stage performance. The higher the wake generator blade-row solidity the lower the pressure ratio, efficiency, and mass flow rate. The experimental data suggest the drop in performance is a result of increased loss production due to blade-row interactions.

A numerical simulation using the code MSU-TURBO was able to account for the change in efficiency observed experimentally between far and close spacing at an operating point near peak efficiency. Analysis of the simulations and high-response static pressure measurements acquired on

the stator blade surface reveal the fluid dynamics of this additional loss producing mechanism. At close spacing the rotor bow shock is actually chopped by the stator trailing edge. The shock diffracts around the trailing edge forming a pressure wave on the upper surface of the stator that propagates upstream until it weakens. In the reference frame relative to this pressure wave, the flow is supersonic and a moving shock wave exists that produces an entropy rise. The lower efficiency, pressure ratio, and mass flow rate measured at close spacing is a result of this extra loss. The magnitude of loss production is affected by the strength of the bow shock at the location it interacts with the trailing edge of the stator. Furthermore, the more blades present in the stator the more loss producing interactions take place. At far spacing the rotor bow shock has degenerated into a bow wave where it interacts with the stator trailing edge and is not chopped, therefore no pressure wave forms on the wake generator upper surface.

The majority of research on blade-row spacing has focused on the effect of rotor-stator axial gap on compressor performance. This research shows that stator-rotor interactions are of equal if not greater importance to the performance of a transonic compressor. The investigation has identified an unsteady flow mechanism that affects the performance of transonic compressors and should be taken into account in the design process. This flow phenomena produces additional losses when the rotor bow shock interacts strongly with the trailing edge of the upstream stator row which occurs when the axial gap between the two rows is too small.

## **INTRODUCTION**

**An understanding of the inherent unsteady flow through a turbomachine is necessary in order to comprehend and overcome many of the present day technical challenges encountered during the design and operation of improved high performance gas turbine engines. For example, unsteady flow phenomena are known to play a primary role in setting gas turbine engine operating limits such as stall inception and in producing aeromechanical excitations resulting in high cycle fatigue and noise.**

**One area of current interest is to evaluate the impact of unsteady flows on turbomachine performance. The emphasis of this research has been to determine if an understanding of unsteady fluid dynamics can be used to improve performance and is it advantageous for this unsteadiness to be accounted for in the design of turbomachine components. To answer these questions it must be determined if potential performance gains are significant enough to warrant increased complexity in the design process and what level of design tool is necessary to account for unsteady flows in the design process.**

**Although it is known that the flow field in a turbomachine is unsteady, design tools do not explicitly account for it. Multistage axisymmetric flow models assume the incoming flow to a blade row is a mixed-out average of the flow exiting the preceding blade row and that potential effects between blade rows are negligible. These models use empirical correlations based on an engine company's design experience to account for the effects of unsteady flow. The average passage model developed by Adamczyk [1] does account for the presence of neighboring blade rows through a time-average flow field representation. Still, its accuracy is dependent on the models used to account for the effects of the unsteady flow environment on the average-passage flow field. The only method that directly simulates the unsteady flow field in a turbomachine is**

that which models the Reynolds averaged Navier-Stokes equations. However, the computer resources required to obtain a solution make this option impractical from a designers standpoint for the time being. For a historical perspective of multistage turbomachine design models see Adamczyk [2].

This research effort will evaluate and analyze the effects of blade-row interactions on the performance of an embedded transonic compressor stage. More specifically, the interactions between an upstream stator row and downstream transonic rotor row are investigated. The report will proceed by presenting a background on the subject of blade-row interactions and then describe the test article and instrumentation used to obtain the data. Experimental data acquired from the transonic compressor test rig that documents how changes in axial blade-row spacing affect compressor performance are then presented. The unsteady CFD code used to model the test compressor is then described followed by analysis to show what part of the compressor is responsible for performance changes and how unsteady fluid mechanics cause these changes. The report ends with conclusions on the role of blade-row interactions on transonic compressor performance.

There are many sources of unsteady flow in a transonic compressor. Some examples are blade-row interactions (both wake-blade and potential), secondary flows such as corner vortices, passage vortices, and tip clearance flows, and trailing edge vortex shedding. The interaction between two adjacent blade rows is considered the most influential of these sources. This section will review pertinent research already accomplished in the area of blade-row interactions. The review will focus on the topics of subsonic rotor-stator interactions, stator-rotor interactions, and numerical modeling of stator-rotor interactions.

### **Subsonic Rotor-Stator Interactions**

Experimental results from a four-stage compressor published by Smith [3] and another multistage compressor experiment discussed by Mikolajczak [4] demonstrate that reducing the axial gap between blade rows in multistage compressors increased the pressure ratio and isentropic efficiency for a given flow coefficient. Both of these compressors were low-speed with no shocks present. In each case efficiency was increased by one point when the blade-rows were moved from far spacing to close spacing. Smith [5,6] proposed that the performance gains were partially a result of inviscid wake defect reduction through stretching and introduced the concept of wake recovery. Smith has described wake recovery as the process that occurs when a viscous wake is flattened (or stretched) reversibly while passing through a blade row, thus avoiding some of the entropy rise that occurs when a wake is flattened entirely by viscous dissipation. The end result is a reduction of wake mixing loss.

Since Smith's [6] description of wake recovery others have performed research that has helped understand the concept of wake recovery in rotor-stator interactions. Deregai and Tan [7] were able to simulate wake stretching with a numerical model, which showed that if rotor wakes are mixed out after the stator passage rather than before the overall static pressure rise increases and the mixing loss decreases. Figure 1 from reference [7] illustrates the concept of wake stretching through a stator blade.

Adamczyk [8] applied a linear model to a two-dimensional cascade and concluded that for highly unsteady flows the wake recovery process is a function of flow turning across the blade-row (airfoil circulation) and related to the vorticity of the incoming wakes. Furthermore it was shown that the potential existed to reduce wake mixing loss by as much as 70% through wake recovery. Building on ideas presented by Adamczyk [8], Van Zante et al. [9] developed a model to evaluate the relative contribution of viscous

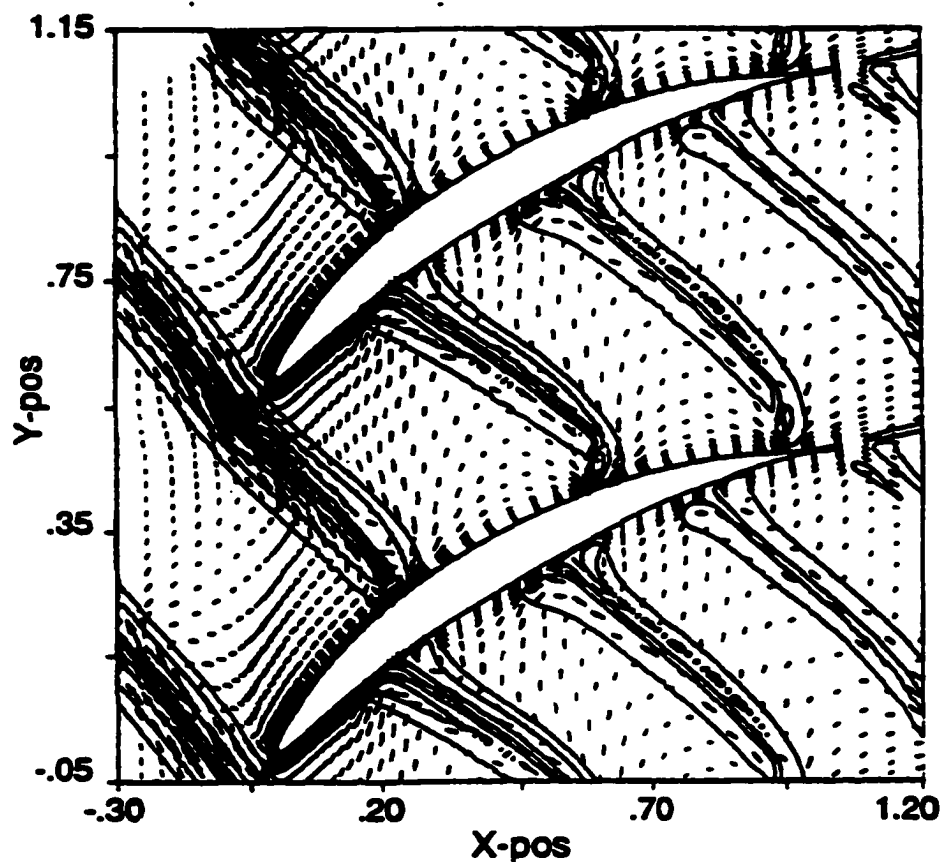


Figure 1. Wake Stretching Through a Stator Blade [7]

dissipation and inviscid stretching to the decay of a wake through a blade-row. This model was applied to a high-speed compressor stage and showed that for the rotor wake passing through the stator, wake stretching was the dominant source of wake decay with viscous dissipation playing a minor role. It was concluded that to reduce the amount of mixing loss between blade-rows it would be beneficial to minimize axial spacing in order to capture the rotor wake sooner, thus allowing the rotor wake to mix out more by means of wake stretching than viscous dissipation. However it was assumed that closer spacing would not increase losses due to potential field interactions or wake-blade interactions. In order to account for the effects of recovery in turbomachinery analysis van de Wall [10] developed a deterministic stress model for the transport of upstream vortical

disturbances through a downstream blade row. Application of this model has shown that both inviscid and viscous mechanisms act to reduce the time-averaged unsteady kinetic energy and both need to be accounted for in order to accurately model the recovery process. The model also showed that the potential for reduced mixing loss still exists when the compressor stage is at an off-design condition.

### **Stator-Rotor Interactions**

There has been some research on stator-rotor interaction in turbines that has produced findings applicable to compressors. Rose and Harvey [11] developed a simple model to estimate the ratio of work done on a stator wake to the work done on the freestream as it flows through a rotor. This ratio is defined as the differential work coefficient. Since more work is done on the stator wake than the freestream, the authors showed that the rotordynamic work process reduces the wake total pressure defect. It was also shown that more work is done on a wake if it is of low total pressure, which in turn reduces the mixing loss. Rose and Harvey [11] propose that the greater the total pressure deficit of the wake the greater the reduction in mixing loss and showed a reduction of 88% in wake mixing loss in their application. Since a stator wake will have greater wake depth the closer it is to the downstream rotor their results also imply that reducing blade row spacing would be advantageous to compressor performance. Not surprisingly, Rose and Harvey [11] suggest that their mechanism of differential work may be the same as wake stretching presented in references [5-10].

Experimental blade-row interaction studies in transonic compressors have focused on visualizing and quantifying the interaction mechanisms present in the flow field. Ottavy et al [12, 13] made laser two-focus anemometer measurements between an IGV and transonic rotor. The measurements and analysis concentrated on the interaction between the rotor bow shock and the wake shed from the IGV. It was concluded that the

shock wave had a much larger effect on the wake than the remainder of the flow. Upstream of the shock wave the wake depth was reduced and the wake was overturned as a result of an expansion zone in the flow due to the curvature of the rotor blade suction surface. Downstream of the shock wave the wake deficit increased and the wake was underturned.

Blade-row interactions are known to play a major role in producing forcing functions that contribute to high cycle fatigue. Sanders and Fleeter [14] have made both Particle Image Velocimetry (PIV) and blade surface static pressure measurements in the IGV passage upstream of a transonic rotor. Their results showed that the flow field was highly unsteady due to the reflection and diffraction of the rotor bow shock in the IGV passage. The shock interaction with the IGV trailing edge caused the trailing edge stagnation point to move periodically from the pressure to suction surfaces of the IGV. This interaction accounted for peak-to-peak fluctuations in static pressure as large as 60% of the inlet total pressure. It was also shown that decreasing the axial spacing from 62.9% to 41.4% IGV chord increased the peak-to-peak static pressure fluctuations by 30%.

#### **Numerical Modeling of Stator-Rotor Interactions**

A limited amount of numerical studies of transonic stator-rotor interactions has been published. It should be noted that unsteady Navier-Stokes codes are still in their infancy with little data available for validation. The turbulence model used can also have a significant impact on the computed results. Liamis et al [15] performed a simulation of an IGV-rotor combination with a quasi three-dimensional Navier-Stokes solver. Their results showed that the rotor bow shock interaction with the IGV wake had a large influence on the IGV instantaneous outlet angle and flow velocities. Variation of 8 degrees in IGV outlet angle and 80 m/s in velocity were observed. It was also noted that the detached rotor bow shock became weaker upstream finally degenerating into a pressure wave in the IGV passage and reflected at the IGV blade surface.

Eulitz et al [16] performed a simulation of a stator-rotor interaction solving both inviscid and viscous equations in a two-dimensional plane. They showed that the rotor shock interaction with the upstream stator and its subsequent reflections was visible with the Euler (inviscid) solution. However the viscous solution shows additional features such as flow separation on the stator pressure surface due to the shock interaction with the stator blade boundary layer. The separation forms and disappears in conjunction with the blade passing period.

Arnone and Pacciani [17] compared steady and time-averaged computations of a rotor and stator stage. They found that the steady solution overpredicted the pressure ratio and adiabatic efficiency and attributed this to spurious shock reflections at the interface boundary. Their solution was to increase the axial gap of the steady solution after which the reflections decreased and the predicted performance was closer to the time-averaged solution. Although the authors found the discrepancy a result of numeric boundary conditions it never-the-less demonstrated that bow shock strength could play a role in the severity of transonic stator-rotor interactions.

### **Value of Present Research**

Low speed experimental results have shown that decreasing blade-row spacing in a multistage compressor improves performance. Analytical studies on the subsonic flow of a rotor wake through a stator have demonstrated that the process of inviscid wake recovery through stretching is responsible for the increased performance. Transonic stator-rotor experimental and numerical research has shown that blade-row interactions are dominated by the rotor bow shock and its interaction with the shed wake and blade surface of the upstream stator. The research presented in this report continues the analysis of blade-row interaction by presenting for the first time the effect of stator-rotor axial spacing on mass flow rate, pressure ratio, and efficiency in a modern technology transonic compressor.

The majority of research on blade-row spacing has focused on the effect of rotor-stator axial gap on compressor performance. This research will prove that stator-rotor interactions are of equal if not greater importance to the performance of a transonic compressor. In addition the investigation will identify an unsteady flow mechanism that affects the performance of transonic compressors and should be taken into account in the design process. This flow phenomena produces additional losses when the rotor bow shock interacts strongly with the trailing edge of the upstream stator row which occurs when the axial gap between the two rows is too small.

## STAGE MATCHING INVESTIGATION RIG

All experimental and numerical research was performed on the U. S. Air Force's Stage Matching Investigation (SMI) rig. It is a high-speed, highly-loaded compressor consisting of three blade-rows: a wake generator, rotor, and stator as shown in Figure 2. The rig was designed such that the wake generator to rotor axial spacing and the wake generator blade count could be varied. The wake generator spacings are denoted as "close", "mid", and "far". The mid and far spacings represent typical axial gaps found in operational fans and compressors. However, the current generation of high performance fans and compressors are being designed with the goal of minimizing blade-row spacing in order to reduce compressor length and thus weight and increase performance. The wake generator blade count can be set to 12, 24, or 40, or the rig can be run without any wake generators (identified as the "clean inlet" configuration). Table 1 gives the wake generator to rotor axial spacings normalized by the wake generator chord.

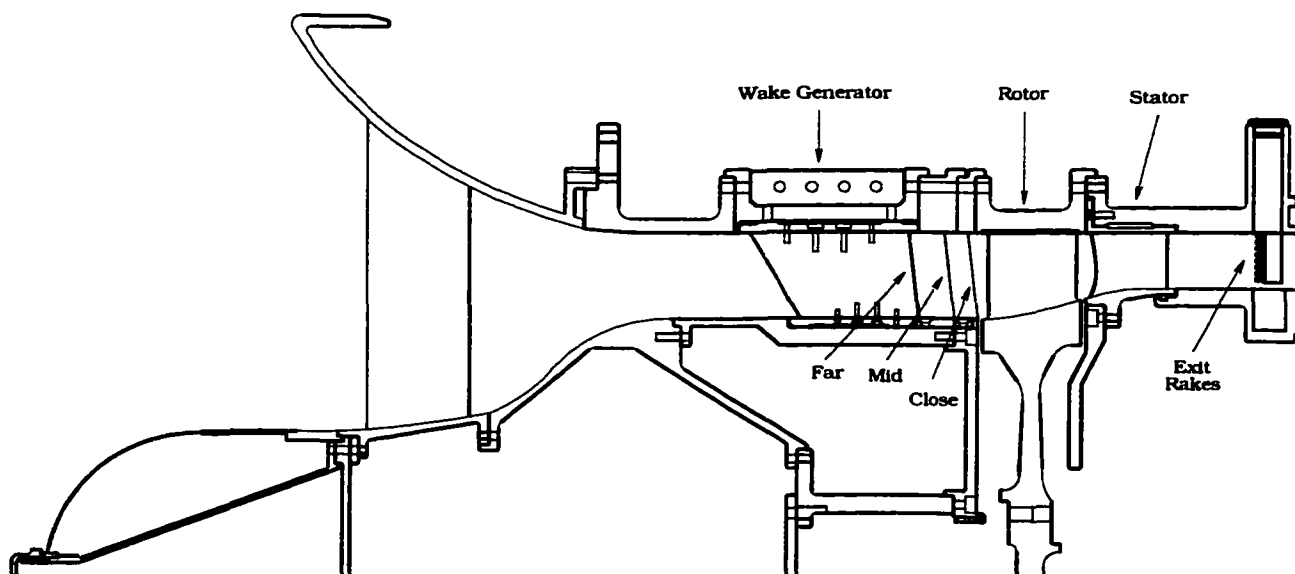


Figure 2. Stage Matching Investigation Rig Layout

**Table 1. Wake Generator-Rotor Axial Spacing**

Spacing	ax/c (mean)	ax/c (hub)	ax/c (tip)
Close	0.13	0.10	0.14
Mid	0.26	0.26	0.26
Far	0.55	0.60	0.52

ax = axial spacing

c = wake generator chord

### Compressor Stage

The rotor and stator were designed by Law and Wennerstrom [18]. A summary of the SMI stage aerodynamic design parameters is given in Table 2 and photographs of the rotor and stator are shown in Figure 3.

**Table 2. SMI Aerodynamic Design Parameters**

PARAMETER	ROTOR	STATOR
Number of Airfoils	33	49
Aspect Ratio - Average	0.961	0.892
Inlet Hub/Tip Ratio	0.750	0.816
Flow/Annulus Area, lbm/sec	40.000	--
Flow/Unit Area, lbm/sec/ft <sup>2</sup>	17.502	--
Flow rate, lbm/sec	34.460	--
Tip Speed, Corrected ft/sec	1120	--
M <sub>REL</sub> LE Hub	0.963	0.820
M <sub>REL</sub> LE Tip	1.191	0.690
PR Rotor	1.880	--
$\eta_{iso}$ Rotor, %	93.5	--
PR Stage	--	1.840
$\eta_{iso}$ Stage, %	--	90.2
D Factor Hub	0.545	0.502

Table 2 (continued)

PARAMETER	ROTOR	STATOR
D Factor Tip	0.530	0.491
LE Tip Dia., in.	19.000	19.000
LE Hub Dia., in.	14.250	15.502
TE Tip Dia., in.	19.000	19.000
TE Hub Dia., in.	15.244	15.896

### **Wake Generators**

The purpose of the wake generators are to create wakes typically found in modern-technology, highly-loaded, low-aspect-ratio fan and compressor front stages. In general these wakes are turbulent and do not decay as rapidly as wakes from high-aspect-ratio stages with lower loading. The wake generators were designed with the intent of producing a two-dimensional representation of wakes measured at the exit of a high-pressure-ratio, low-aspect-ratio fan stage reported by Creason and Baghdadi [19]. A two-dimensional representation was desired in order to isolate the effect of different wake parameters during the experiment. Variations of the baseline wake generator design were available to change the wake depth, width, and shedding frequency if desired.

There are many sources of flow unsteadiness in fan and compressor middle stages but as presented in the background section the most influential are when the wakes shed from an upstream blade-row interact with a downstream blade-row. These wakes produce high frequency and periodic changes in inlet pressure, velocity, temperature, turbulence and incidence angle. Stator wakes are chopped and passed by the downstream rotor, affecting the rotor blade work and boundary layer characteristics. These wakes are also likely to affect the performance of other downstream blade-rows.

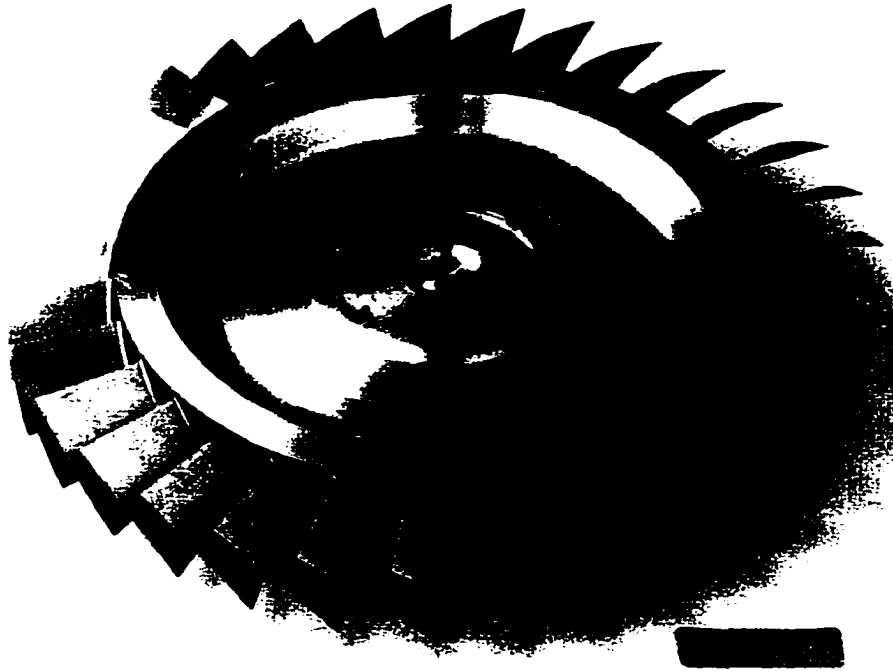


**Figure 3a. SMI Rotor**

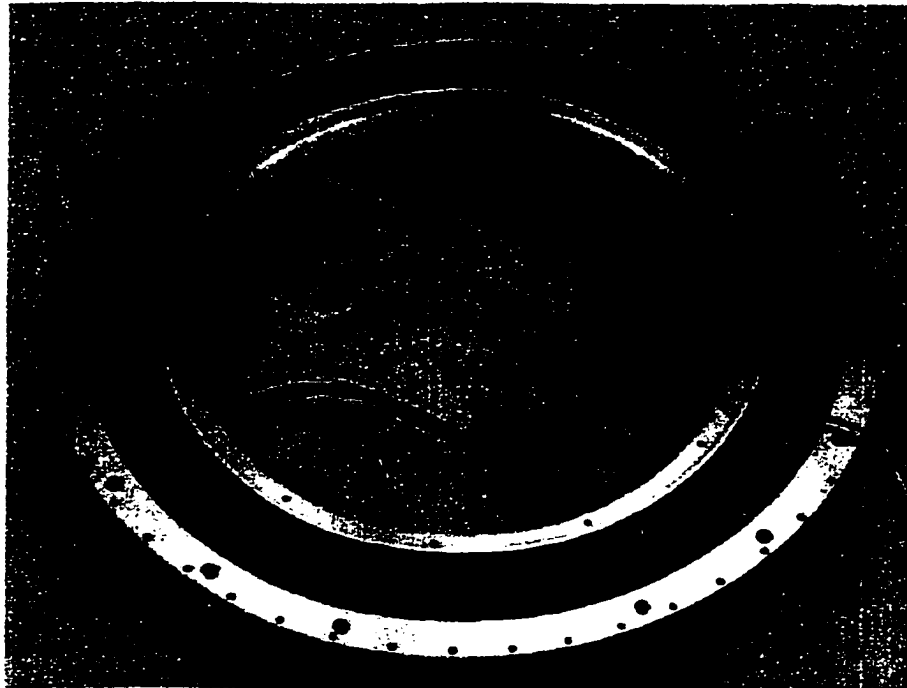


**Figure 3b. SMI Stator**

The wake generators are uncambered symmetric airfoils that do not turn the flow. As shown in Figure 4 the wake generators have a small leading edge and a blunt trailing edge. This shape creates a large base drag and no swirl. Solidity is held constant from hub to tip by varying the chord, the intent being to hold spanwise loss and wake width constant.

### **Test Facility**

The SMI rig was tested in the Compressor Aero Research Lab (CARL) located at Wright-Patterson Air Force Base, OH. A schematic of the facility is shown in Figure 5. The compressor is driven by a 2000 hp constant speed electric motor that is connected to an eddy-current coupling to control speed. Between the compressor drive shaft and the eddy-current coupling is a speed increaser that produces a maximum rotational speed of 21,500 rpm. The CARL facility may be run in either a closed or open loop configuration. Closed loop operation allows the test article to be run at reduced inlet pressures thus decreasing the required horsepower and eliminating some run restrictions resulting from high ambient air temperature. All testing of the SMI rig was done in the open loop

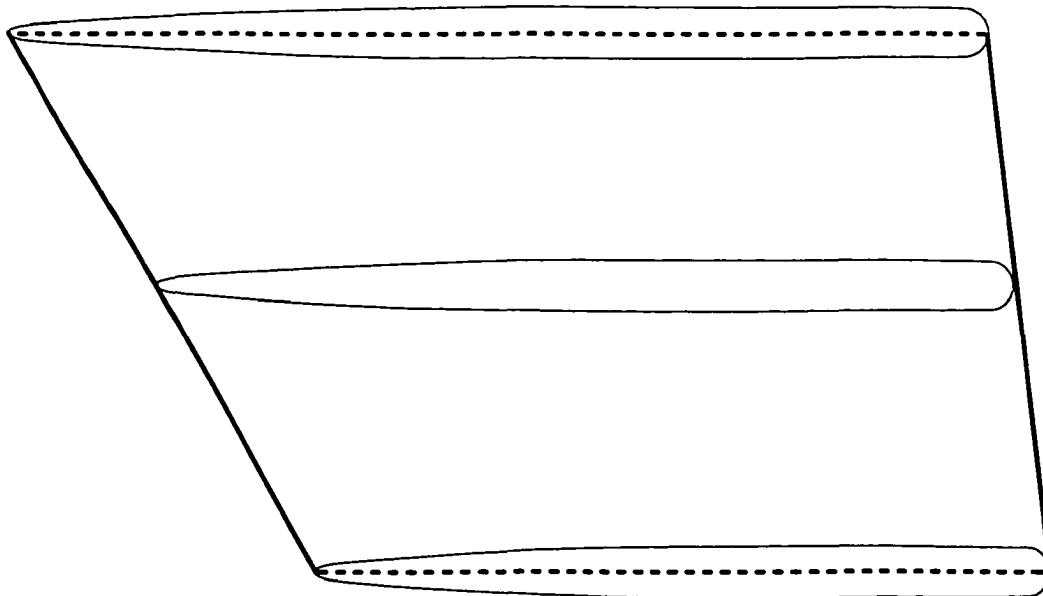


**Figure 4. Wake Generator Cross Section**

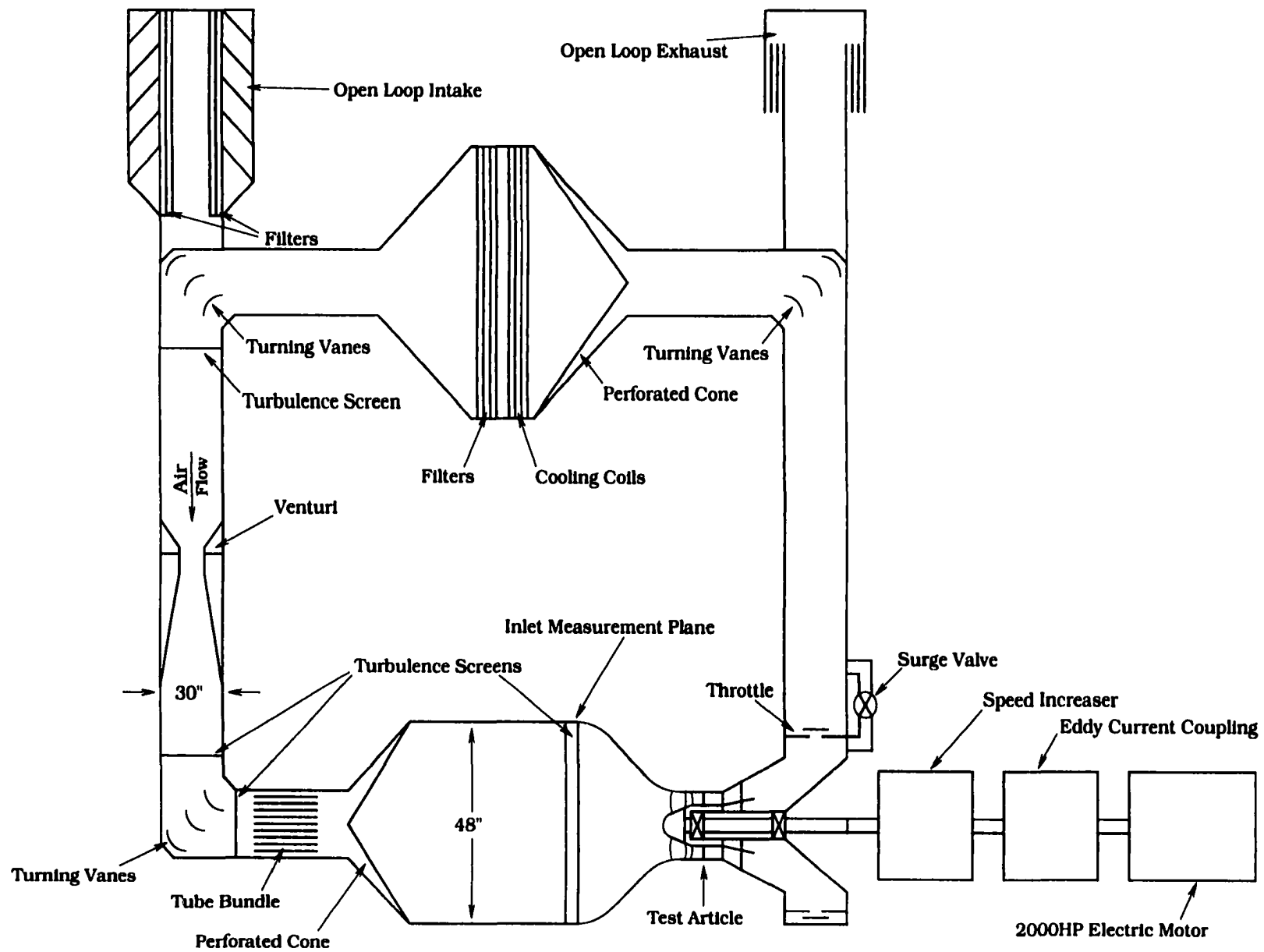
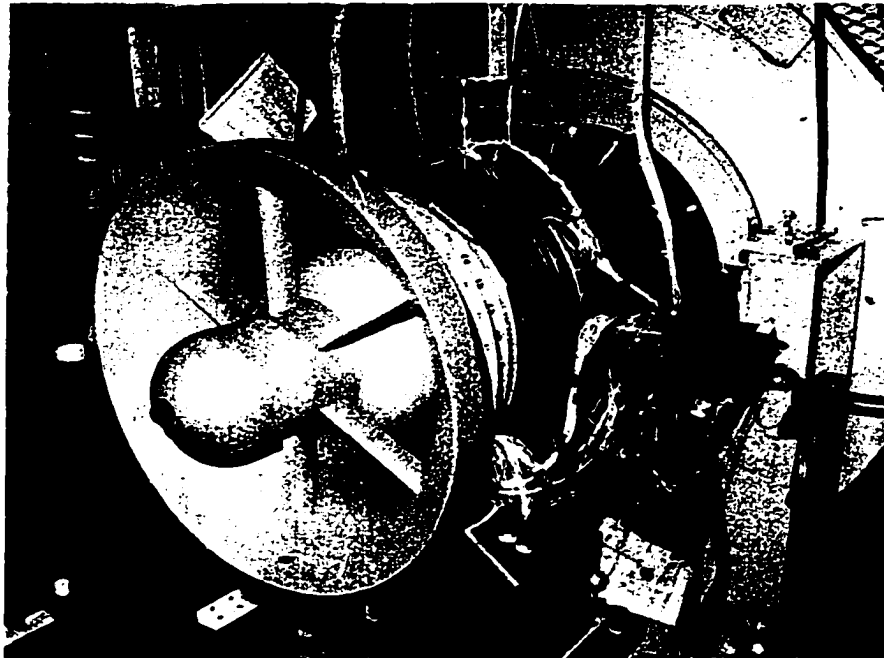


Figure 5. CARL Facility

configuration. The CARL facility can accommodate mass flow rates in the range of 15 to 65 lbm/s. The data acquisition hardware is state-of-the-art and capable of measuring steady-state temperatures and pressures and recording analog signals from high-response pressure transducers and strain gauges. The facility is also capable of making radial and circumferential traverse measurements in the compressor flowpath. A photograph of the SMI rig installed in the CARL facility is shown in Figure 6.

#### **Test Article Instrumentation**

Exit conditions measured to compute compressor performance (pressure ratio and efficiency) were obtained from an array of total pressure and total temperature probes. The exit instrumentation consisted of ten pressure and ten temperature rakes with eight probes distributed spanwise on each rake. From hub to case the distribution of each rake was 16.88, 27.96, 39.05, 50.13, 61.21, 72.29, 83.38, and 94.46 percent span. The rakes were located 2.1 stator axial chords downstream of the stator trailing edge (see Figure 2). Overall performance of the SMI rig was calculated by



**Figure 6. SMI Rig in the CARL Facility**

numerically averaging the 80 exit pressure and 80 exit temperatures. The rakes were positioned so that a pitchwise distribution in pressure and temperature could be established for a circumferentially periodic flow field. Placement was such that one stator pitch distribution (in ten percent increments) was measured. Figures 7, 8, and 9 describe the layout of exit probes along with their percent of stator and wake generator pitch locations.

Inlet conditions are determined from an array of 30 inlet thermocouples for temperature and inlet plenum static pressures for total pressure. Both of these measurements were taken from the inlet plenum location shown in Figure 5. Mass flow rate measurements are made from the venturi as shown in Figure 5.

### **Aliasing**

The exit rake configuration of the SMI rig is typical of that found in multistage compressor experiments. The only exceptions are that the SMI rig has probes at the stator exit instead of the stator leading edge and the quantity of the measurements is much greater than typically found in a multistage compressor test. Excluding wakes from blade rows upstream of the compressor, this measurement approach provides an excellent representation of the pressure and temperature field downstream of one stator row. With the assumption of circumferential uniformity the stage performance is accurately represented by this layout. However, if the exit rakes sense the influence of blade-rows upstream of the rotor, the upstream flow features will be aliased into the stator pitch results. Aliasing in this sense means that signal content from the wake generators is found in the stator pitch measurements that does not really exist. For this experiment, with 12- and 24-wake generators upstream of the rotor, the influence of two wake generators will be seen in the data measured for a single stator pitch. For example, Figure 8 shows that the pressure rakes for the 24 wake generator configuration are at 70, 10, 50, 90, 30 percent wake generator pitch and repeated again 70 10, 50, 90, 30 percent wake generator pitch

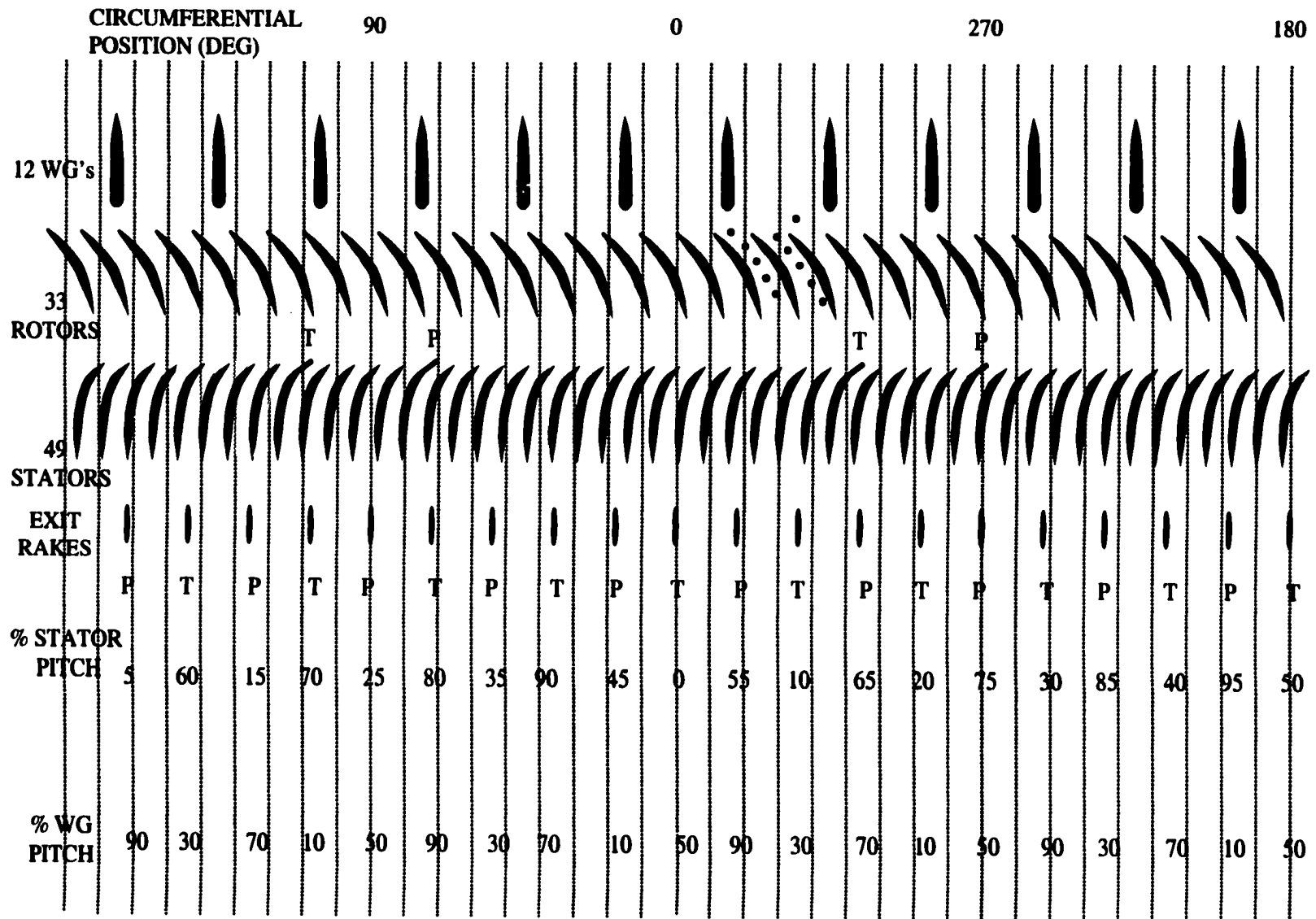


Figure 7. 12 Wake Generator Exit Rake Layout

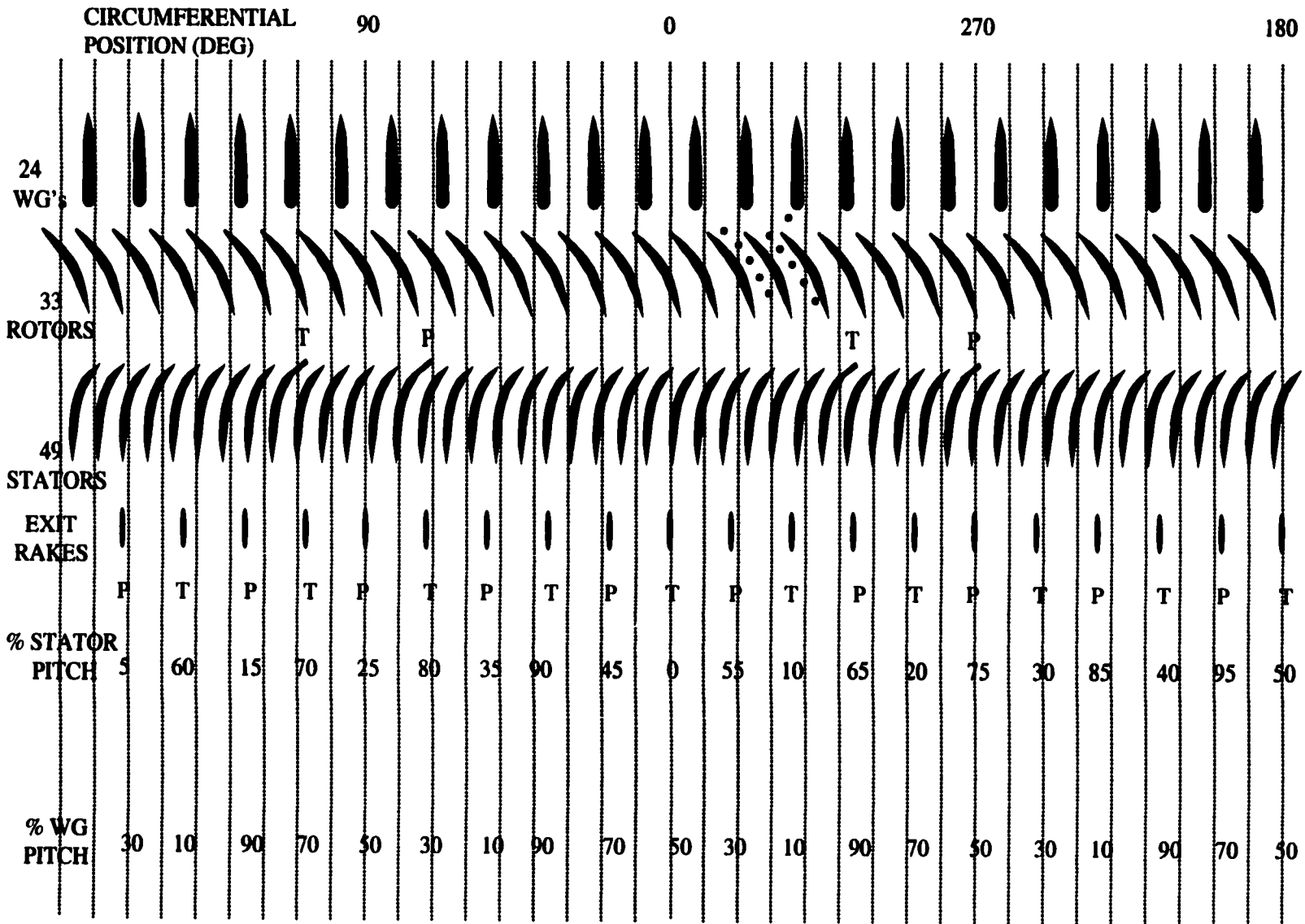


Figure 8. 24 Wake Generator Exit Rake Layout

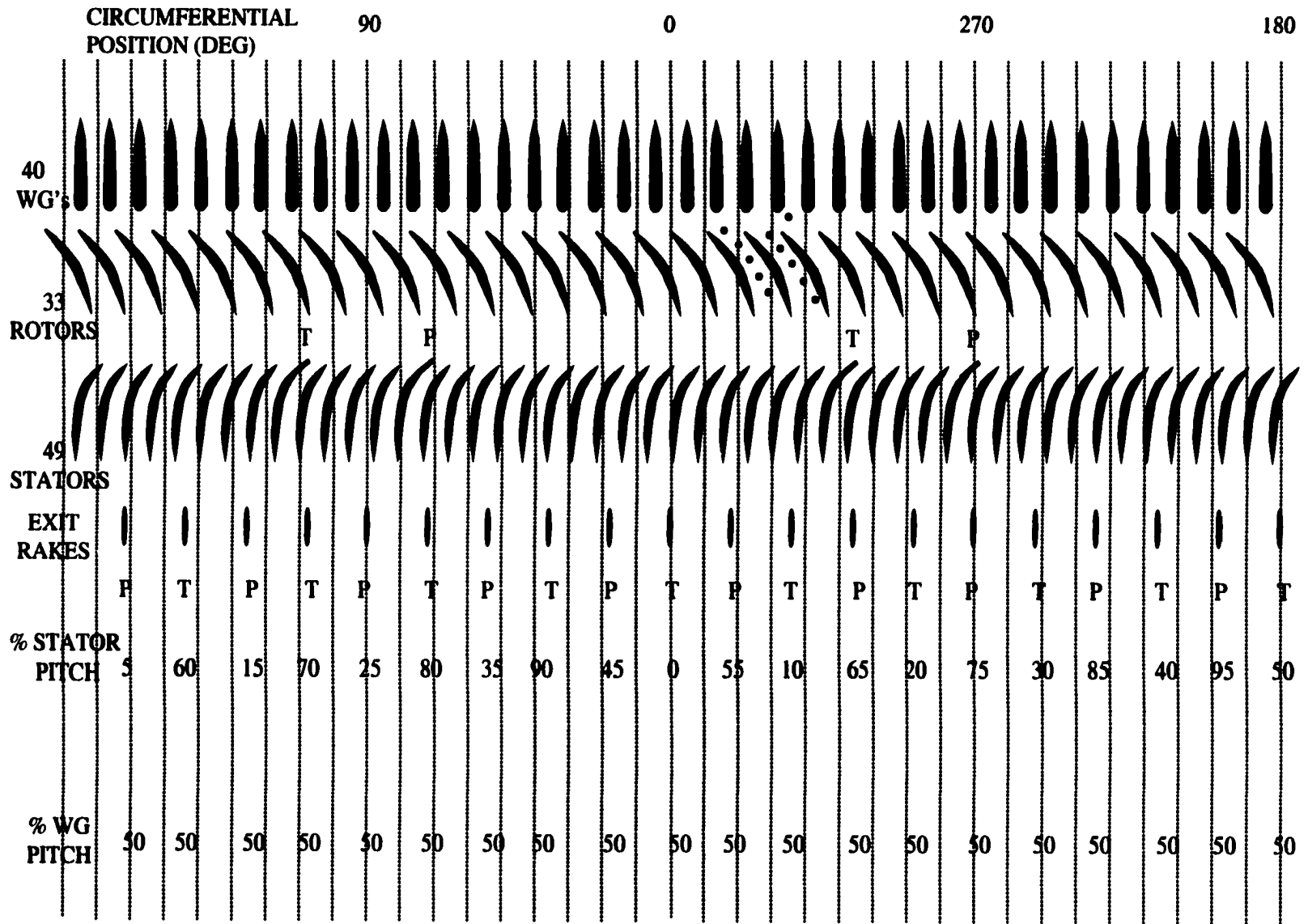


Figure 9. 40 Wake Generator Exit Rake Layout

over one stator pitch. This assumes that their influence persists through both the rotor and stator blade row. The results are now aliased to reflect a total of 98 wake generators (2 for each of the 49 stators) instead of the 12 or 24 that are actually in place. This phenomenon exists in any situation where fixed probes are used to quantify performance in embedded blade rows. For this experiment it will be shown that the exit probes do sense the influence of the wake generators upstream of the rotor. Therefore, the absolute value of the influence of wake generator spacing on performance will be influenced by aliasing, but the relative trends in measured performance between different configurations is still resolved. However, with 40 wake generators all of the exit probes will be equally influenced by the wake generator wakes. As shown in Figure 9 the exit rakes are all at 50% wake generator pitch. This situation makes it extremely difficult to isolate the influence of the wake generator wakes and therefore increases substantially the uncertainty of the 40 wake generator performance measurements.

### **Experimental Repeatability**

Since this research includes a parametric study on the influence of small changes in axial blade-row spacing and wake generator solidity on compressor performance, it was necessary to determine what magnitude of performance changes should be considered significant. This was accomplished by establishing the repeatability (or precision error) of the experiment.

The precision error of the measured mass flow rate, pressure ratio and efficiency was established through a series of repeat tests with the 24-wake-generator configuration. Compressor characteristic data was acquired on five different days for a common rig configuration of 24 wake generators, close spacing, and corrected speed of 100%. The results of these tests are shown in Figure 10. The repeatability results take into account the precision errors associated with the acquisition and reduction of total

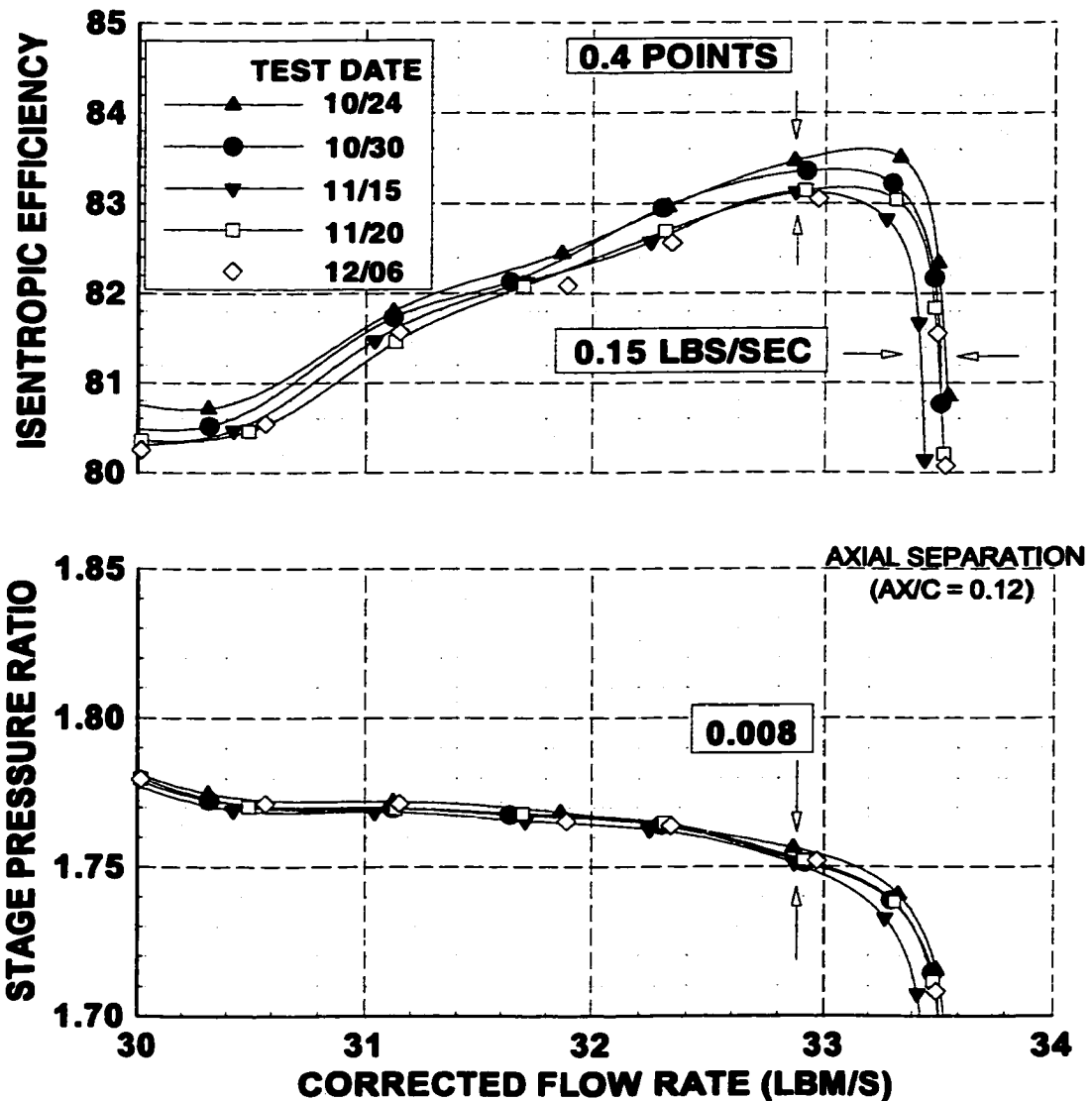


Figure 10. Repeatability Results

pressure and temperature measurements as well as precision errors related to the test article and test facility such as operating conditions, speed control, and inlet flow profiles. Based on a series of tests as much as a month apart, where some components of the rig were removed and then re-installed, the repeatability for pressure ratio, mass flow rate and efficiency was established. It was concluded that if a configuration change resulted in performance changes greater than 0.15 lbm/s in mass flow rate, 0.008

pressure ratio, or 0.4 points in efficiency that the changes were a result of the configuration change and not the uncertainty associated with the measurements.

### **Wake Generator/Rotor Only Configuration**

To alleviate some of the concerns that were raised due to the effects of aliasing on the measured performance and to remove any effects the stator may have on performance with changes in blade-row spacing, the SMI rig was modified to run without the stator as shown in Figure 11. This was accomplished by replacing the stator hardware with a Circumferential Traverse Assembly (CTA) at the case and an inner ring at the hub that matched the flowpath geometry of the original stator. The rotor-alone configuration allowed the isolation of the interaction between the wake generators and rotor as the primary experimental variable in producing performance changes.

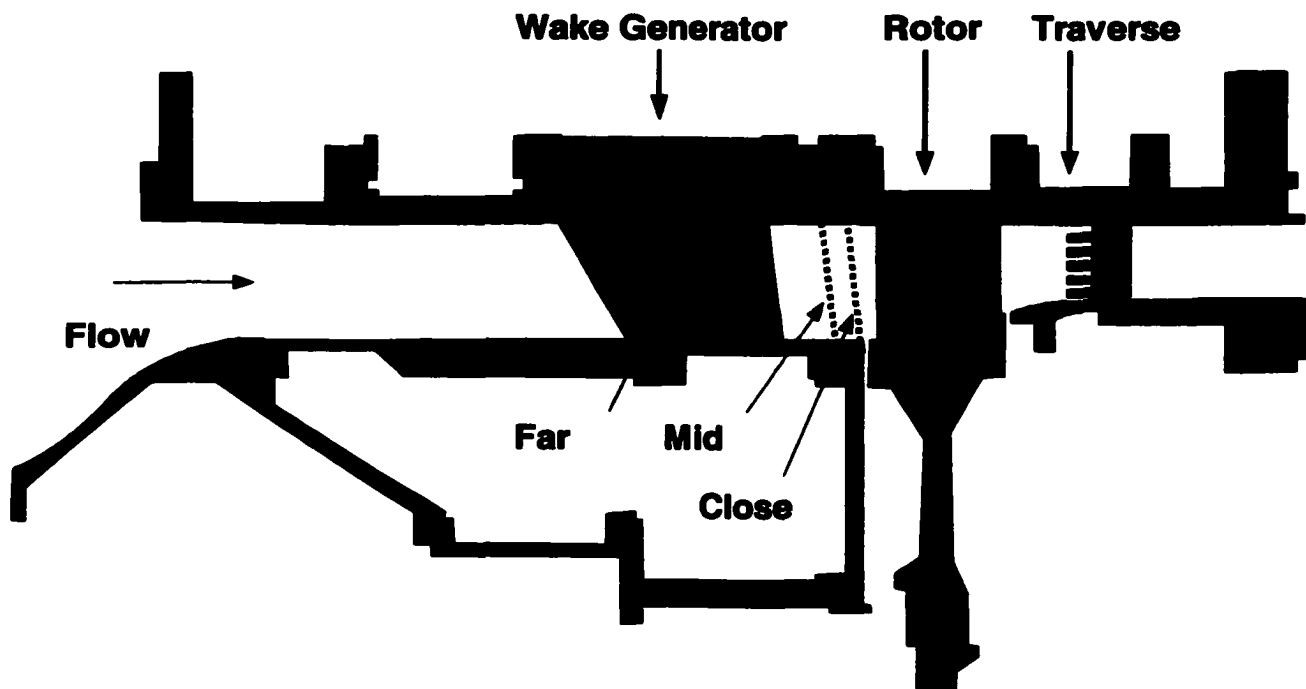


Figure 11. Wake Generator/Rotor Only Layout

A rake was designed and fabricated to measure the total pressure and temperature downstream of the rotor. The rake was positioned approximately 0.93 axial rotor chords downstream of the rotor trailing edge. The rake consisted of five kiel heads distributed spanwise (90.64, 70.77, 50.83, 31.22, and 12.37 percent span) and within each kiel head total pressure and total temperature were measured. Drawings of the rake are found in Appendix A. Guidelines were followed from reference [20] concerning the kiel head spacing and length to minimize the effect of the probe on the measured flow. The CTA was traversed a total range of 30.75 degrees circumferentially in increments of 0.375 degrees (2.5% wake generator pitch). This corresponded to two wake generator pitches for the 24 wake generator configuration. For the 40 wake generator configuration the CTA was traversed for 36 degrees in increments of 0.225 degrees (2.5% wake generator pitch) thus covering four wake generator pitches.

Prior to performance mapping the orientation of the CTA rake was optimized by obtaining data with the rake set at 5 degree increments between angles of 30 to 60 degrees to the axial direction. Mass flow rate, pressure ratio, and efficiency were measured at open throttle and the optimum angle was determined to be 40 degrees. The response time for the CTA rake to reach equilibrium was found to be 30 seconds. Therefore after rotating the CTA, the measurements were acquired after waiting 30 seconds.

Data acquired from the CTA rake were then area-averaged. The area-averaged total pressure and temperature were used with the measured inlet conditions described in the test article instrumentation section to determine the overall pressure ratio and isentropic efficiency for the rotor-alone configuration. The traverse rake results were area-averaged instead of mass-averaged because the flow angle entering the rake was unknown.

The rotor-alone configuration was only run for the 24 and 40 wake generator configurations since they showed the greatest changes of performance with spacing.

## **WAKE CALIBRATION**

Wake generator calibration served two purposes. One was to calculate the total pressure loss at various distances downstream of the wake generator blade-row. The loss was then used to correct the three-blade-row performance of the SMI rig at the rotor face to determine the effect of axial spacing on the flow capacity of an embedded compressor stage (two-blade-rows). Results of the flow capacity study were documented by Chriss, et al [21]. The second purpose of the wake generator calibration was to evaluate the width and depth of the wakes interacting with the downstream rotor. Knowledge of the wake properties aided in analyzing the experimental and numerical results. It was desirable to understand the similarities and differences of the wake generator wakes and those produced by a typical stator found in a transonic compressor. Since this research effort focuses on the 24 and 40 wake generator performance, only wake calibration results for those configurations will be presented.

### **Wake Calibration Instrumentation**

Wake generator calibration was accomplished by using the SMI rig as a flow generating device, moving the wake generator blade-row forward, and placing a Circumferential Traverse Assembly (CTA) between the wake generator blade-row and the rotor blade-row. Figure 12 shows the SMI wake calibration layout. Total pressure rakes were attached to the CTA at distances downstream of the wake generator corresponding to the three (close, mid, and far) axial spacings between the wake generator and rotor blade-rows. The original CTA rakes shown in Figure 13 measured total pressure at 6.44%, 18.86%, 30.82%, 42.40%, 64.38%, 74.91%, 85.14%, and 95.11% wake generator span. Unsteady total pressure was measured at 53.56% span but was not used in the wake calibration analysis.

After the initial measurements from the CTA rakes were analyzed, it was determined that a more thorough measurement of the endwall

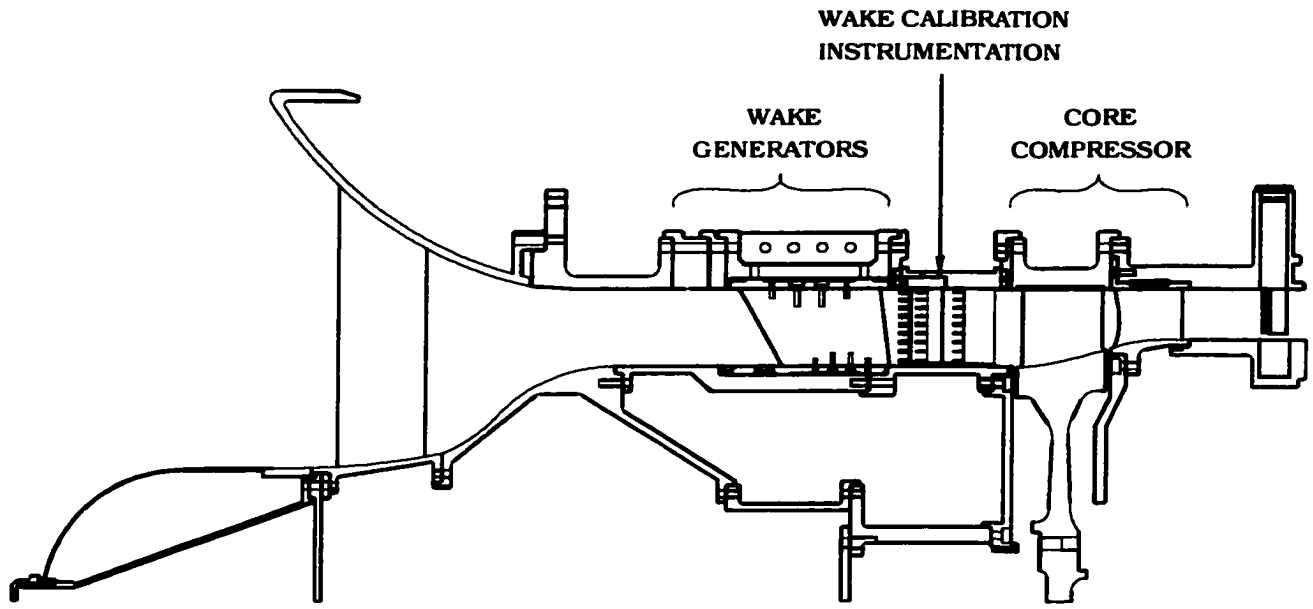


Figure 12. SMI Wake Calibration Layout



Figure 13. CTA Rake

boundary layers was necessary for accurate loss measurement. A set of three CTA boundary layer rakes were designed and fabricated to measure the total pressure near the hub and case. A figure of one of the boundary layer rakes is shown in Figure 14. These rakes made hub measurements at 0.93%, 2.74%, 4.63%, 6.44%, 8.25%, and 10.06% wake generator span and case measurements at 92.29%, 93.73%, 95.12%, 96.51%, 97.94%, and 99.28% wake generator span. Hypodermic tubing was used which allowed the high concentration of measurements near the endwalls. To minimize the effect of flow displacement on the pressure measurement, guidelines recommended in reference [20] were followed to determine the length and diameter of the sensing elements. Both rakes made measurements at common locations of 6.44% and 95.11% span to check that no bias existed between the two rakes.

Static pressure measurements were also made at the hub and case in the same three axial planes as the total pressure probes. Case static pressure taps were located in five-degree increments on both sides of each CTA rake and rotated circumferentially with the CTA. At the hub, static pressures were measured with two groups of twenty-one stationary taps that covered two or three wake generator pitches depending on the configuration being 24 wake generators or 40 wake generators.

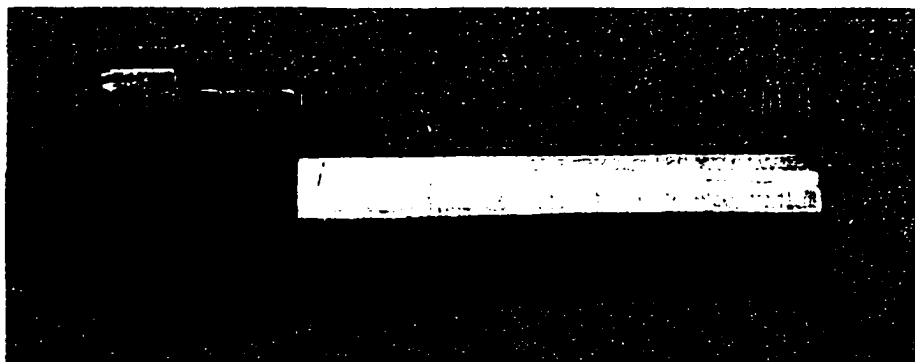


Figure 14. CTA Boundary Layer Rake

### **Wake Calibration Procedure**

The CTA was rotated in increments of 10% wake generator pitch when in the freestream and 2.5% wake generator pitch when in the wake. Figures 15 and 16 illustrate the circumferential range traversed by the CTA and how many wake generator pitches were traversed. For the 24 wake generator calibration two complete wake generator pitches were traversed and for 40 wake generators three complete wake generator pitches were traversed.

From the measured total and static pressure measurements the spanwise axial velocity profile was determined using basic compressible flow equations. The static pressure profile was estimated based on a linear interpolation between the average hub and case static pressures measurements. Static temperature at each span was calculated from the interpolated static pressures, the measured total pressure, and the total temperature measured at the inlet from the equation

$$t = T / \left( \frac{P}{p} \right)^{\frac{\gamma-1}{\gamma}}$$

This assumes the total temperature was constant from the inlet to the CTA rakes and did not vary with span. The ratio of specific heats and gas constant for air were determined from inlet measurements as part of the data acquisition process. Mach number at each CTA probe location was calculated from the total and static pressure as

$$M = \sqrt{\left[ \left( \frac{P}{p} \right)^{\frac{\lambda-1}{\gamma}} - 1 \right] \frac{2}{\gamma-1}}$$

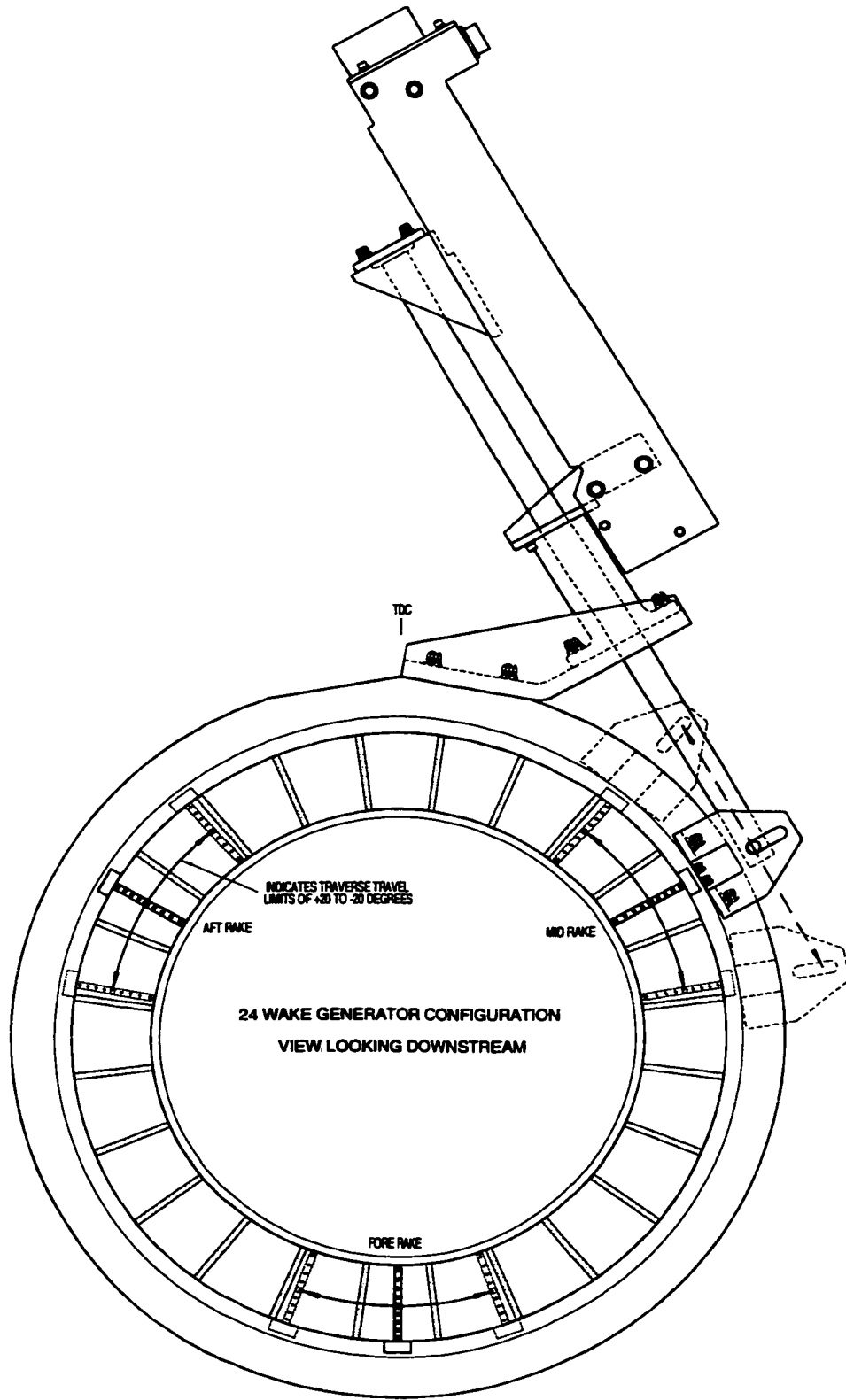


Figure 15. 24 Wake Generator Calibration

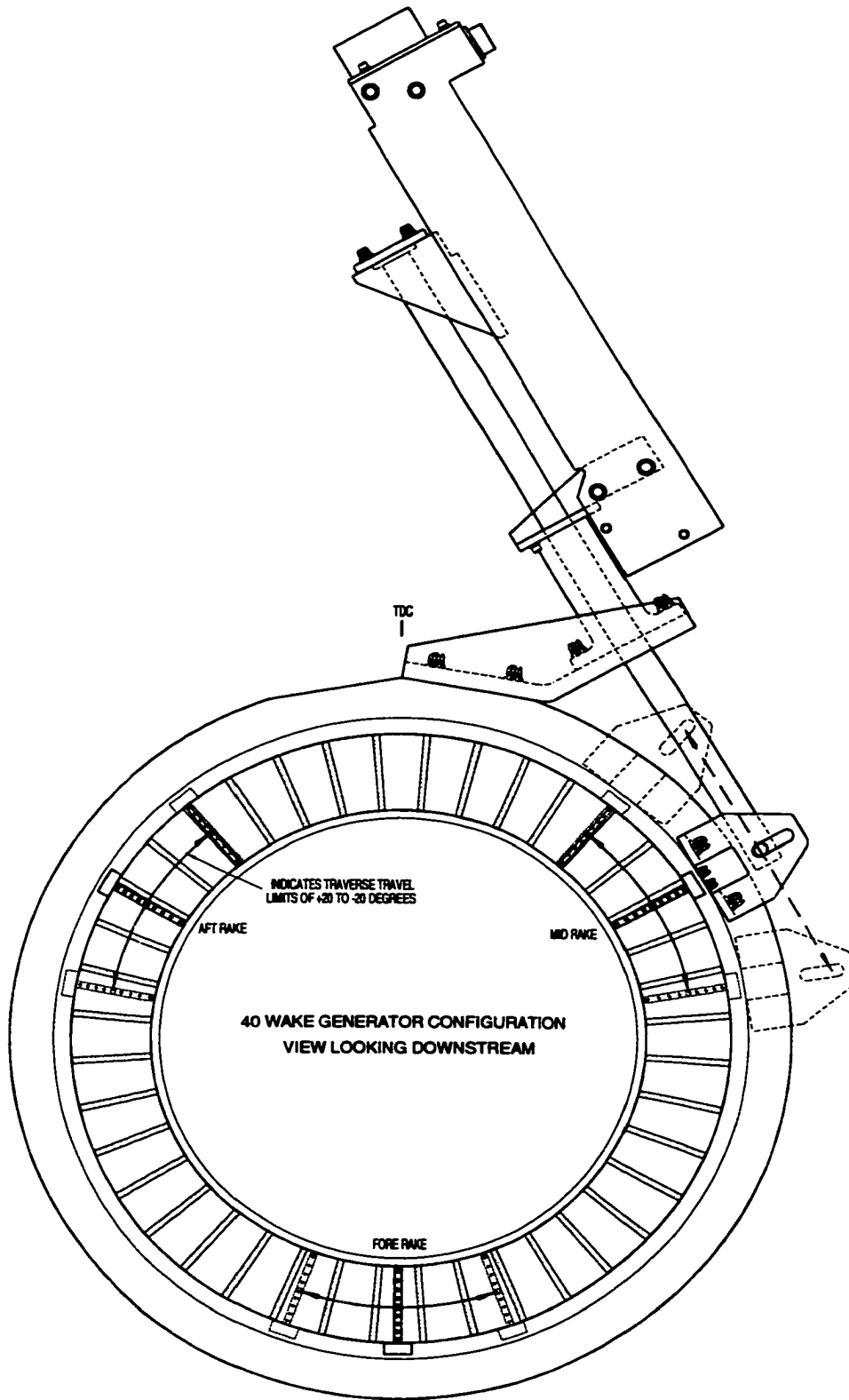


Figure 16. 40 Wake Generator Calibration

and velocity was then determined from the Mach number and static temperature.

$$V = M \sqrt{\gamma R t_g}$$

Freestream velocity ( $V_\infty$ ) was computed from an average of the velocities calculated at mid pitch between 6.44% span and 85.14% span, the region outside the boundary layer.

The loss coefficient,  $\omega$ , is defined as

$$\omega = \frac{P_{rake} - P_{inlet}}{P_{inlet} - P_{inlet}}$$

where  $P_{rake}$  is the total pressure measured by the rake,  $P_{inlet}$  is the total pressure measured at the plenum (see Figure 5), and  $p_{inlet}$  is a static pressure measurement located on the hub flowpath just upstream of the wake generator. The calibration assumes that the downstream rotor did not affect the CTA rake measurements and consequently the calculated loss coefficient. The loss coefficient therefore does not account for any losses other than that due to mixing.

### **Wake Calibration Results**

Since the mixing loss is dependent on Mach number, wake calibrations were made over a range of mass flows. The results presented here were acquired at 100%  $N_c$ , open throttle. Since the wake properties of both the 24 and 40 wake generator configurations showed similar trends as spacing changed, calibration plots are only be presented for the 24 wake generator results. The total pressure measurements acquired by the CTA rakes are presented in the form of contour plots in Figures 17 - 19. These plots do not include the boundary layer measurements. The difference

between each contour line is  $0.3 \text{ lbf/in}^2$  and the orientation is downstream looking up. The dashed lines in the figures indicate the location of the wake generators. From these plots the widening of the wake from close to far spacing is clearly evident. Wake depth is deepest at close spacing and becomes shallower at mid and far spacing. The wake width is nearly constant from hub to case. This confirms the intent of the wake generator design to produce a two-dimensional wake profile. The wake is constant in the circumferential and radial directions but not in the streamwise direction. Also evident is the boundary layer growth at the casing. The boundary layer is slightly visible at close spacing and most obvious at far spacing. The hub boundary layer was not measured by the CTA rakes signifying the boundary layer is located below the hub most probe at 6.44% span.

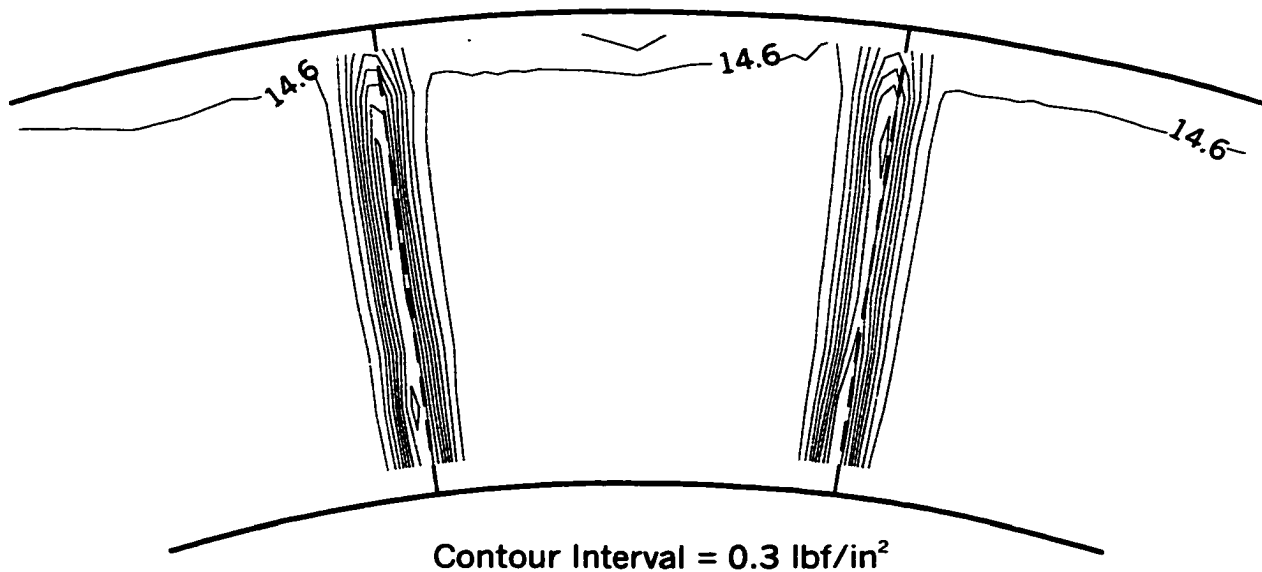


**Figure 17. 24 Wake Generator Total Pressure Contours, Close Spacing**

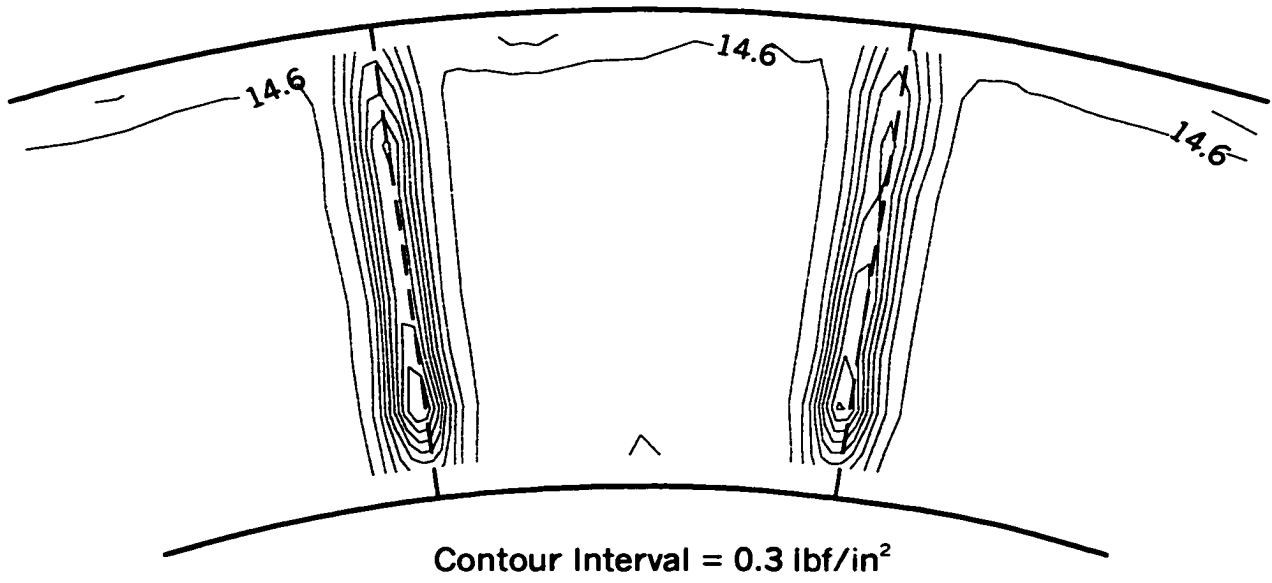


Figure 18. 24 Wake Generator Total Pressure Contours, Mid Spacing

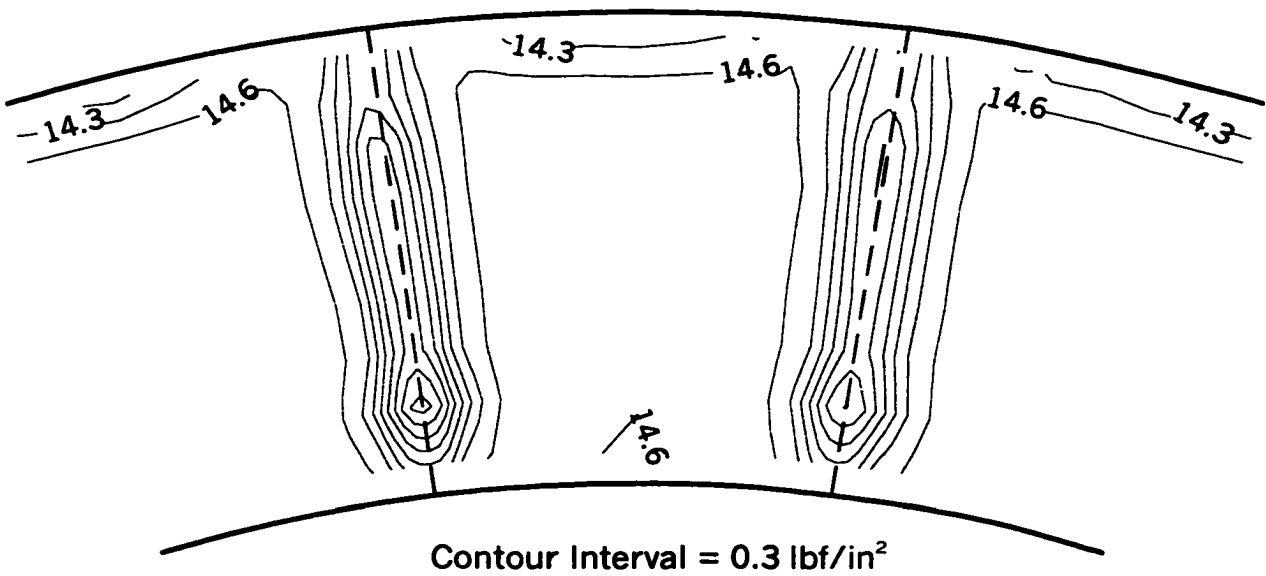


Figure 19. 24 Wake Generator Total Pressure Contours, Far Spacing

Velocity profiles for the 24 wake generator configuration at the hub, case, and near mid span are shown in Figures 20 - 22. Here it is observed that the wake depth is similar at the hub and case and deepest near mid span. The effect of the casing boundary layer is once again evident at 95.12% span. Close inspection of the total pressure contours and velocity profiles indicate some wake-to-wake variability for different wake generators at the same spacing. This will be addressed later in this section. Wake decay was analyzed by Chriss et al. [21] and the results are shown in Figure 23. The SMI wake generator wakes show similar trends to that compared in the literature [22-24].

The overall mass-averaged loss coefficients are presented in Table 3 and Table 4. The flow Mach number during the calibration,  $M_{in}$ , was calculated based on measurements made upstream of the wake generator blade-row. Including the endwall boundary layer effects increased the loss coefficient magnitude 20% to 40% for the 24 wake generator configuration

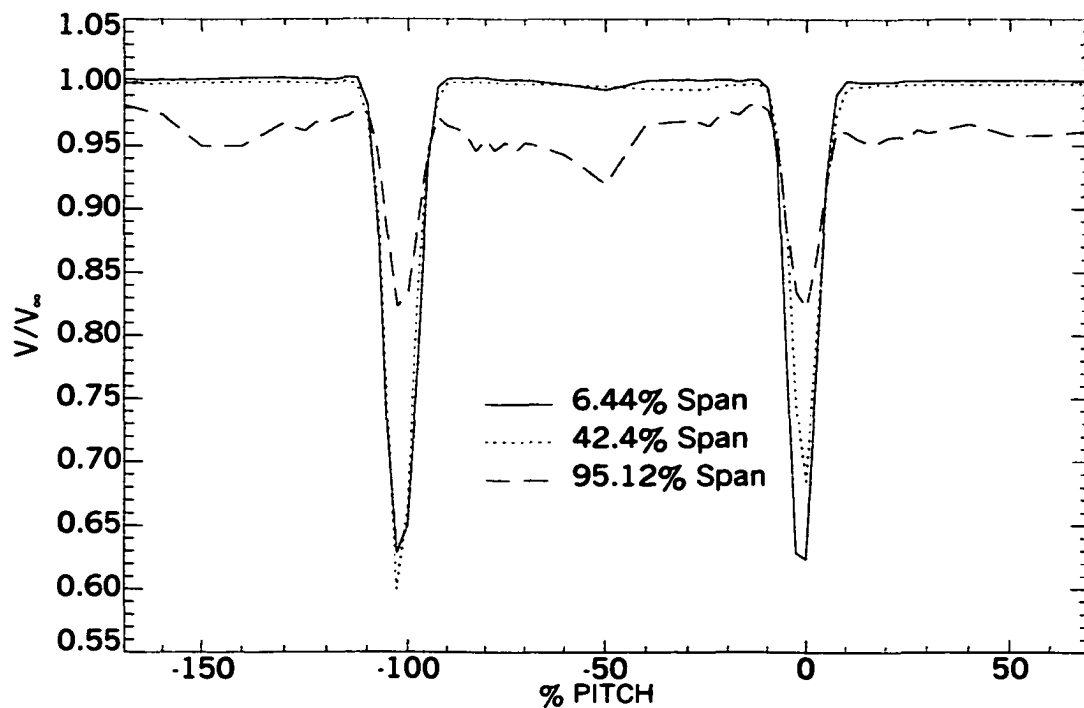


Figure 20. 24 Wake Generator Velocity Profiles, Close Spacing

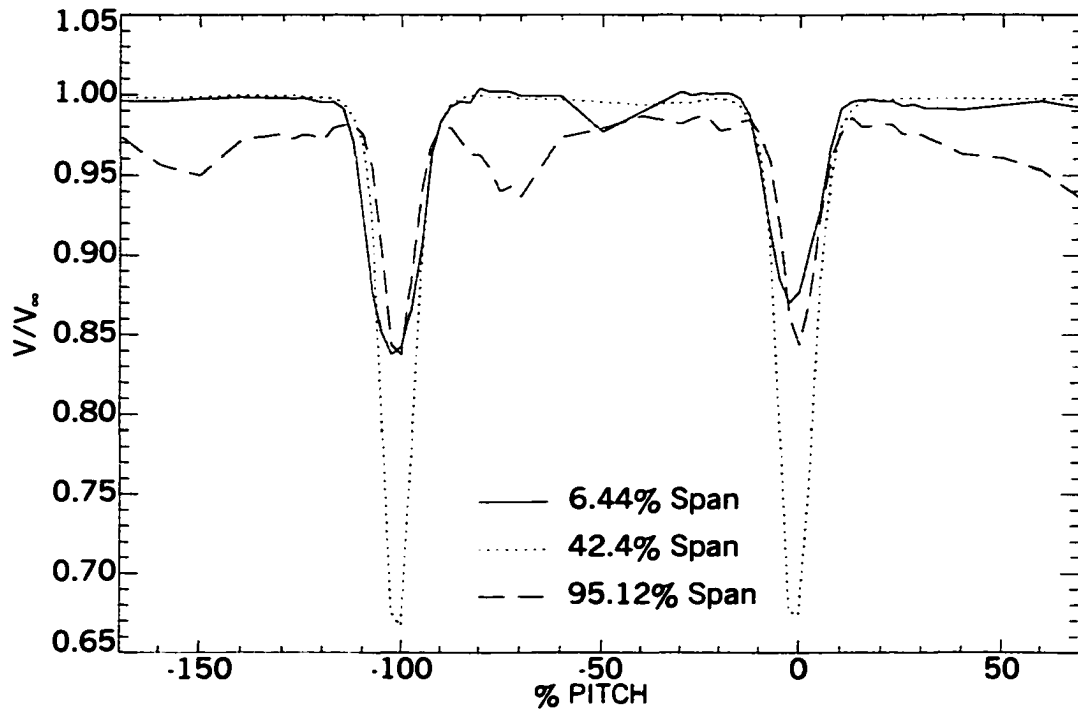


Figure 21. 24 Wake Generator Velocity Profiles, Mid Spacing

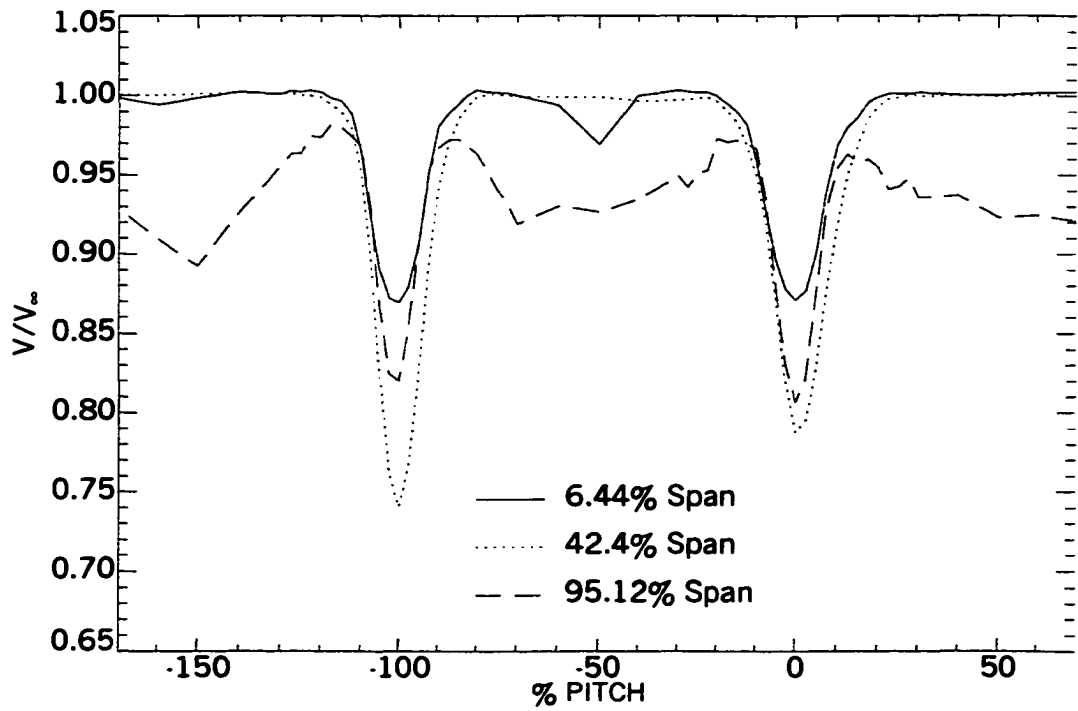


Figure 22. 24 Wake Generator Velocity Profiles, Far Spacing

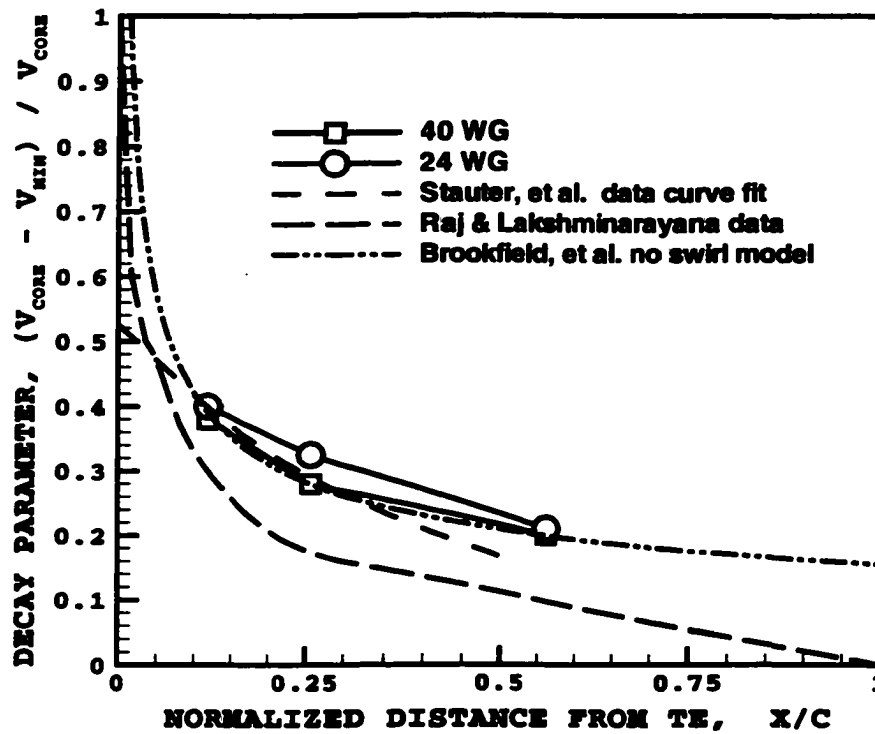


Figure 23. Wake Decay Comparison

Table 3. 24 Wake Generator Loss Coefficients

Spacing	$\omega$ without boundary layer	$\omega$ including boundary layer	% Increase
Close	0.0607	0.0822	35.42
Mid	0.0658	0.0917	39.36
Far	0.0844	0.1012	19.91

$$M_{in} = 0.574$$

Table 4. 40 Wake Generator Loss Coefficients

Spacing	$\omega$ without boundary layer	$\omega$ including boundary layer	% Increase
Close	0.1099	0.1426	29.75
Mid	0.1283	0.1541	20.11
Far	0.1627	0.1845	13.40

$$M_{in} = 0.568$$

and between 13% and 30% for the 40 wake generator configuration. Plots of the mass-average loss coefficient versus wake generator span are found in Figures 24 and 25. These results include the CTA boundary layer rake measurements. As expected the highest loss is found at the endwalls and this accounts for the increase in overall loss coefficients found in Table 3 and Table 4 when the CTA rake boundary layer measurements are included. The 24 wake generator loss profiles are nearly constant in the freestream with only a slight increase in loss around 20% span for the far spacing configuration. The loss also increases at the endwall boundary layers located above 92% span and below 8% span. For the 40 wake generator case, the difference in freestream loss for the different spacings is more noticeable and the far spacing loss profile is less two-dimensional. At the endwalls the boundary layer losses are evident above 94% span and below 6% span.

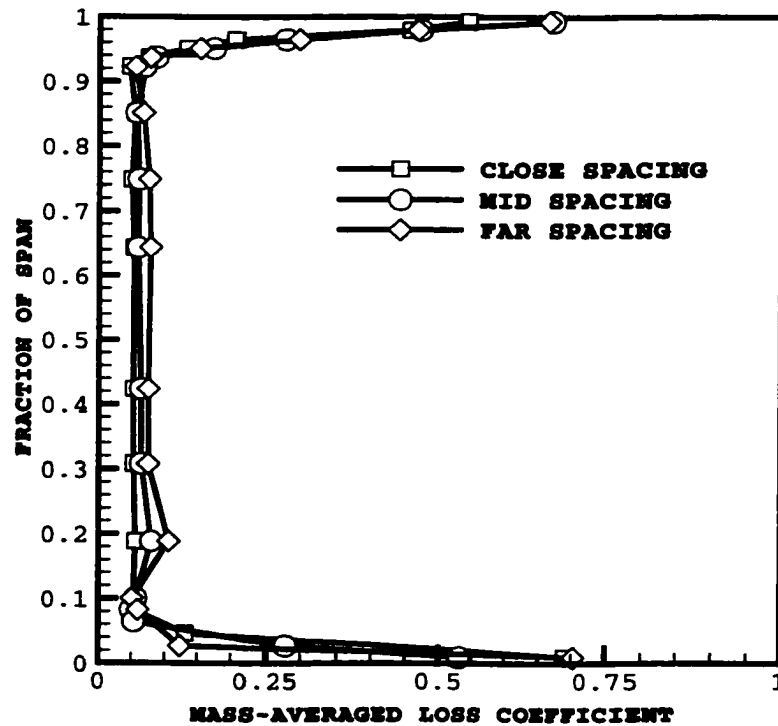


Figure 24. 24 Wake Generator Loss Coefficient Profile

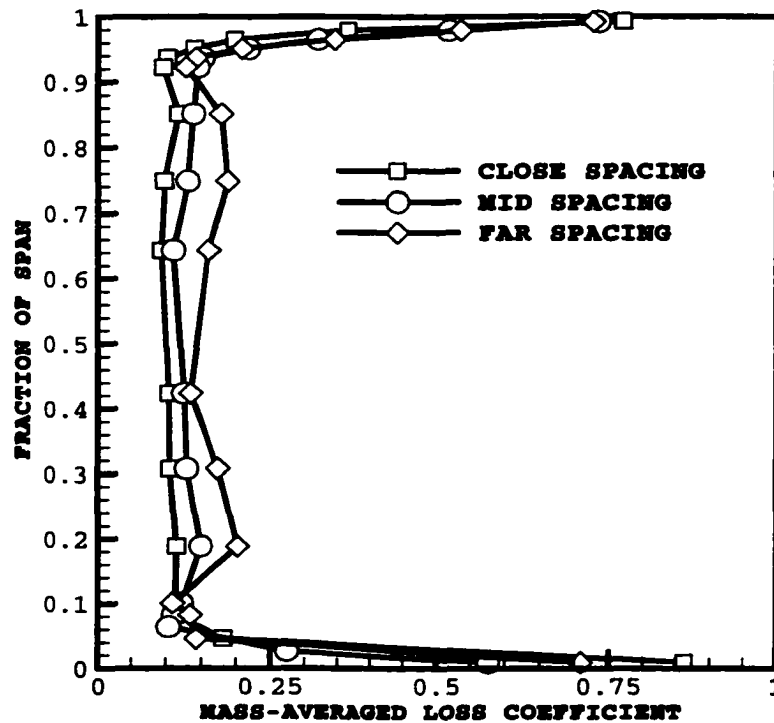


Figure 25. 40 Wake Generator Loss Coefficient Profile

The design intent of the wake generators was an overall loss coefficient of 0.070 for 24 wake generators and 0.155 for 40. These values are close to the experimentally measured loss coefficient without the boundary layer. The wake generators were designed with a quasi three-dimensional streamline curvature code and a two-dimensional potential flow solver with boundary layer analysis. It was assumed that the endwall losses would be low and this is true at far spacing but at close and mid spacing the endwall losses do contribute significantly to the loss coefficient. As a result, the overall loss coefficient produced by the wake generators was a little higher than the design intent. However they are still well within the range typically found in highly loaded stators.

During the course of the wake calibration study for this and other research programs using the SMI rig, different wake generators at the same configuration were calibrated. A significant wake-to-wake variability in the

overall loss coefficient was observed. As shown in Figures 17 through 19 presented previously, variations in wake width and depth are clearly visible for different wake generators. A further example is shown in Figure 26, where loss coefficient (not including boundary layer) for three adjacent wake generators is compared for the 40 wake generator configuration, far spacing. In this case there was a difference of 32% between the minimum and maximum loss coefficient. Loss coefficient uncertainty for a single wake generator was determined to be  $\pm 0.001$ . However, due to wake-to-wake variability, the overall mass averaged loss coefficient uncertainty was established as  $\pm 0.01$ .

In summary, the wake generators produced a wake of nearly constant loss from hub to tip in-between the endwall boundary layers. This was the design intent. The overall loss coefficient is representative of the loss produced from a modern technology transonic compressor front stage. Due to the blunt trailing edge of the wake generator, the wakes may be wider

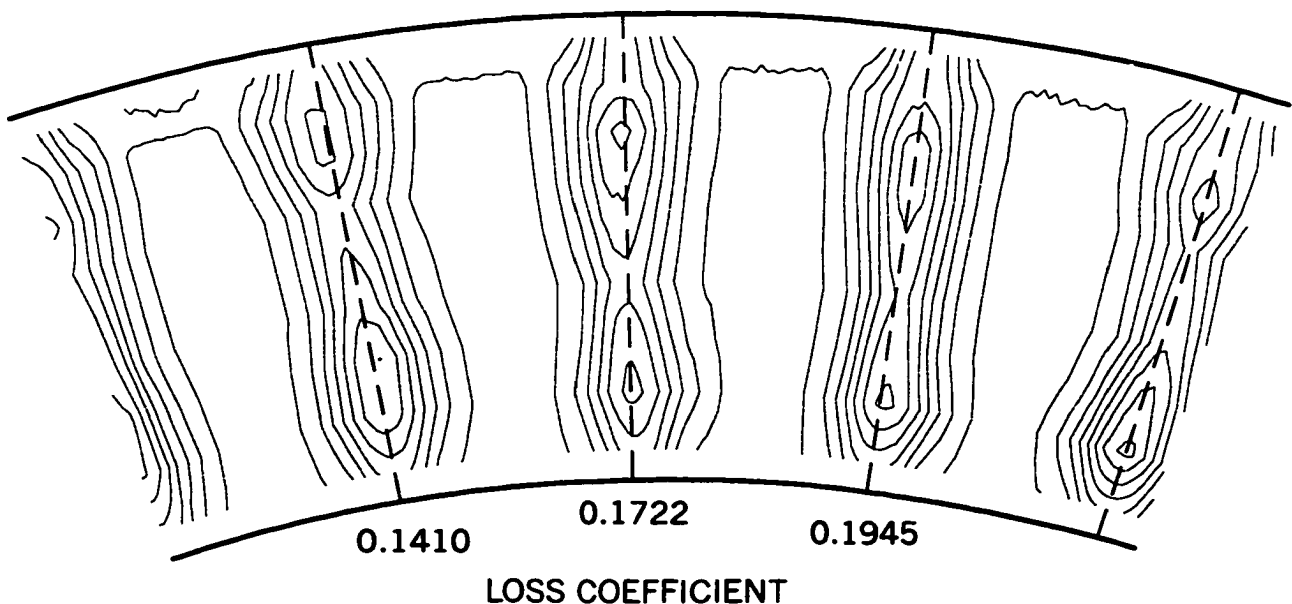


**Figure 26. 40 Wake Generator Total Pressure Contours, Far Spacing, with Overall Loss Coefficient**

than what would be produced from a normally cambered stator airfoil, but wake measurements for comparison are not found in the open literature. There is some concern that a wake and loss produced from a loaded stator blade would affect the interaction between a stator and rotor differently. A new design of the wake generator is underway to better simulate a loaded stator and to address this concern.

## **SMI AND WAKE GENERATOR/ROTOR ONLY PERFORMANCE**

Experimental results obtained while testing the SMI rig in the CARL facility are presented in this section. Data are presented for the SMI rig (wake generator/rotor/stator) and wake generator/rotor only layouts. The purpose of this section is to document what affect changes in axial spacing between the wake generator and rotor had on the overall compressor performance. The section concludes with a discussion on the significance of the observed changes on overall engine performance.

### **SMI Results**

Performance characteristics for the SMI rig are shown for each configuration in Figures 26 through 28. Figure 26 shows that for the 12-wake generator configuration the close and mid spacing performance was nearly identical, the only exception being the near-stall pressure ratio characteristic. At mass flow rates below 32 lbm/s the pressure ratio at mid spacing was slightly higher than close spacing. The far spacing pressure ratio characteristic was consistently higher than that of close and mid spacing. The far spacing efficiency characteristic was higher than the close and mid spacing characteristic near peak efficiency. As the mass flow rate approached stall (32.5 lbm/s) the efficiency at far spacing was similar to that of close and mid spacing. The choking mass flow rate, which is the value of the vertical part of the characteristic, was higher for far spacing than close and mid. The difference in pressure ratio, efficiency, and mass flow rate between the far and close/mid configurations was greater than the repeatability values presented in the previous section. Therefore it was concluded that the observed change in performance with axial blade-row spacing was real and not due to experimental measurement uncertainty. In addition to the 12 wake generator performance, Figure 26 contains the SMI rig performance with no wake generators (clean inlet) installed. The clean-inlet configuration had a higher choking mass flow rate and higher peak

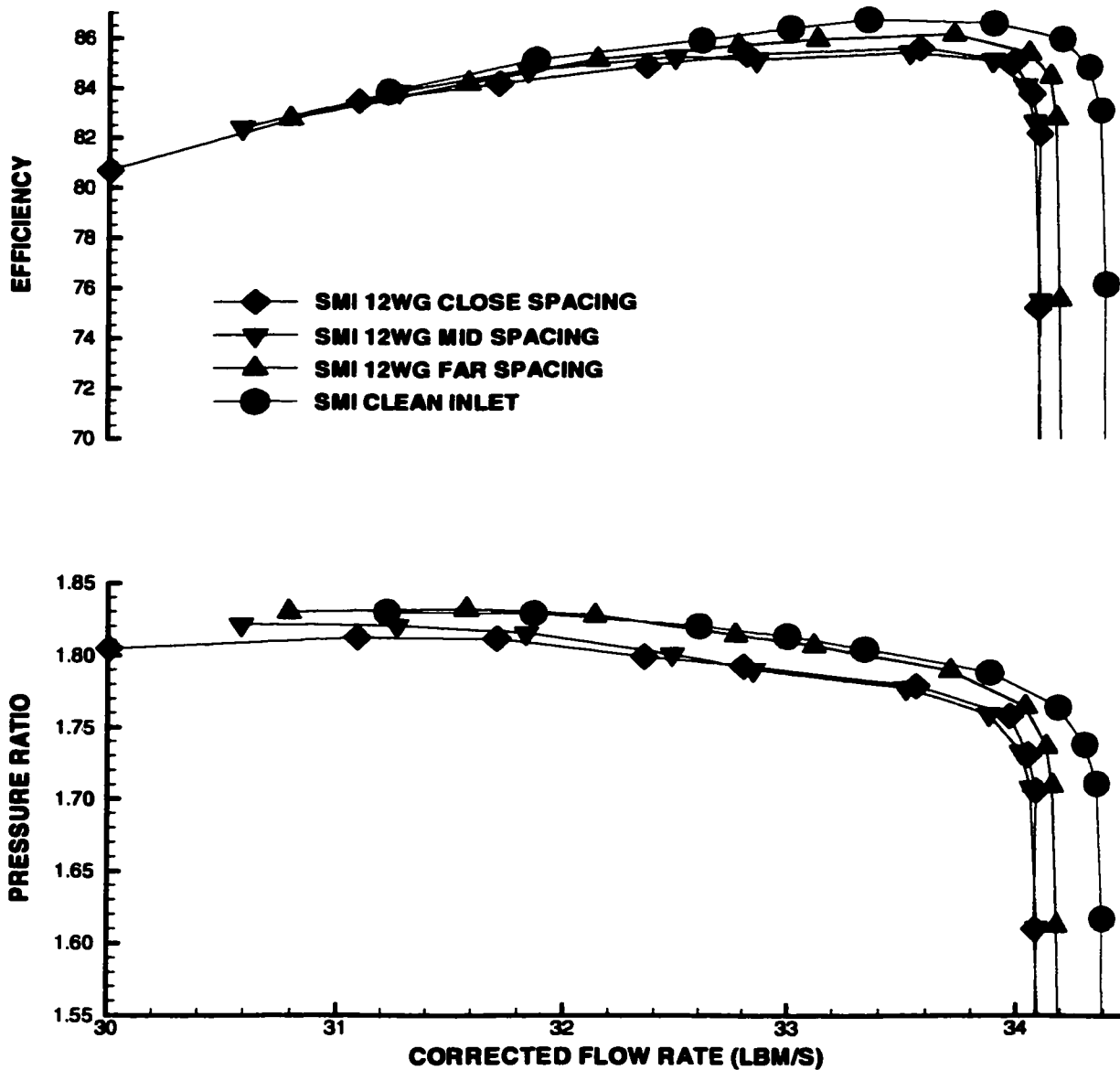


Figure 26. SMI 12 Wake Generator Performance, 100%  $N_c$

efficiency than far spacing. Due to the blockage and losses associated with the wake generators installed, the mass flow rate was less than for clean inlet. The pressure ratio characteristic of the clean inlet and far spacing configuration were very similar as mass flow rate was reduced from the peak efficiency value. The data points acquired nearest to stall are not necessarily indicative of the stall margin of the compressor. There was

some variability between the mass flow rate where the data point was obtained and the mass flow rate at which the SMI rig stalled. Consequently, no analysis on the relationship between stall margin and blade-row spacing was attempted in this research effort.

For the 24-wake generator results shown in Figure 27 there was a significant difference in performance between each of the three spacings tested. Both the pressure ratio and efficiency characteristics decreased significantly as the axial blade-row spacing was reduced from far to close. For the 24-wake generator configurations the performance difference between the three axial blade-row spacings persisted over the entire flow range of the characteristic. The choking mass flow rate decreased as the blade-row spacing was reduced.

Figure 28 shows the performance characteristics for the 40 wake generator configuration. However, these results have come under scrutiny because of the aliasing problem presented in the Stage Matching Investigation Rig section of this report. The aliasing occurs because the wake generator wakes persist far downstream and are sensed by the exit rakes used to measure total temperature and total pressure. The up and down fluctuations in the efficiency characteristics as mass flow rate was reduced from choke to near-stall is a consequence of this aliasing problem. However, the observed drop in choking mass flow rate is real and unaffected by the exit rake measurements.

#### **Part Speed SMI Performance**

Part-speed results for the 24-wake generator configuration are presented in Figures 29 and 30 along with clean inlet performance. At 85%  $N_c$  the mid and far spacing performance were very similar. At corrected mass flow rates between 27 lbm/s and 30 lbm/s the close spacing performance was less than that of mid and far. It should be noted that at lower corrected speeds the measurement uncertainty increases and therefore at 85%  $N_c$  the differences between close and mid/far performance

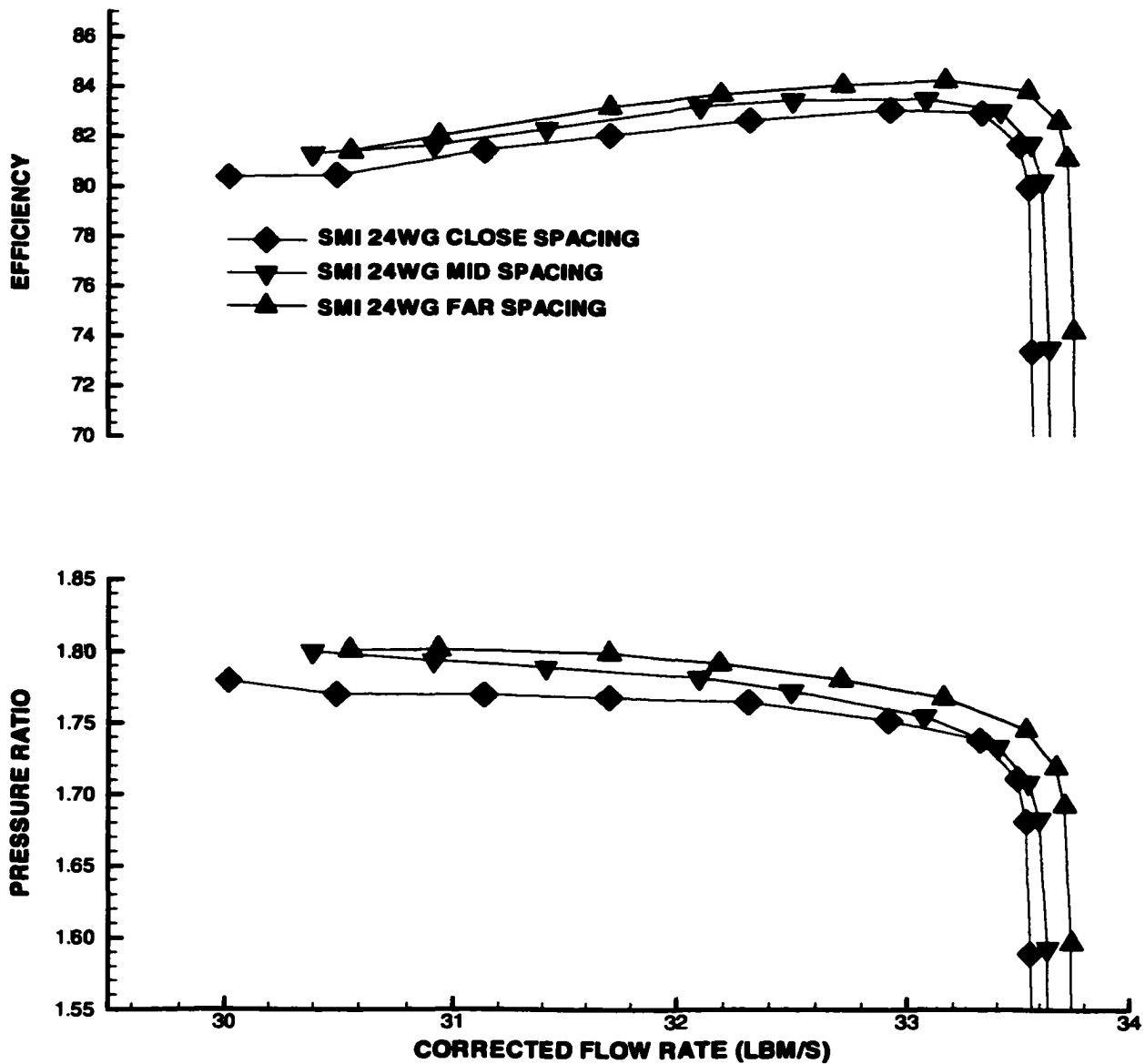


Figure 27. SMI 24 Wake Generator Performance, 100%  $N_c$

is most likely insignificant. At 85%  $N_c$  and below the relative velocity of the rotor is subsonic throughout the span. Without a shock system present the flow does not choke when the throttle is completely open. The maximum mass flow rate at open throttle for all three spacings was nearly the same. The clean inlet pressure ratio and efficiency characteristics were greater

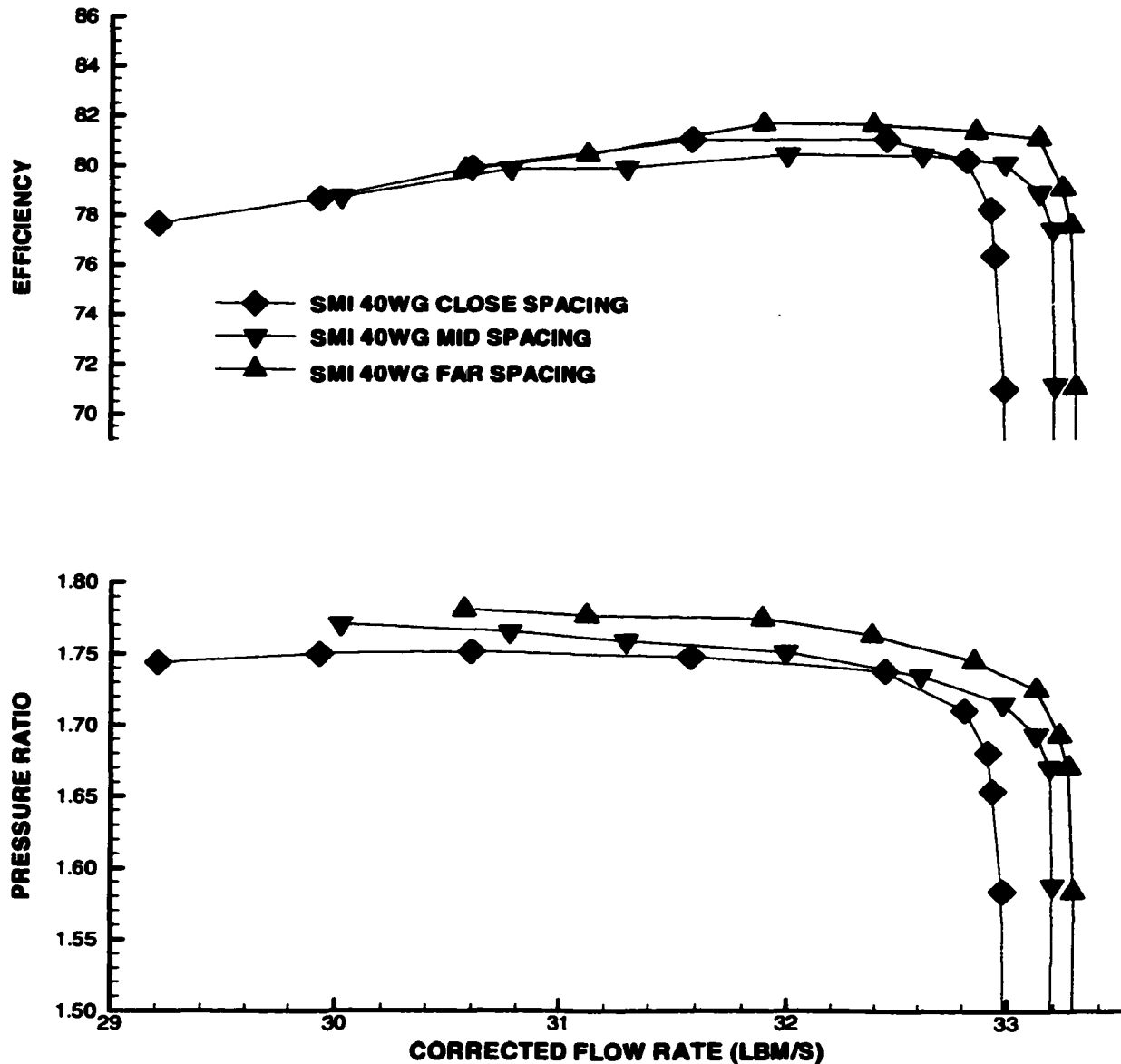


Figure 28. SMI 40 Wake Generator Performance, 100%  $N_c$

than the characteristics with wake generators present. The maximum mass flow rate of the clean inlet configuration was also higher.

Performance characteristics at 70%  $N_c$  are shown in Figure 30. At this speed it was clear that there were no significant differences in performance between the three spacings. As seen in the 85%  $N_c$  data, the maximum corrected mass flow rate attained was similar for all three

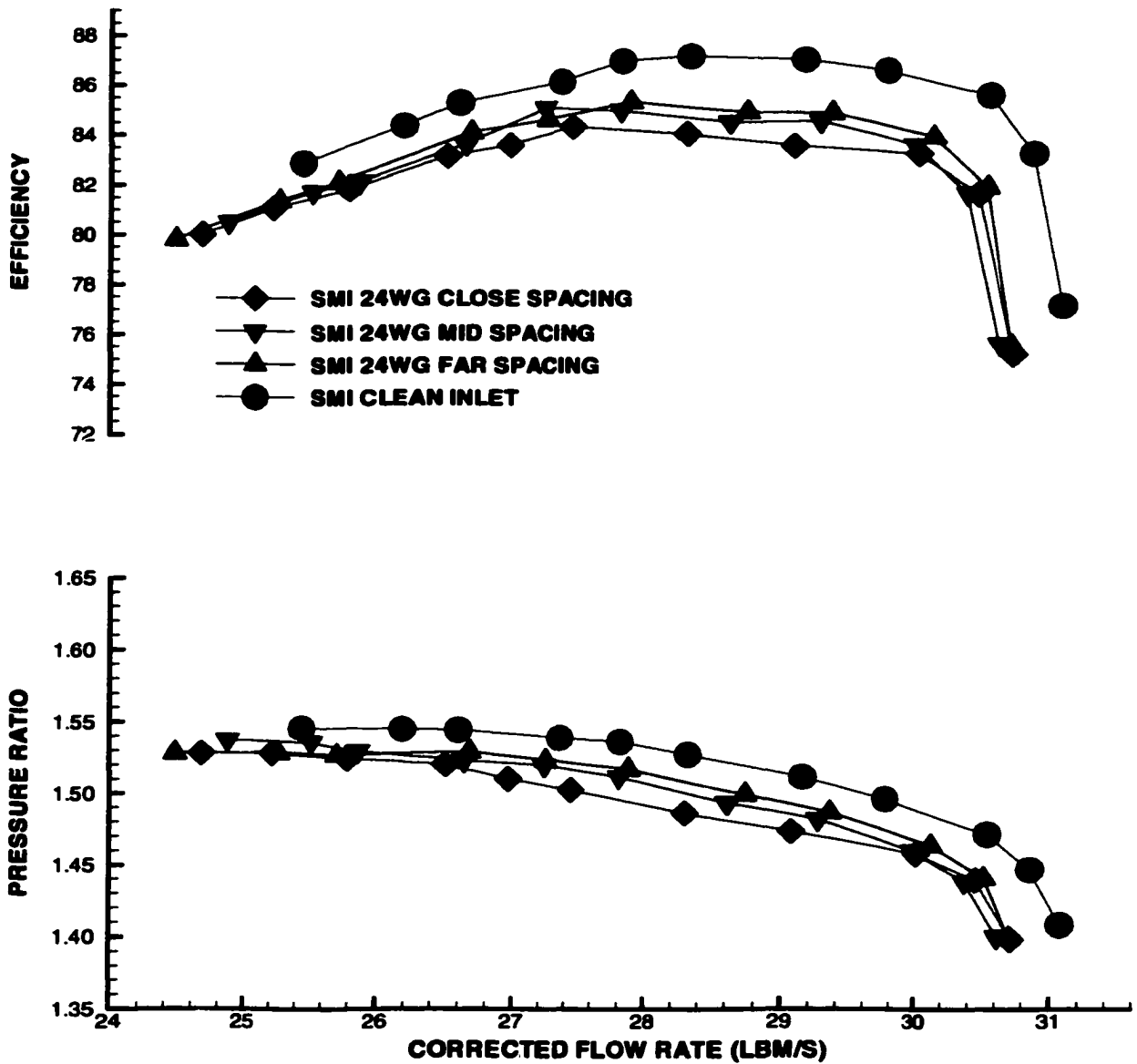


Figure 29. SMI 24 Wake Generator Performance, 85%  $N_c$

spacings. The clean inlet pressure ratio characteristic was only slightly higher than the 24 wake generator configurations, however, the clean inlet efficiency characteristic was still significantly greater. The clean inlet maximum mass flow rate was higher than with wake generators but the difference was less than that observed at 85%  $N_c$ .

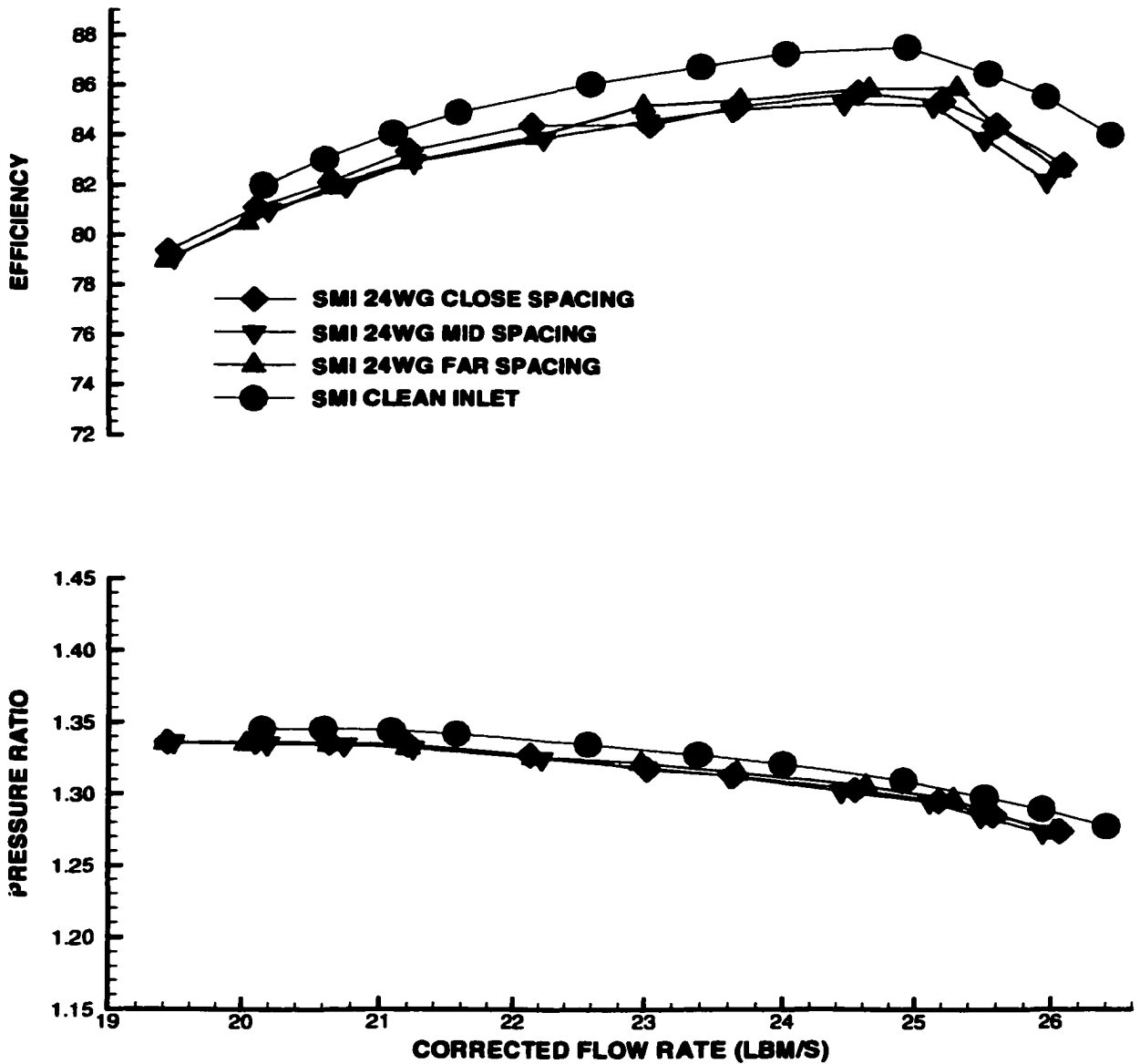


Figure 30. 24 Wake Generator Performance, 70%  $N_c$

### Wake Generator/Rotor Only Results

The SMI rig was converted to run without the downstream stator in order to remove any doubts concerning the exit rake aliasing problem and the measured SMI performance. Furthermore, removing the stator isolated the change in axial spacing between the wake generator blade-row and the rotor blade-row as the only variable to account for any measured changes in

the wake generator/rotor only compressor performance. The traverse rake and data acquisition procedures for measuring the total pressure and total temperature downstream of the rotor were described in the Stage Matching Investigation Rig Section.

Figure 31 shows the wake generator/rotor only performance for the 40 wake generator configuration. A consequence of removing the SMI stator was a severe increase in backpressure in the facility flowpath downstream of the test article that limited the maximum mass flow rate attainable. For this reason the data shown in the wake generator/rotor only configuration was only attained for flows ranging from below peak efficiency to near-stall. Although the entire compressor map was not obtainable, the limited observations made are felt to be representative for the complete flow range. Without the losses associated with the downstream stator the pressure ratio and efficiency characteristics of the wake generator/rotor only configuration were higher than the corresponding original SMI rig.

Figure 31 shows that the pressure ratio and efficiency characteristics increased as the spacing was changed from close to far. The measured difference was greater than the experimental repeatability thus confirming its significance. The difference in efficiency between far and mid spacing was the same as the difference between mid and close spacing. The difference in pressure ratio between the close and mid spacing characteristics was greater than between mid and far spacing. Despite the limited control of mass flow rate during the wake generator/rotor only experiments, an attempt was made to acquire data at consistent mass flow rates for each of the three spacings. The 40 wake generator/rotor only results are important because the aliasing problem present during the original SMI rig measurements (see Figure 28) prevented accurate documentation of the performance changes at that configuration. The 40 wake generator configuration performance trends from Figure 31 were

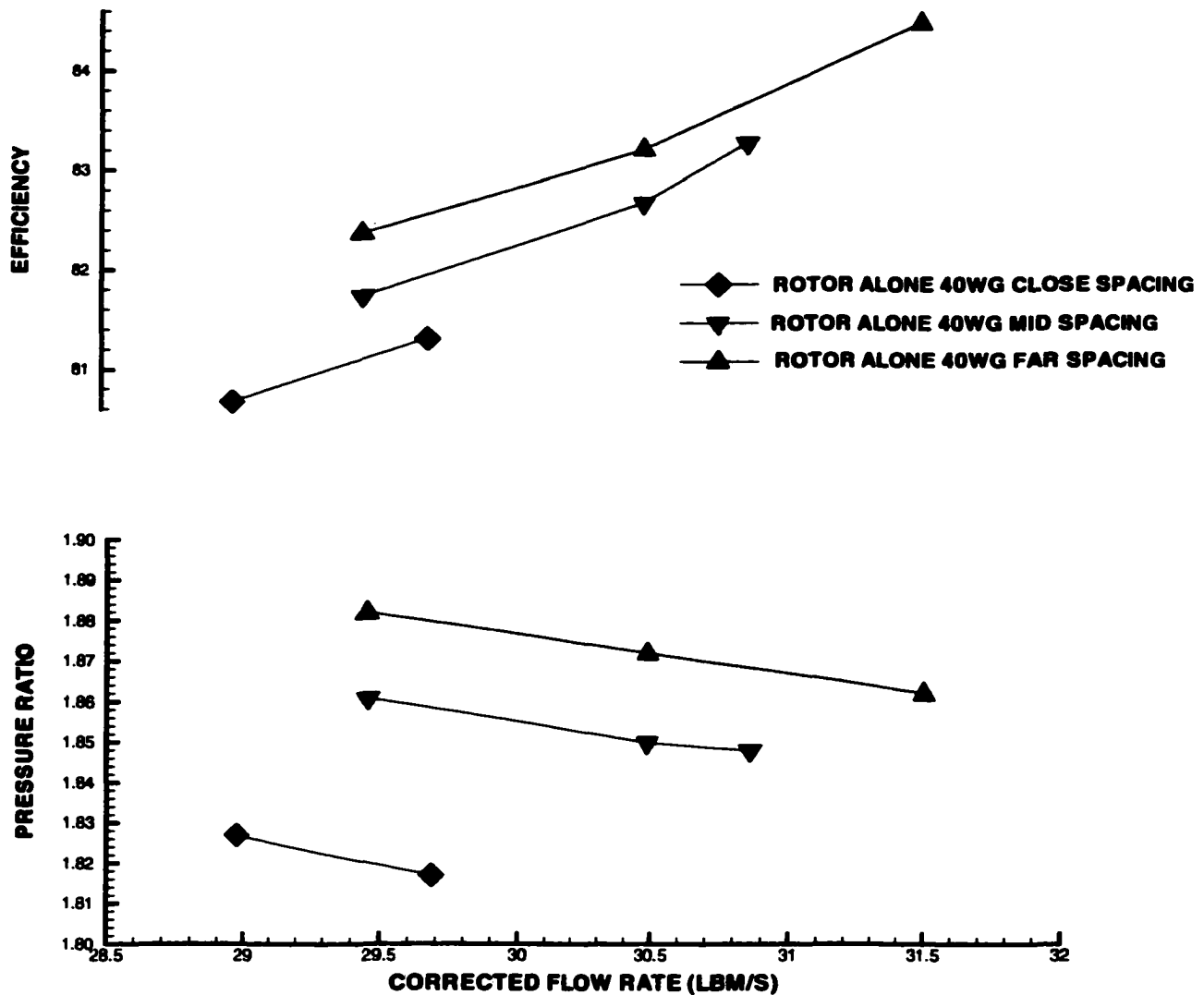


Figure 31. 40 Wake Generator/Rotor Only Performance, 100%  $N_c$

consistent with observations made from the SMI 24 wake generator configuration presented in Figure 27.

The 24 wake generator rotor alone performance is presented in Figure 32. For this case data was only obtained at far and close spacings. Consistent with Figure 31 both pressure ratio and efficiency increased significantly as the blade-row spacing was moved from close to far spacing.

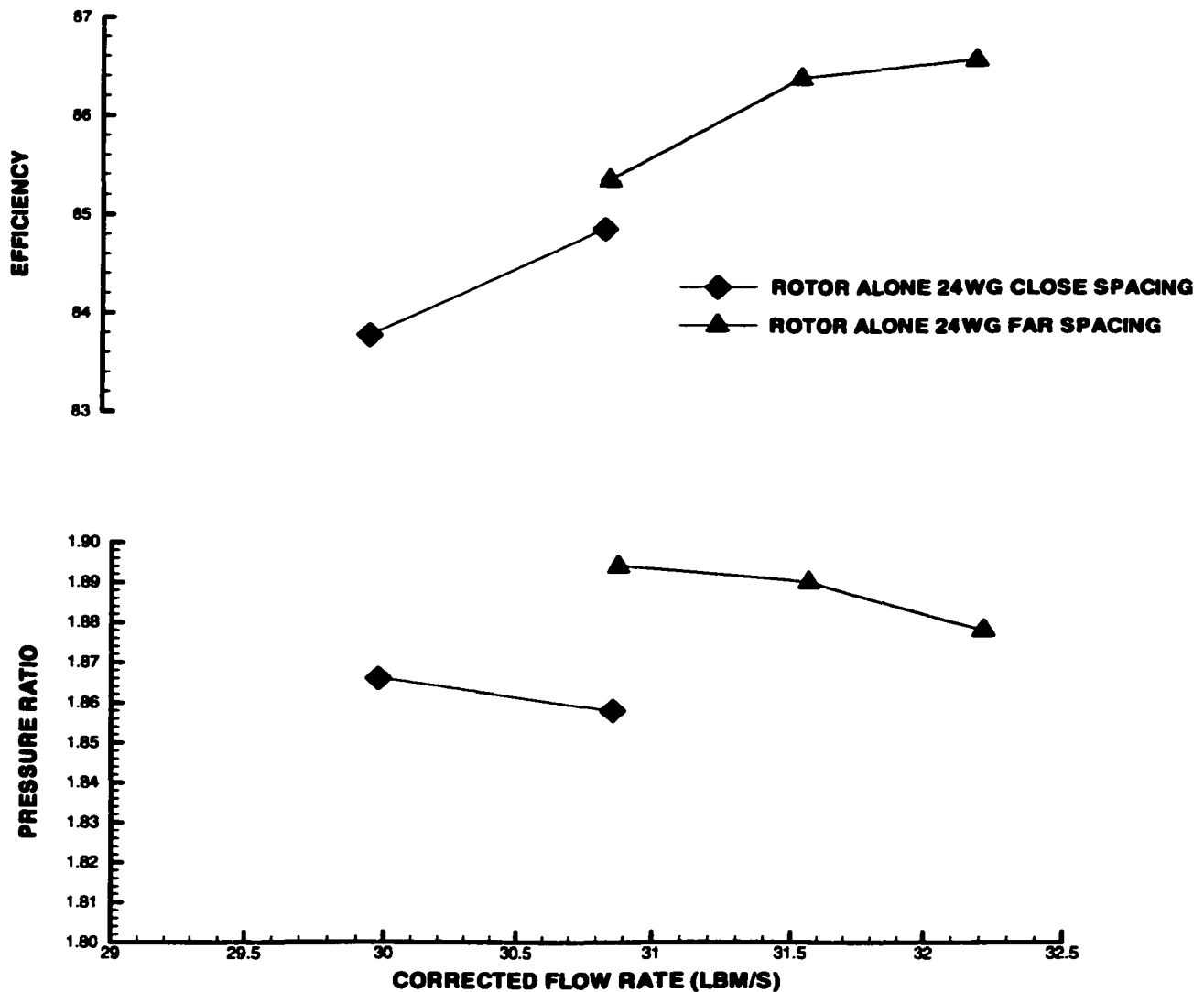


Figure 32. 24 Wake Generator/Rotor Only Performance, 100% Nc

### Performance Summary

Both the SMI results (Figures 26, 27) and the wake generator/rotor only results (Figures 31, 32) show similar trends concerning the effect of blade-row spacing on the performance of a transonic compressor. Figure 33 plots the changes in pressure ratio and efficiency of the SMI rig with spacing for an operating point near peak efficiency at 100% Nc. The error bars define the level of pressure ratio or efficiency change that must be observed to be considered relevant. For the 12 wake generator configuration there

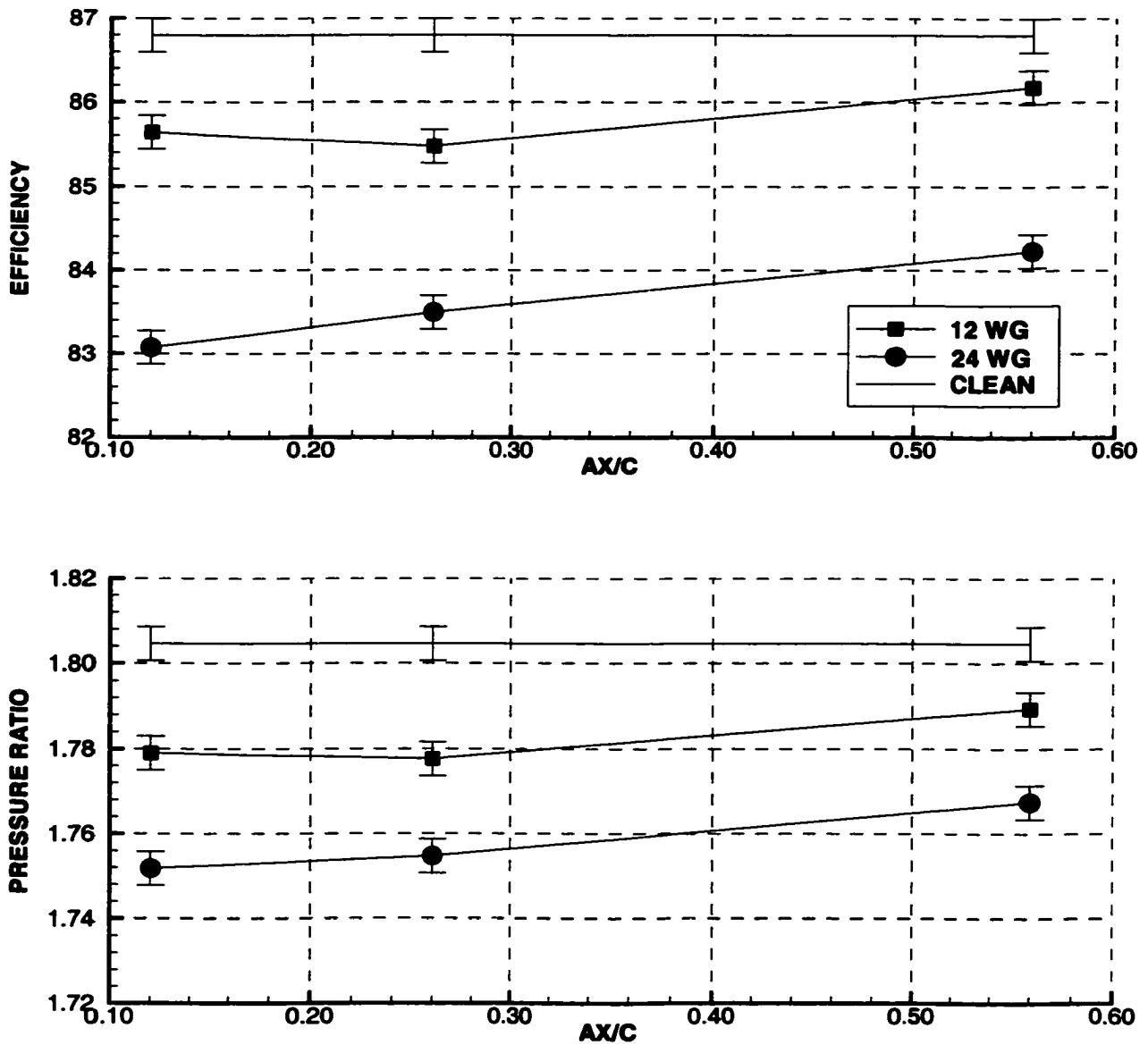


Figure 33. SMI Performance Comparison at Peak Efficiency, 100%  $N_c$

were no differences in performance between close and mid spacing. However there was a measurable decrease between far and close spacing in pressure ratio and efficiency. With 24 wake generators installed the pressure ratio did not change significantly from mid to close spacing but the efficiency did decrease. Significant reduction in pressure ratio and efficiency were observed between far and close spacing.

Figure 34 charts the difference in pressure ratio and efficiency for the wake generator/rotor only 24 and 40 wake generator configurations. The performance at each spacing is compared at similar mass flow rates. For 40 wake generators this was approximately 29.5 lbm/s (see Figure 26) and for 24 wake generators it was approximately 31.0 lbm/s (see Figure 27). Since the 40 wake generator, close spacing data was obtained above and below

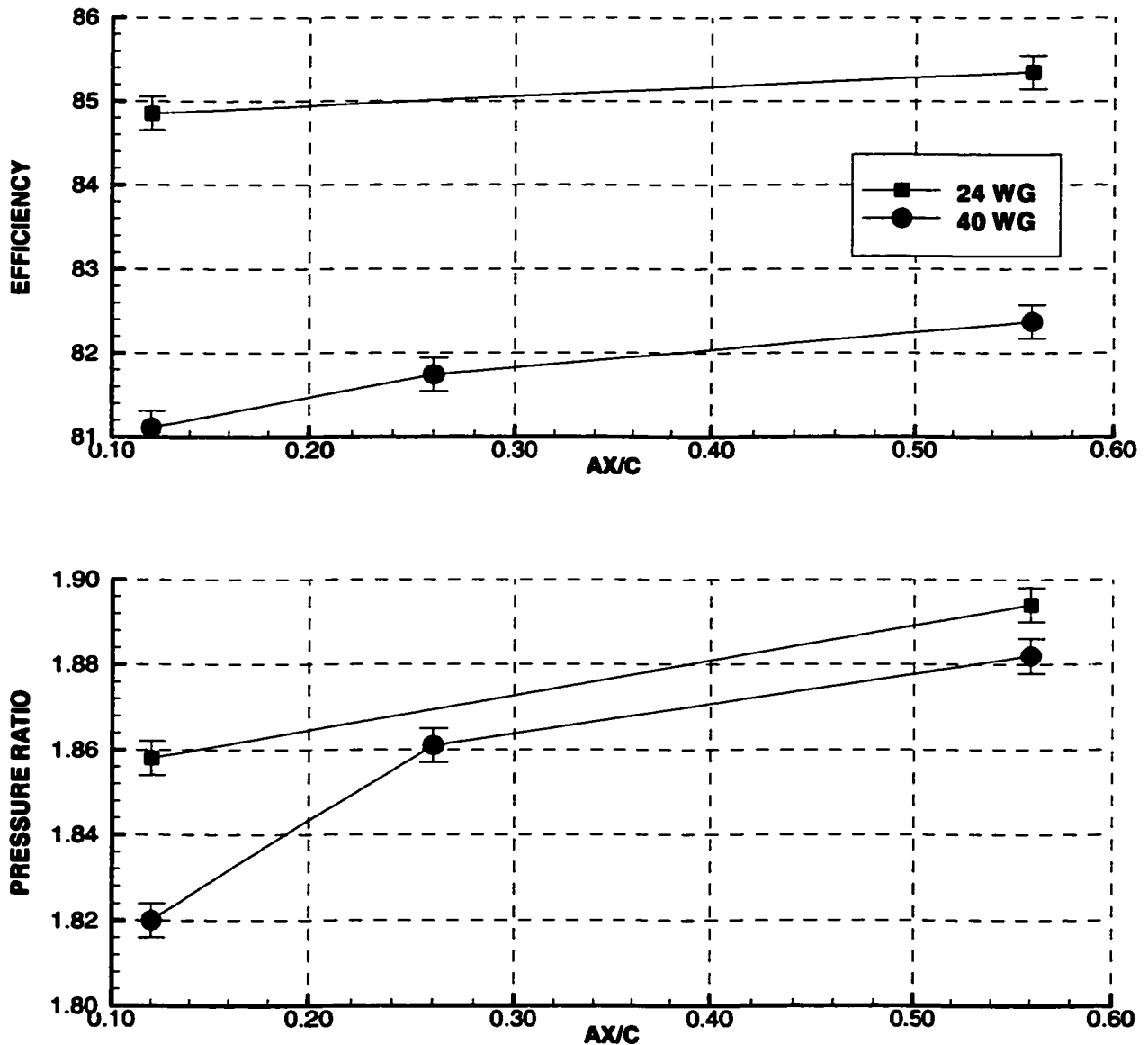


Figure 34. Wake Generator/Rotor Only Performance Comparison at Common Mass Flow Rate, 100%  $N_c$

29.5 lbm/s, a linear interpolation was used to estimate pressure ratio and efficiency at 29.5 lbm/s. Figure 34 shows that a significant reduction in pressure ratio and efficiency were observed for the 24 wake generator configuration as the spacing was reduced from far to close. For 40 wake generators there was a large decrease in pressure ratio and efficiency between mid and close spacing. A significant reduction in pressure ratio and efficiency was also observed between far and mid spacing.

Tables 5 and 6 summarize the performance changes observed for both the SMI and the wake generator/rotor only experimental data. Two trends are observed.

**Table 5. SMI Performance Change Near Peak Efficiency**

	<b>% Decrease From Far Spacing PR</b>	<b>Change in <math>\eta</math> from Far Spacing</b>
12 WG Mid	0.65	- 0.707
12 WG Close	0.58	- 0.540
24 WG Mid	0.72	- 0.735
24 WG Close	0.88	- 1.160

**Table 6. Wake Generator/Rotor Only Performance Change at Common  
Mass Flow Rate**

	<b>% Decrease From Far Spacing PR</b>	<b>Change in <math>\eta</math> from Far Spacing</b>
24 WG Close	1.90	- 0.494
40 WG Mid	1.12	- 0.631
40 WG Close	3.29	- 1.263

One is that pressure ratio and efficiency decrease with reduced blade-row spacing between the wake generator and transonic rotor. The other trend is that pressure ratio and efficiency decrease with increased solidity of the

upstream blade-row. The hypothesis that blade-row interactions are responsible for the decrease in performance is strengthened by these trends. The closer the spacing between blade-rows the stronger the interactions became. If these interactions are some type of wake-rotor, wake-shock, or blade-shock interaction then obviously the more blades in a blade-row the more loss will be produced.

As the corrected speed was reduced the difference in performance with changes in blade-row spacing eventually became insignificant. This suggests that the interaction may be related to the shocks present in a transonic rotor.

Table 7 compares the choking mass flow rate for the 12, 24, and 40 wake generator configurations based on a percent reduction from the

**Table 7. SMI Choking Mass Flow Rate Comparison at 100%  $N_c$**

<b>Configuration</b>	<b>% Reduction from Clean Inlet</b>		
	<b>Close Spacing</b>	<b>Mid Spacing</b>	<b>Far Spacing</b>
12 WG's	0.92	0.90	0.57
24 WG's	2.39	2.26	1.88
40 WG's	4.09	3.51	3.24

Clean Inlet = 34.394 lbm/s

clean inlet value. It is observed that the choking mass flow rate decreases as blade-row spacing is reduced and wake generator solidity is increased. This is a similar trend to that observed with pressure ratio and efficiency. The trend of decreased mass flow rate with increased solidity is expected because more wake generators produce more blockage, thus reducing the effective flow area. Since closer spacing between the wake generator blade-row and the transonic rotor blade-row also decreases the mass flow rate it appears that the blade-row interactions may also produce more blockage. For this reason rotor solidity should also have an effect on the severity of

blade-row interactions because with more rotor blades there are more shocks/bow waves interacting with the upstream blade-row. Changes in mass flow rate with spacing were not significant at part speed. This suggests the increased blockage is not present at subsonic speeds.

The experimental results presented in this section clearly show that a measurable difference is observed when blade-row spacing is varied in a transonic compressor. The magnitude of performance changes observed would have a significant impact on the operation and mission capabilities of military aircraft gas turbine engines. Copenhaver [22] has shown that for a next generation Air Force fighter engine, drops in efficiency, pressure ratio, and mass flow rate at levels observed with the SMI experiment would result in a 2.5% increase in Specific Fuel Consumption (SFC), a 1.7% reduction in net after burner thrust, and a 1.5% drop in thrust-to-weight ratio. In the current development of military compressors industry has often expended tremendous resources to overcome shortfalls in mass flow rate from the design goal. Understanding the affect of blade-row interactions on mass flow rate in transonic fans and compressors would be of great interest to the military and industry.

### **Wake Recovery Analysis**

The observation that the SMI performance decreased as the axial gap between blade-rows was reduced is contrary to the concept of wake recovery and the low speed experimental results presented in the Introduction. The process of wake recovery was shown to improve performance as the axial spacing between blade-rows was reduced. The SMI observations suggested that there was another mechanism beside wake recovery that was affecting the performance of the compressor stage when blade-row spacing was changed.

Using the model of Van Zante et al [9], the potential for wake recovery in the SMI rotor was estimated at 50% span. The model estimates the recovery parameter of two interacting blade rows based on the inlet and exit

velocity triangles and the blade geometry. These input parameters are found in reference [18]. The recovery parameter is proportional to the wake inlet and exit length ratio and describes how much of the wake mixing loss possible is recovered in a reversible manner. At 50% span the recovery parameter was  $-0.18$ , which means there is no reduction in mixing loss as the wake generator wakes passes through the rotor. Consequently, performance gains from wake recovery would not be expected with decreased wake-generator-to-rotor axial gap. Analysis of the model suggests that significant wake recovery is not likely with the zero degree inlet angle of the wake generator wake. Even if the inlet wake angle was not zero, this and other wake recovery models are based on incompressible, inviscid theory and would not account for any shock interactions with the wake generator blade or wake.

## **STEADY-STATE DATA ANALYSIS**

In the previous section it was established that reduced blade-row spacing in the SMI compressor significantly decreased pressure ratio, efficiency, and mass flow rate. The challenge now becomes determining at what location in the compressor the performance decrease occurs. This section begins with an overview of loss in compressors followed by results of a flow swallowing study on the SMI rig that proves loss sources other than mixing do exist. Wake generator/rotor only experimental data are then analyzed to show that the decrease in performance is a result of unsteady interactions between the upstream wake generator and downstream transonic rotor.

### **Loss Overview**

In the Introduction it was explained how wake mixing loss can be affected by blade-row spacing. Additional loss sources exist in a compressor and can be generally grouped (see Cumpsty [23]) as 1) drag at solid surfaces; 2) mixing; 3) shock losses; and 4) shear work. Losses have an effect on blockage (an effective reduction in flow area), pressure rise, work input, and mass flow capacity. At a thermodynamic level Denton [24] has described loss as any flow feature that reduces the isentropic efficiency of a turbomachine. In an adiabatic compressor this translates to thermodynamic irreversibility that creates entropy. The reduced pressure ratio, efficiency, and mass flow rate the SMI rig experienced was a result of increased loss produced when the spacing between blade-rows was reduced.

### **Flow Capacity Experiment**

Results from Chriss et al [21] showed that losses in addition to wake mixing loss occur when the spacing was reduced from far to close. In this experiment the SMI rig was used to evaluate the effect of upstream blade-row wakes on the flow capacity of a downstream stage. This was accomplished by determining the total pressure loss measured from the

wake calibration experiment at distances corresponding to each of the three spacings and correcting the three-blade-row performance for the total pressure deficit at the rotor inlet.

The rotor-stator (or embedded stage) flow capacity at choke for each spacing was then compared and is shown here as Figures 34 and 35. The abscissa is the axial spacing and the ordinate is the choking mass flow rate of a configuration divided by the choking mass flow rate of the clean inlet configuration. An ordinate value of one means the embedded stage passed the same mass flow rate as the clean inlet configuration. If all losses are accounted for the corrected embedded stage should pass at least as much mass flow as the clean inlet case. Values less than one mean that loss sources other than mixing were present and unaccounted for.

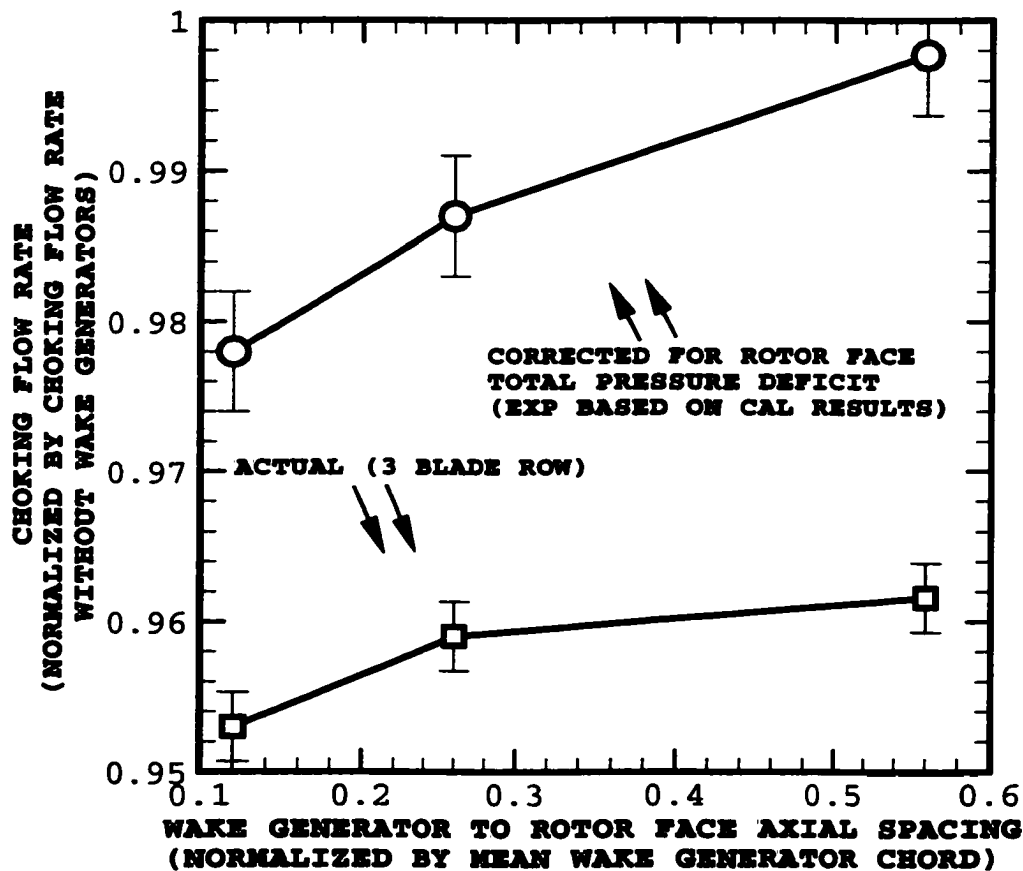


Figure 34. 40 Wake Generator Choking Flow Rate Comparison

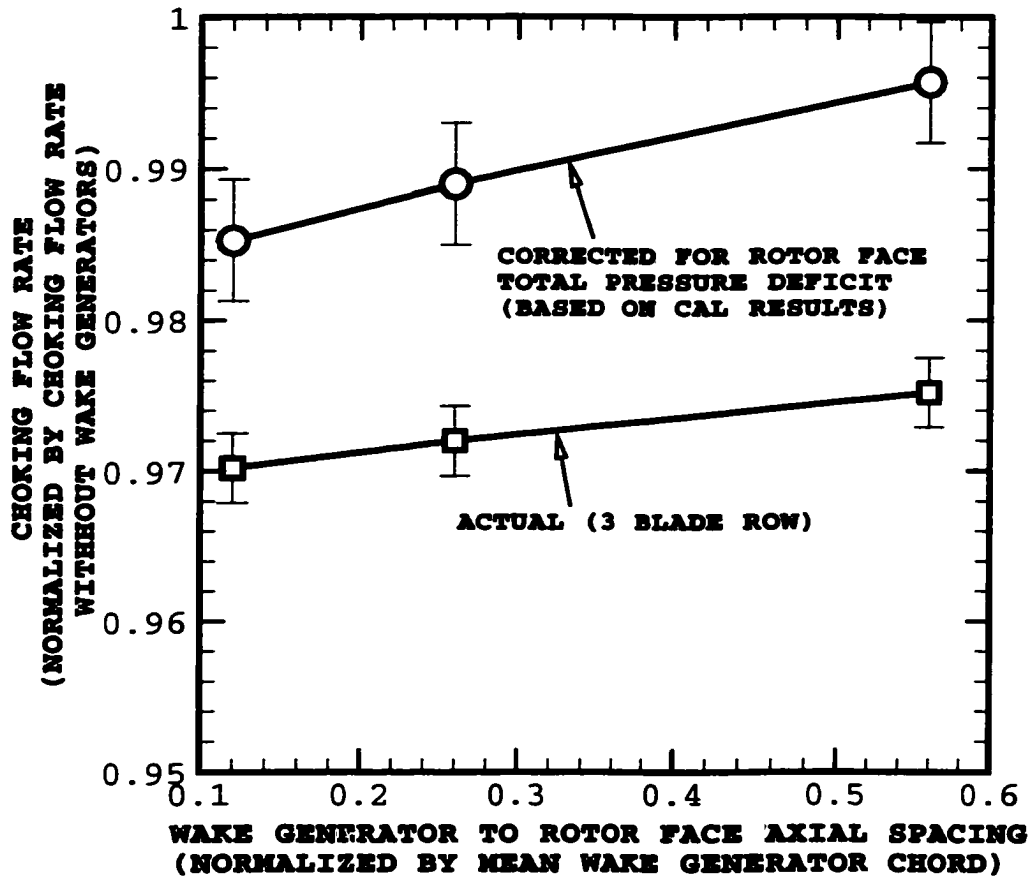


Figure 35. 24 Wake Generator Choking Flow Rate Comparison

At some distance upstream of the rotor there will be minimal blade-row interactions and the loss generated between blade rows will be due to wake generator wake mixing. For the SMI rig this distance is very near far spacing as evidenced by corrected choking mass flow rate near 1. However at mid and close spacings, wake mixing alone does not account for the drop in flow capacity and thus the corrected choking mass flow rate is less than 0.99. Since blade-row spacing between the wake generators and rotor is the only variable, the losses must be a result of some blade-row interactions. Including these losses would increase the corrected embedded stage mass flow rate. The figures also show that the closer the spacing more loss is unaccounted for. Comparing Figures 34 and 35 it is observed that there is more blade-row interaction loss in the 40 wake generator configuration than

the 24 wake generator configuration. This is expected since with more wake generators more blade-row interactions take place.

### **Wake Generator/Rotor Only Analysis**

Experimental data acquired during the wake generator/rotor only testing further aid in determining where in the compressor extra loss was produced. Measurements made by the traverse rake located 0.93 rotor chords downstream of the rotor (see Figure 11) were circumferentially averaged to produce radial profiles of pressure ratio and efficiency. Profiles for the 40 wake generator configuration are shown in Figure 36. These profiles correspond to the data points presented in Figure 31 at similar mass flow rates for each spacing. For the 40 wake generator comparison the mass flow rate was near 29.5 lbm/s.

Inspection of Figure 36 shows that the close spacing pressure ratio profile is different in shape compared to the mid and far spacing profiles. There exists a major reduction between 10% and 75% span. The mid spacing profile is similar in shape to the far spacing but of reduced magnitude. The efficiency profiles show a reduction in efficiency between 10% and 70% span. Interestingly, the efficiency at the tip-most rake element shows a substantial increase at close spacing. Thus, even though the overall performance of the SMI rig suffers with reduced blade-row spacing, there is some benefit near the casing.

Profiles for the 24 wake generator configuration are shown in Figure 37. These profiles correspond to data presented in Figure 32 near a mass flow rate of 31.0 lbm/s. The trends are similar to those observed with 40 wake generators but the differences between spacings are smaller in magnitude. It is also apparent that the pressure ratio profile does not show as large a deficit over as much span as the 40 wake generator pressure ratio profile. The 24 wake generator configuration pressure ratio profile is reduced between 40% and 80% span. Figure 37 shows similar trends in

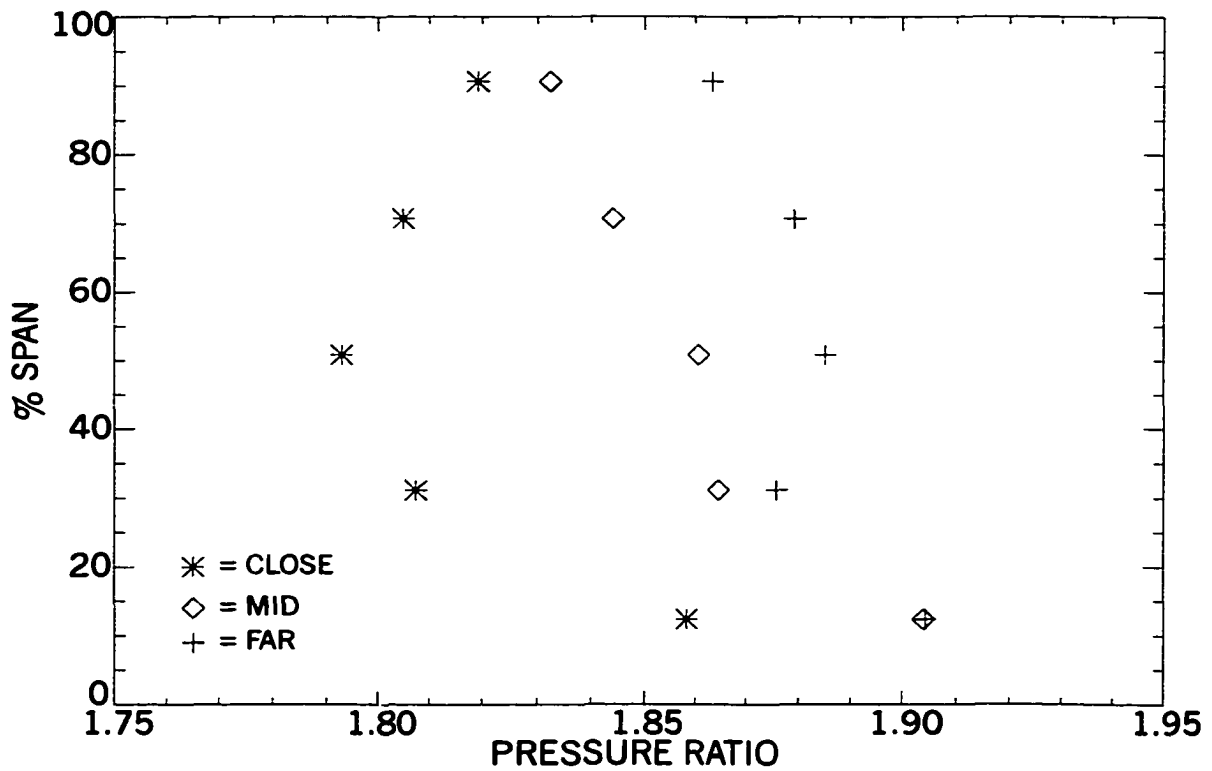
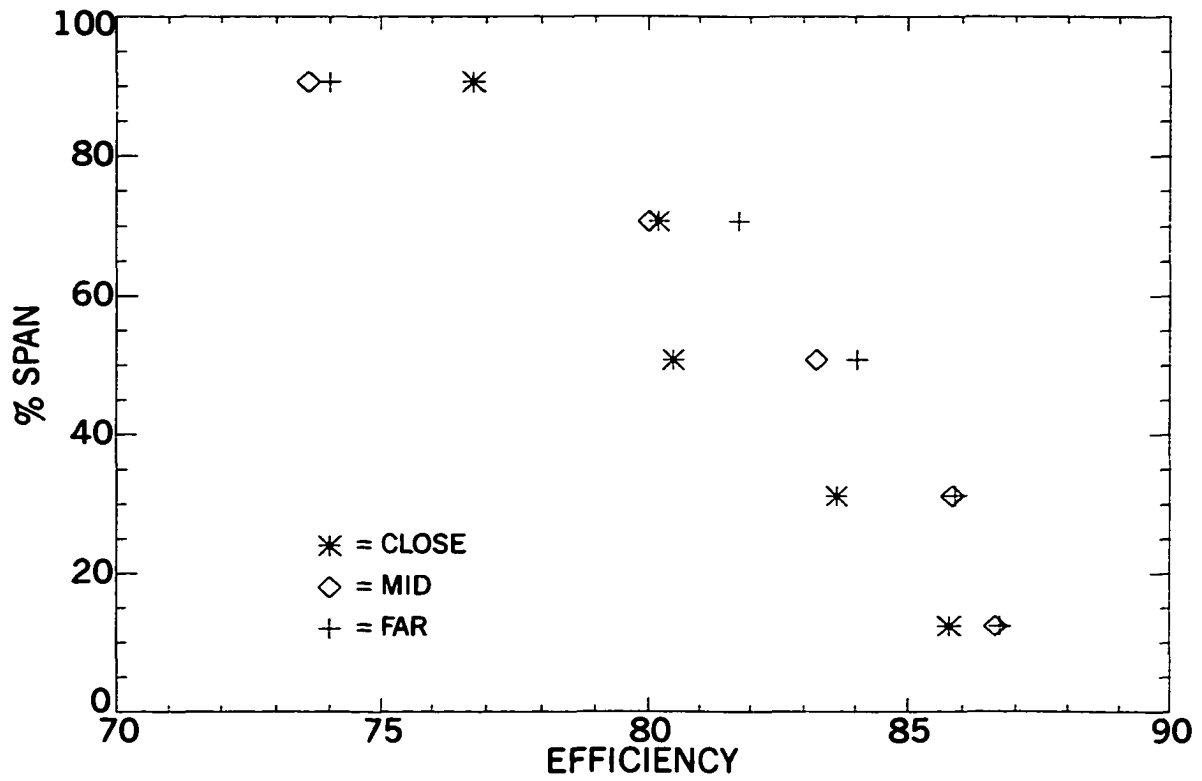


Figure 36. 40 Wake Generator Profile Comparison at 29.5 lbm/s

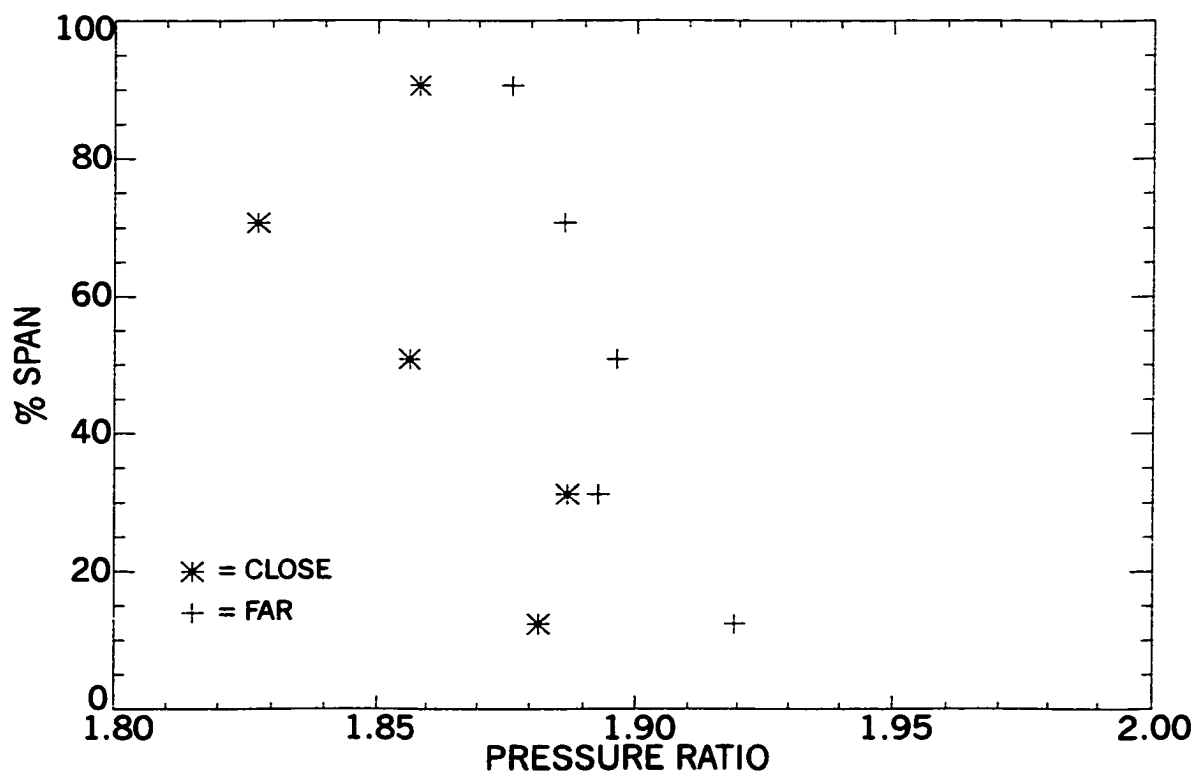
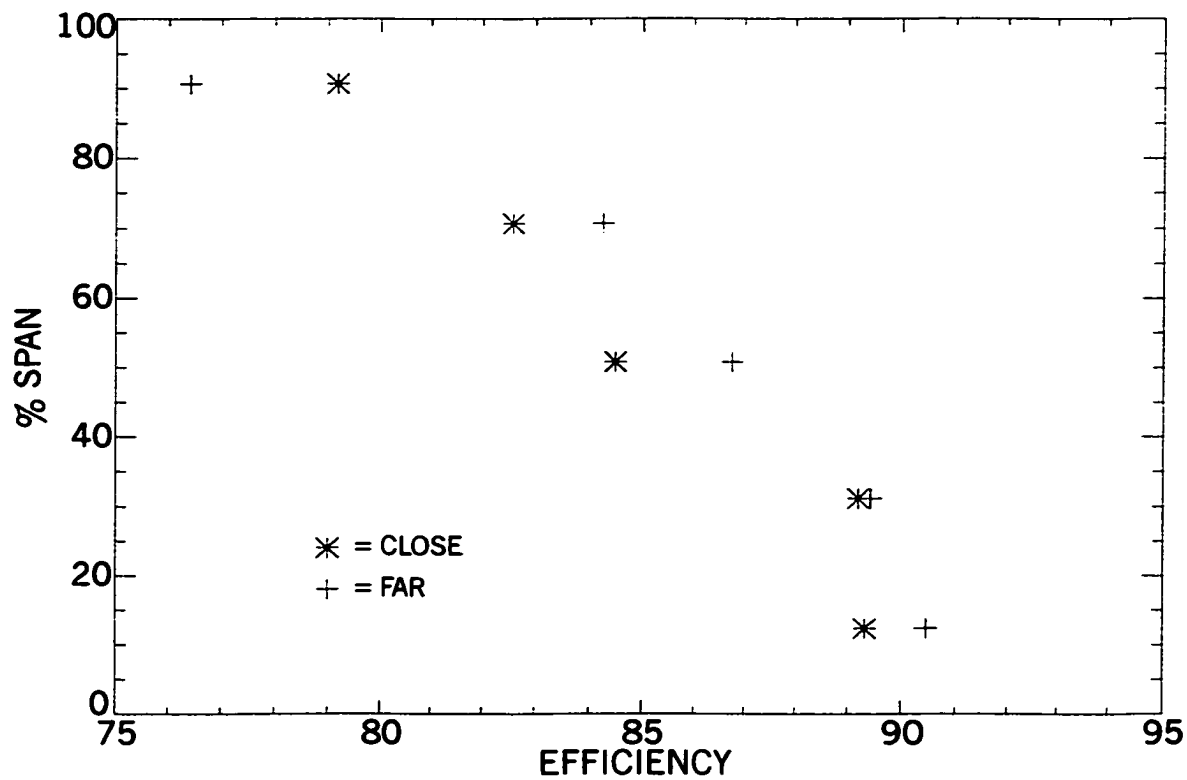


Figure 37. 24 Wake Generator Profile Comparison at 31.0 lbm/s

the efficiency profile with an increase in efficiency at the tip as noted in Figure 36 is still present.

In order to determine whether the change in shape of the pressure ratio profile is due to spacing changes and not a result of the compressor operating at a different location on its characteristic for different spacings, pressure ratio and efficiency profiles at various mass flow rates for a given spacing were analyzed. Plots of this data are presented in Figures 38 – 40 for the 40 wake generator configuration. Comparing the three figures it is obvious that the profile shape does not change appreciably with mass flow rate but the magnitude of the pressure ratio and efficiency does. Due to the fact that the wake generator/rotor only experiment was only able to operate past peak efficiency, the general trend is that as mass flow rate was lowered the pressure ratio increased and the efficiency decreased. The same observations are made for the 24 wake generator configuration pressure ratio and efficiency profiles. These plots are presented in Appendix B. It can be concluded that the change in profile shape at a similar mass flow rate is due to changing the axial gap between blade-rows from far to close spacing.

**Contour Plots of Pressure Ratio and Efficiency.** Further insight into the cause of performance reduction with decreased blade-row spacing is gained by analyzing contour plots of pressure ratio and efficiency from the wake generator/rotor only steady-state traverse rake measurements. Since the greatest differences in performance were found between close and far spacing, results from those two data sets at a common mass flow rate of 29.5 lbm/s are presented. The 40 wake generator configuration is analyzed since more wake generator wakes are visible over the range traversed by the CTA rake.

Figure 41 plots the contours of pressure ratio and efficiency at close spacing. The wake generator wakes are distinguishable in Figure 41a as four regions of high gradients leading to an area of low pressure ratio. The

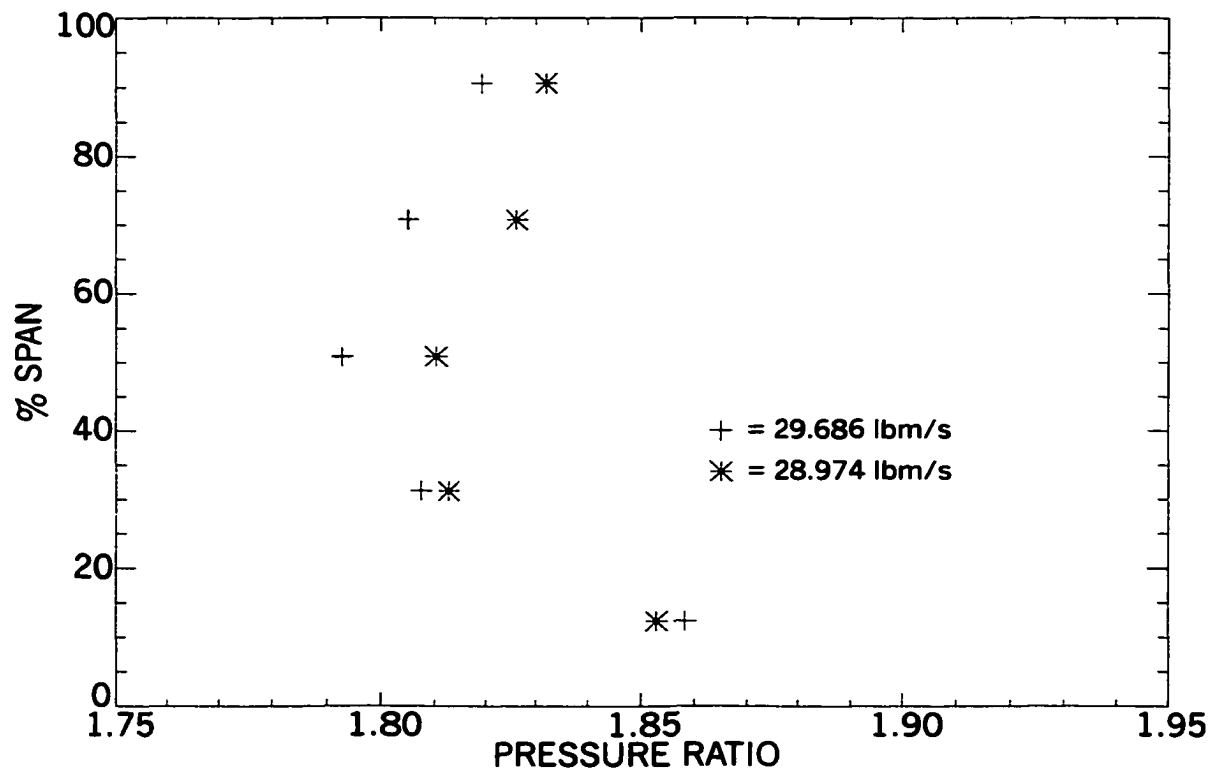
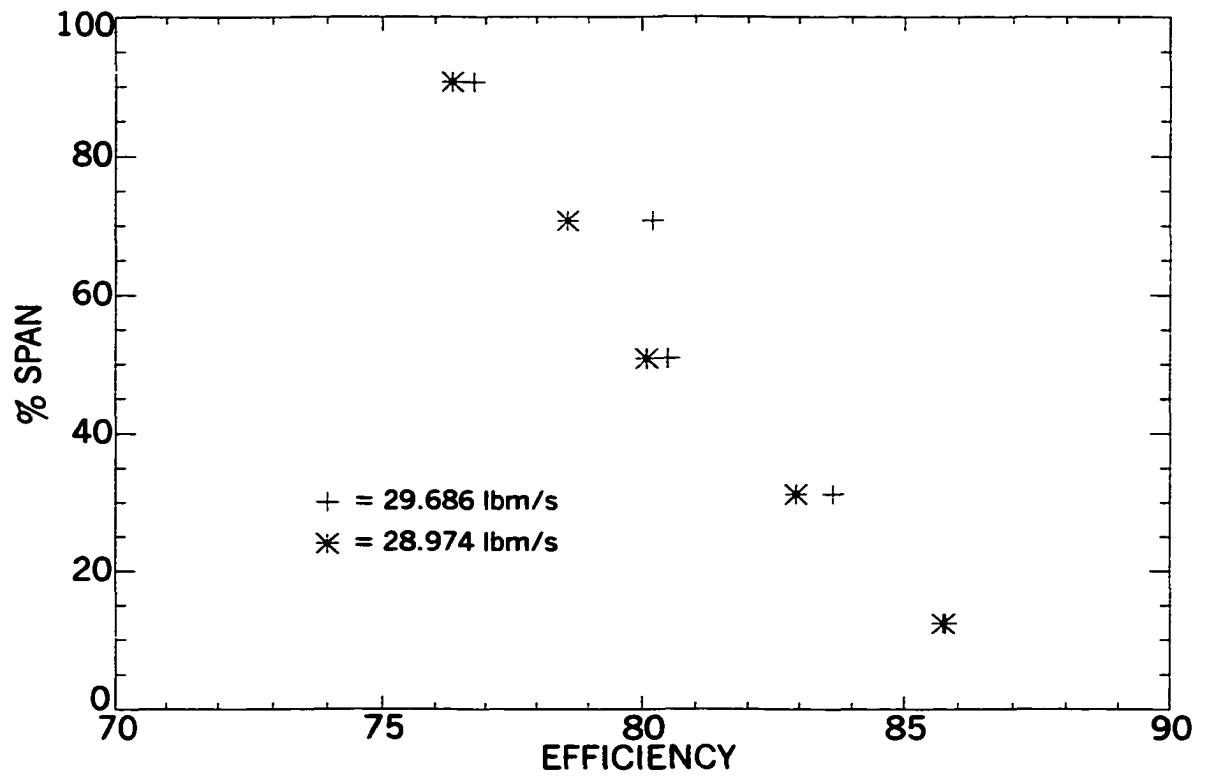


Figure 38. 40 Wake Generator Performance Profiles at Close Spacing

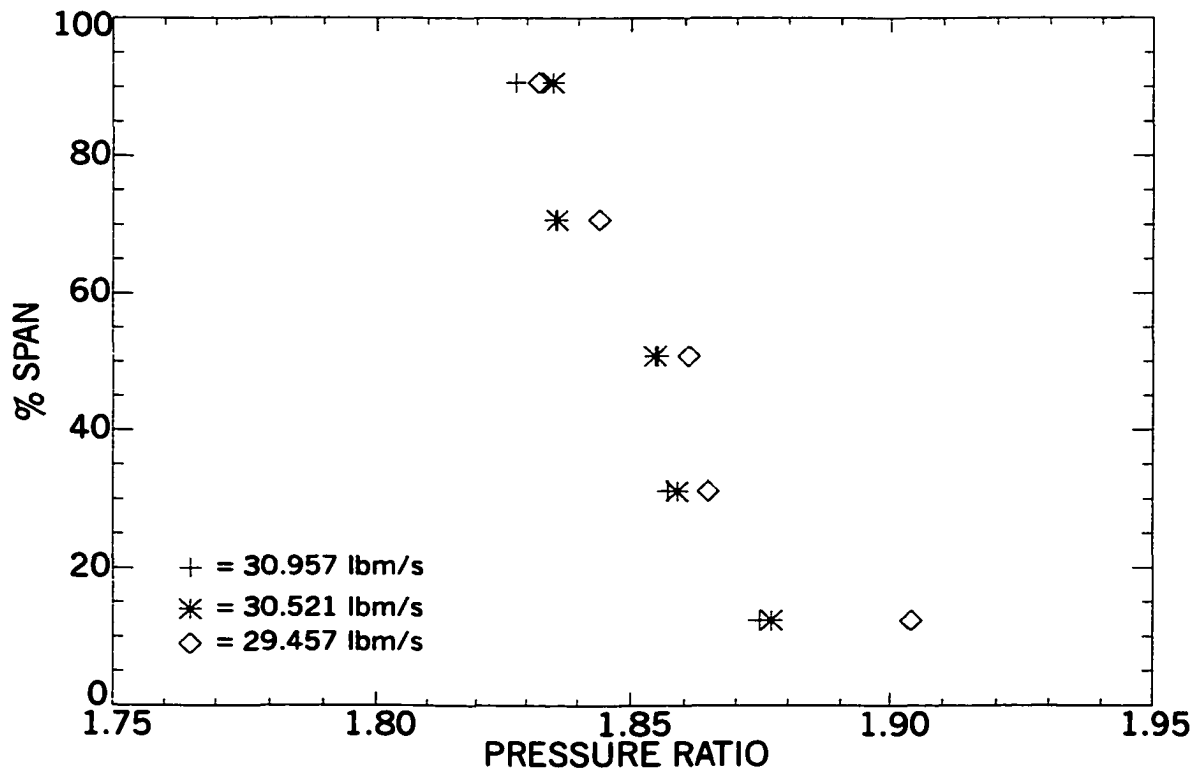
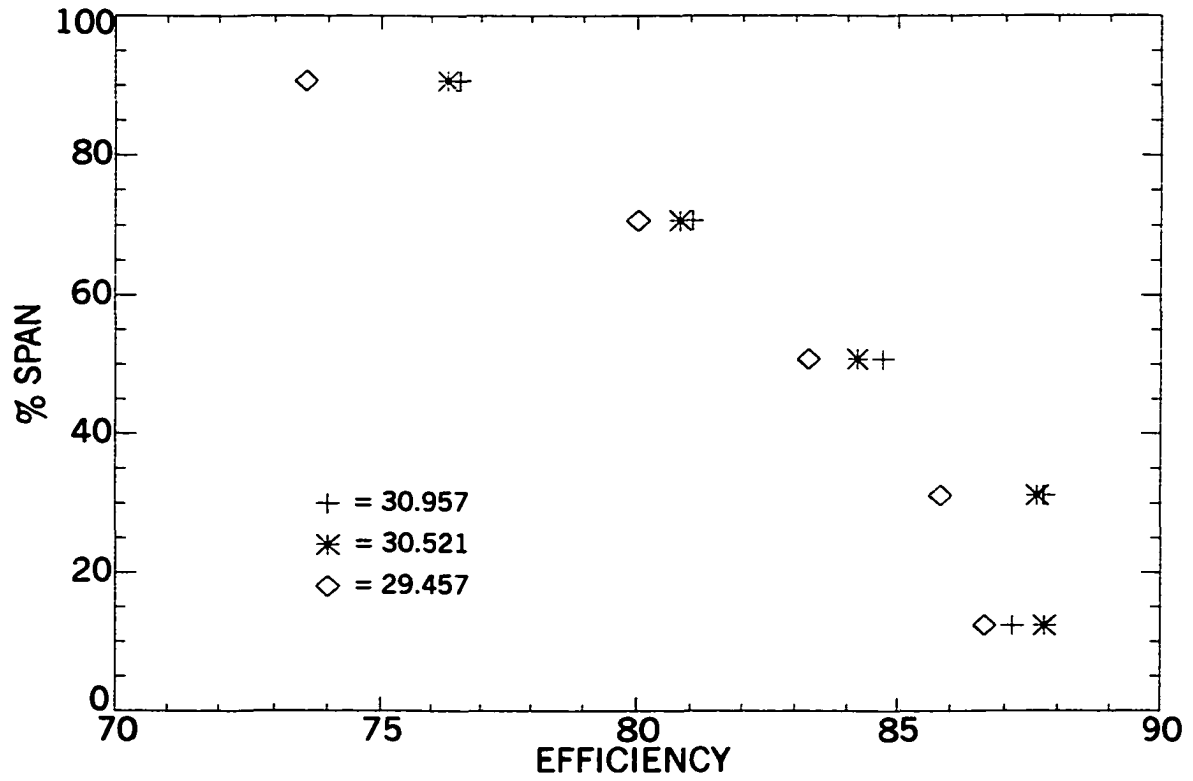


Figure 39. 40 Wake Generator Performance Profiles at Mid Spacing

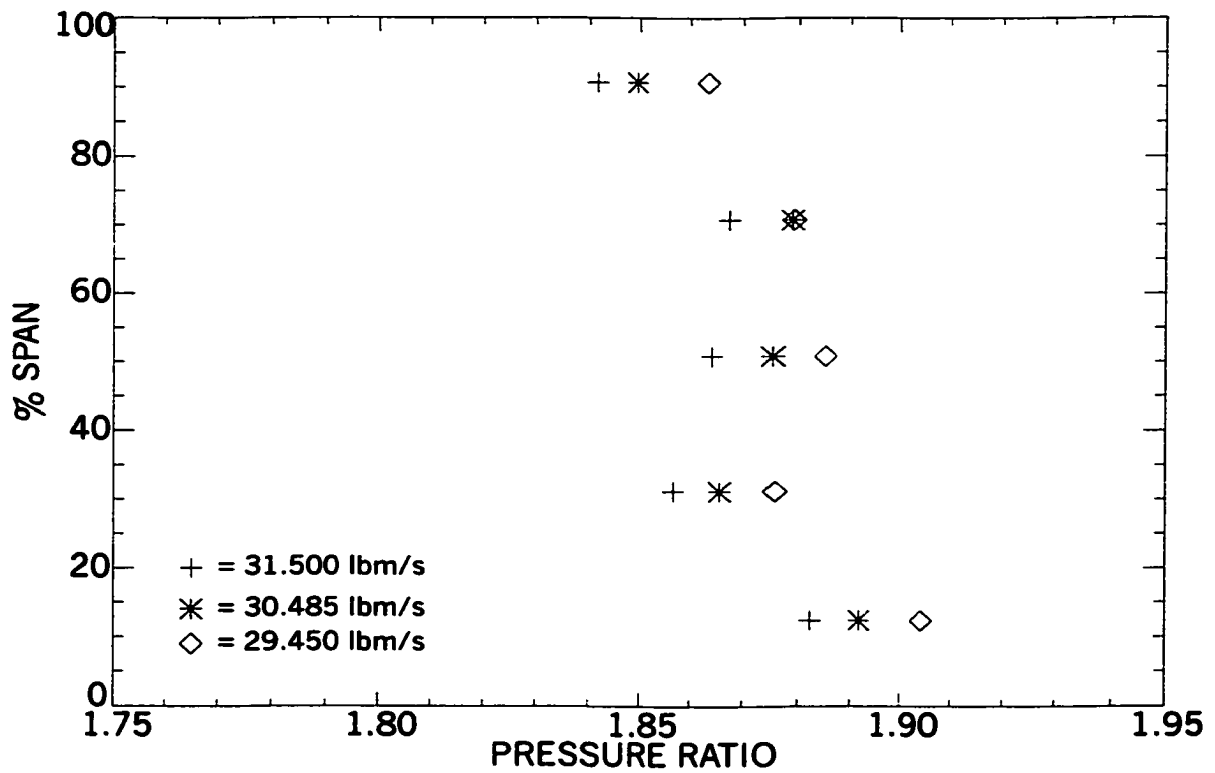
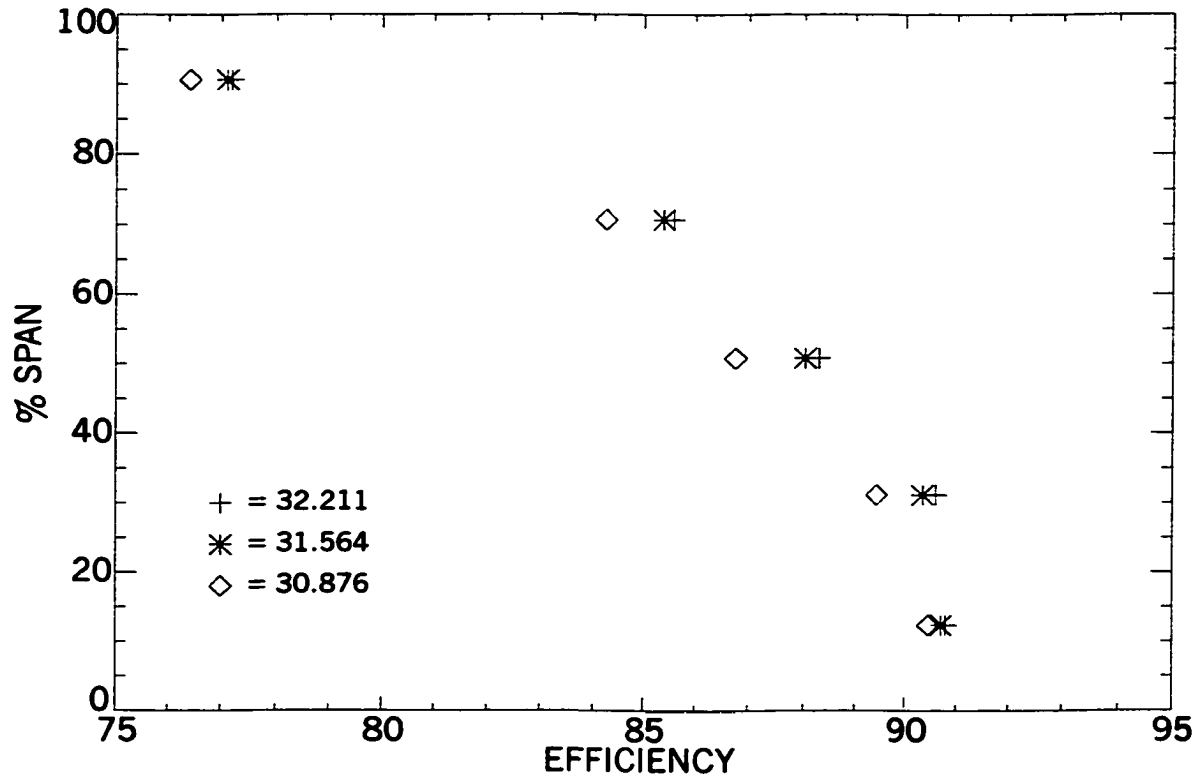
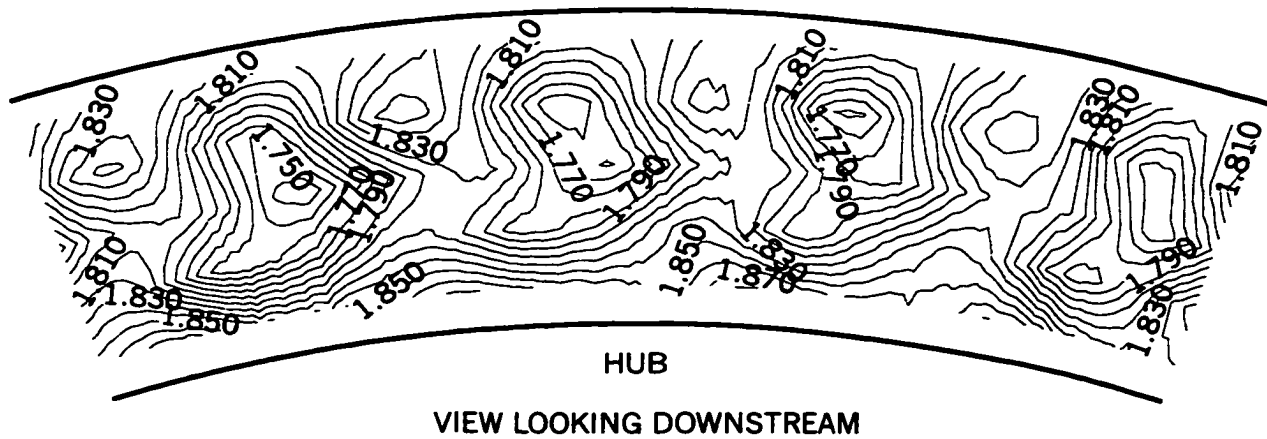


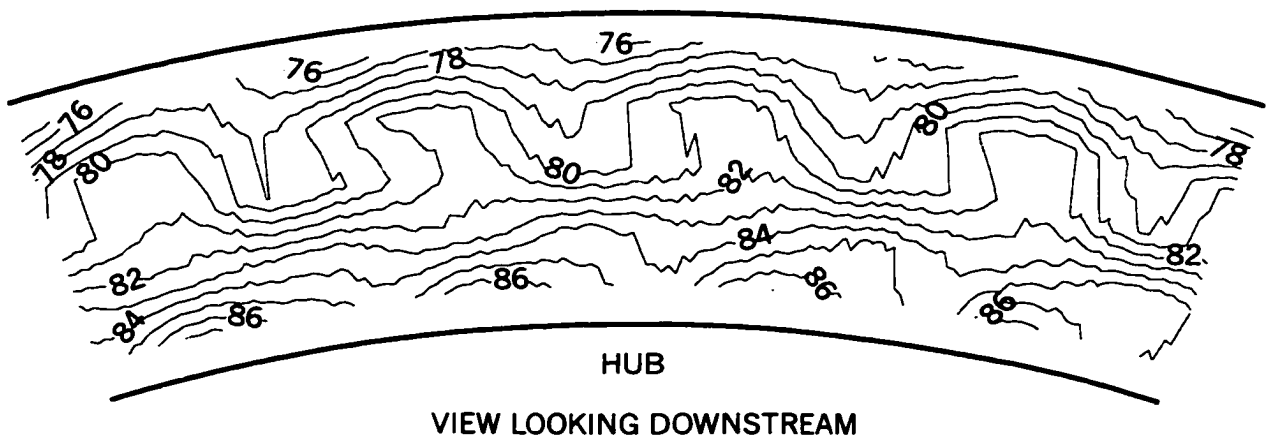
Figure 40. 40 Wake Generator Performance Profiles at Far Spacing

CASE



a) Pressure Ratio

CASE



b) Efficiency

Figure 41. 40 Wake Generator Performance Contours, Close Spacing

pressure ratio is lowest within the wakes between 25% and 75% span. In Figure 41b the efficiency contours demonstrate a similar pattern in that the wakes are visible as pockets of reduced efficiency coincident with the regions of low pressure ratio.

Contours at the far spacing configuration are shown in Figure 42. The wakes are still evident in Figure 42a where regions of lower pressure ratio are visible. However, the steep gradients are no longer present and the difference in pressure ratio between the freestream and wake is much less

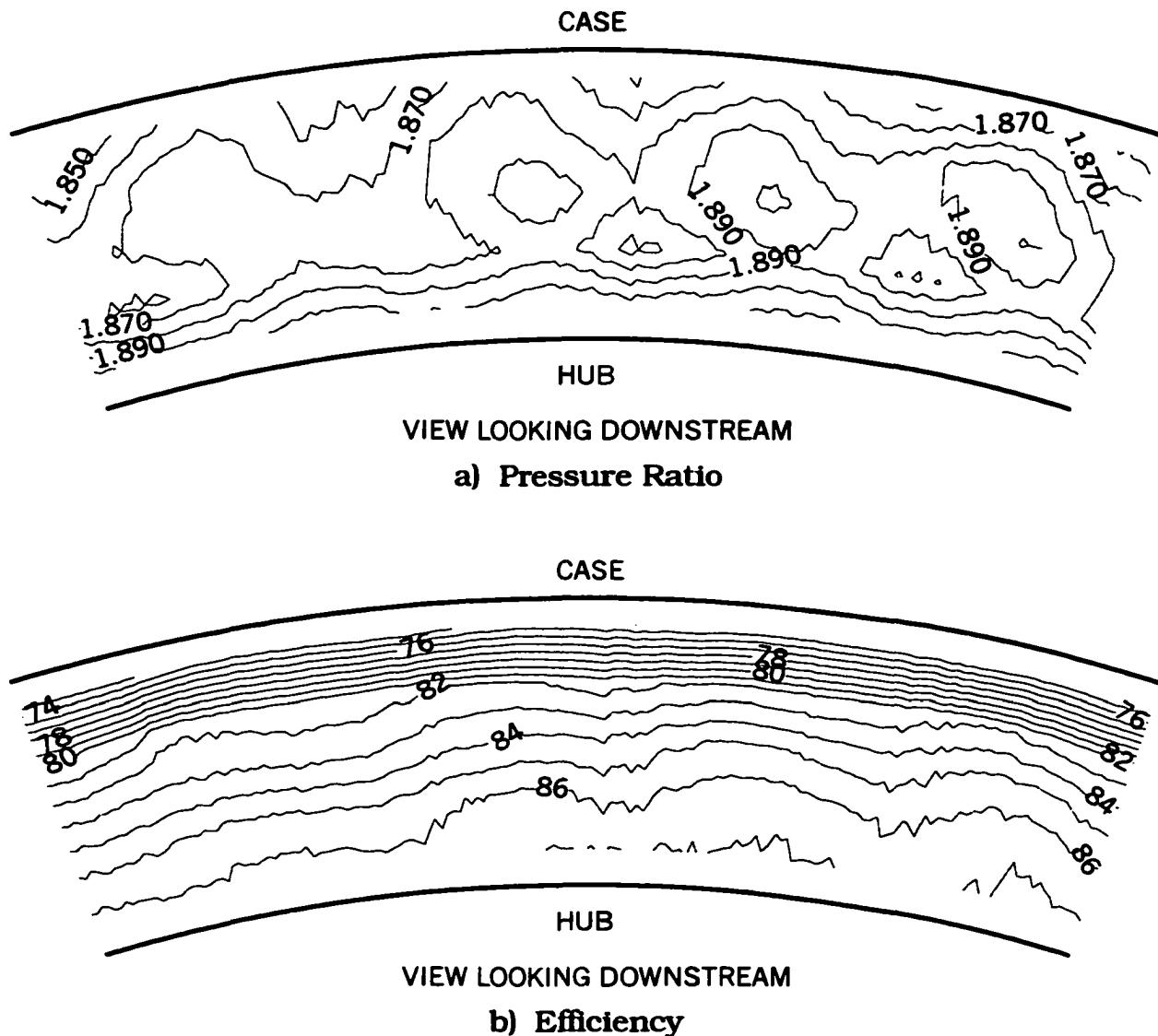


Figure 42. 40 Wake Generator Performance Contours, Far Spacing

than for close spacing. In Figure 42b the pockets of reduced efficiency are not visible. The efficiency contours have a radial profile decreasing from hub to tip. The only evidence of wakes is the sinusoidal-like wave pattern evident between 30% and 70% span.

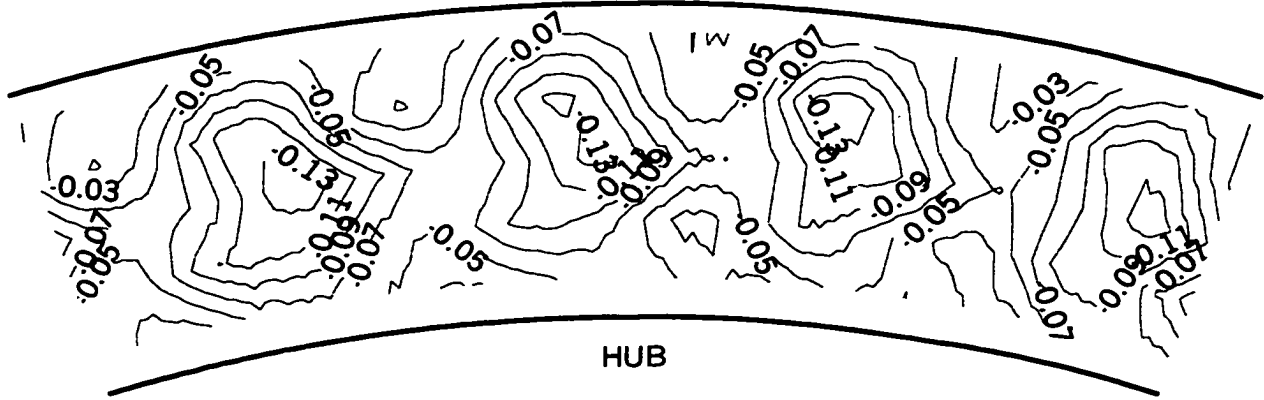
At far spacing the wakes have nearly mixed out before entering the rotor and therefore are not very distinguishable downstream of the rotor. In the close spacing configuration the wakes have not mixed out very much

before entering the rotor and thus are clearly visible in downstream of the rotor.

It is possible to remove the steady-state rotor flow field common to both spacings and isolate the regions of increase loss as spacing is reduced from far to close. This is accomplished by subtracting point by point the far spacing data from the close spacing and plotting the resulting difference contours. Figure 43 shows the result of subtracting Figure 42 from Figure 41. In Figure 43a the entire flowfield has reduced (negative difference) pressure ratio but the largest differences correspond to the 4 wake regions noted in Figure 41. In Figure 43b there are both gains (positive difference) and drops in efficiency. The greatest reductions once again correlate with the location of the wake generator wakes. The gains, although significant in magnitude, are only evident above 90% span. Since it has been established that the overall area-average efficiency at far spacing was more than 1 point greater than close spacing for the SMI and wake generator/rotor only experiments, the increase in tip efficiency shown in Figure 43b was deemed a secondary effect and was not analyzed in more detail. However, future research as to the cause of the increase may prove beneficial.

The experimental results presented in this section show the general location of increased loss production and suggest that the increased loss is a result of blade-row interactions. The flow capacity experiment of Chriss et al [21] revealed that loss in addition to mixing loss is present when the blade-rows are close together. The radial profiles illustrate that the extra loss production occurs between the wake generator blade-row and transonic rotor blade-row and is most significant in the mid-span region. The differencing contours further suggest that blade-row interactions are responsible for the additional loss production and that these blade row interactions are related in some manner to the wake generator wakes. To determine the blade-row interaction mechanism responsible for the increased loss production an unsteady CFD simulation was carried out.

CASE

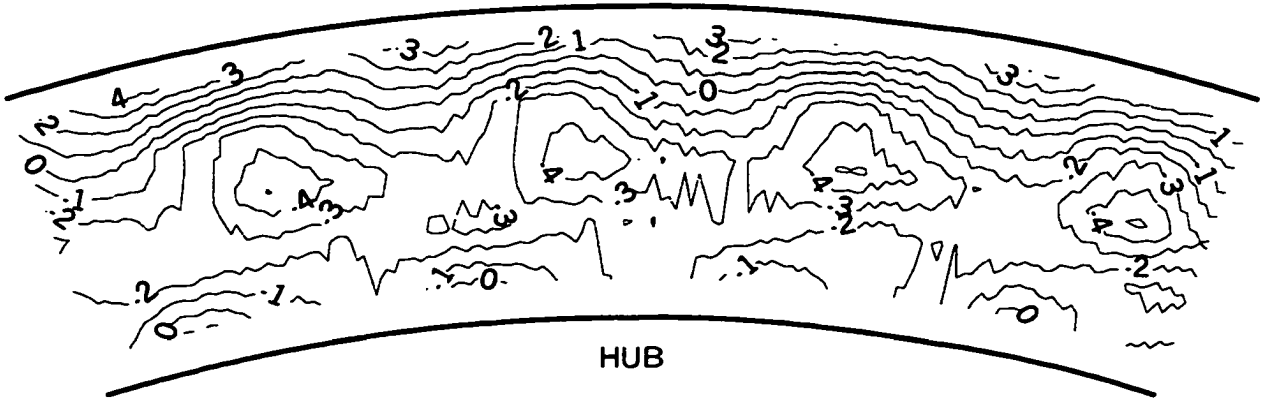


HUB

VIEW LOOKING DOWNSTREAM

a) Pressure Ratio Difference

CASE



HUB

VIEW LOOKING DOWNSTREAM

b) Efficiency Difference

Figure 43. 40 Wake Generator Performance Differences, Close - Far Spacing

## **NUMERICAL APPROACH**

To study in greater detail the unsteady fluid mechanics of the interaction between the wake generator and rotor, numerical simulations of the SMI rig were carried out. This section will introduce the code used to perform the simulations and explain the steps taken to obtain a converged solution.

### **MSU-TURBO**

The CFD program used for the simulations was MSU-TURBO Version 4.1. The principal architect is J. P. Chen from Mississippi State University with funding provided by NASA Glenn Research Center. MSU-TURBO [25-27] is a three-dimensional, viscous, time-accurate code that solves the Reynolds Averaged Navier-Stokes (RANS) equations in the rotating frame of reference. The solution algorithm is an implicit finite volume solver and turbulence modeling is accomplished with either the Baldwin-Lomax or  $k-\epsilon$  model. Axial communication between blade rows is through a sliding interface that does not distort the grid.

MSU-TURBO can model the unsteady blade-row interaction using any one of three methods: full or periodic simulation, time-shift boundary, and wake-blade interaction. The simplest method is the wake-blade interaction. It consists of modeling a single blade-row with unsteadiness introduced through a time-dependent inlet or exit boundary condition. The effect of incoming waves from either the upstream or downstream blade row is taken into account with the boundary condition, however the effect of waves communicating back and forth between blade-rows is not captured with this method.

Wave interactions between blade-rows can only be accurately resolved if the exact blade counts are modeled. If this is done the effect of wakes convected downstream and the potential effects that propagate upstream and downstream will be accounted for. This is the purpose of the full or

periodic simulation method. With a time-accurate, three-dimensional RANS code it is computationally impractical to model each blade in every blade-row. To help reduce the computer resources required the number of blades modeled is therefore based on the geometric periodicity of the configuration.

**Phase-Lag Boundary Conditions.** If phase-lag boundary conditions are applied at the circumferential and axial block interfaces only one blade passage from each blade row is required to model the unsteady blade-row interaction. The time-shift boundary method uses phase-lag boundary conditions that greatly reduce the computational cost of a simulation compared to the periodic method. Phase-lag boundary conditions assume that the unsteadiness of the blade-row interaction solely depends on the blade passing frequency of the adjacent blade-row and its higher harmonics. As a consequence this method does not capture the details of unsteady flow features such as vortex shedding and flow separation. However, as shown by Chen and Barter [26], even if non-deterministic flows are present the phase-lag method produces overall numerical results similar to that of the periodic solution. Phase-lag boundary conditions are most useful when the blade-row interaction is dominated by the unsteadiness at the adjacent blade passing frequency. Flow visualization techniques applied by Estevadeordal et al [28] confirm that this is indeed the case with the SMI rig at the operating conditions modeled with MSU-TURBO.

### **Initial Solution**

Building an initial solution consists of defining a mesh for each blade-row and constructing a flow field on those meshes. The initial solution for the SMI rig was obtained using the method and computer programs of Van Zante [29]. This technique generates a starting flow field for MSU-TURBO from a converged APNASA solution and mesh. APNASA is a code developed by Dr. John Adamczyk of NASA Glenn Research Center using the average passage formulation [1] of the Navier-Stokes equations. The average passage procedure models the time-averaged flow field in a multistage

compressor using body forces and deterministic stresses to account for the presence of neighboring blade rows. While accounting for many of the effects of blade-row interactions, the average passage model still depends on correlations to model the deterministic stresses. APNASA has enjoyed great success as a tool to analyze and design multistage turbomachinery [2].

**Meshes.** The MSU-TURBO wake generator and rotor meshes were created as a subset of the meshes used by the APNASA simulation of the SMI rig. APNASA and MSU-TURBO are both restricted to using a sheared H-mesh. The number of nodes in the spanwise (or radial) and pitchwise (or tangential) directions were kept the same as the APNASA mesh. To help minimize computer resources required to run MSU-TURBO, the number of nodes in the axial direction was reduced from the APNASA mesh. Like most steady CFD codes APNASA meshes extend far upstream and downstream of each blade row. For the MSU-TURBO simulations the meshes were terminated shortly upstream of the wake generator and downstream of the rotor. Although flow gradients still existed at these axial locations, perturbation type [25, 26] non-reflective boundary conditions are used at the upstream and downstream boundaries, which allows the MSU-TURBO mesh boundaries to be in areas of moderate to high gradients without adversely affecting the solution.

One variable in setting up a mesh for MSU-TURBO is the location of the sliding interface between blade-rows. For these simulations the sliding interface was chosen to be close to the rotor leading edge in order to preserve the wake features of the wake generator. The aim was to keep the mesh density high in the wake region to reduce the numerical dissipation of the high gradient wake flow features. Figure 44 shows the close spacing mesh at 75% span. Two blade passages are included so that the blade shapes are discernable. The ratio of grid points to spacing was kept constant between the meshes of the close and far models. The

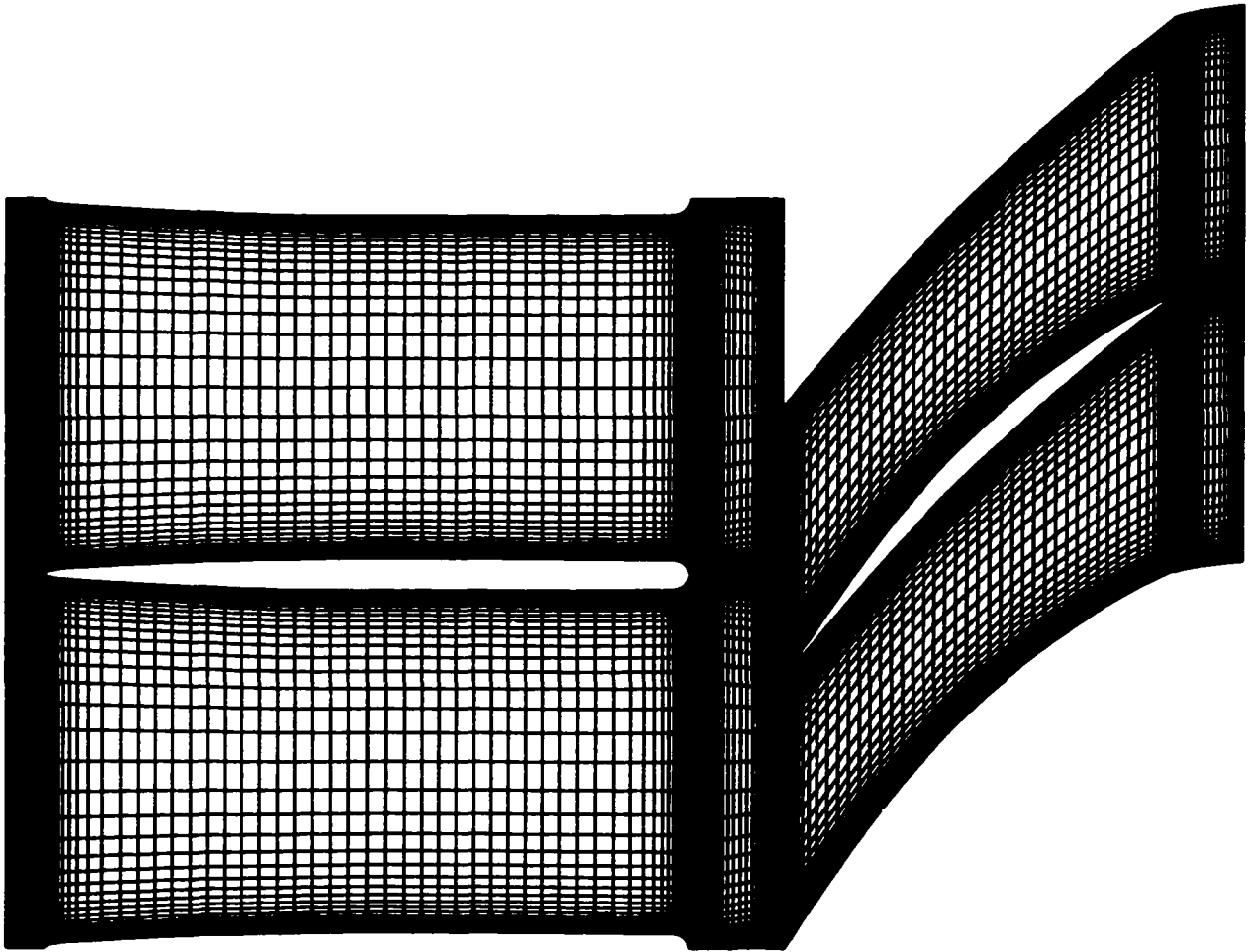


Figure 44. Close Spacing Mesh at 75% Span

location of the sliding interface for the far mesh was chosen to be the same percent gap downstream of the wake generator (or upstream the rotor) as it was for the close mesh. The meshes used for each simulation are provided in Table 8. The mesh sizes are ordered in terms of the number of axial, radial, and tangential nodes.

**Flow Field Construction.** Once the MSU-TURBO meshes were built, the next step was to create a flow field on the new meshes. The first step was to interpolate the APNASA wake generator flow field onto the rotor mesh. The second step was to subtract the axisymmetric average of the

**Table 8. MSU-TURBO Mesh Sizes**

<b>Simulation</b>	<b>Wake Generator</b>	<b>Rotor</b>
<b>Close Spacing</b>	<b>126x51x41</b>	<b>97x51x41</b>
<b>Far Spacing</b>	<b>138x51x41</b>	<b>99x51x41</b>

wake generator flow field from that interpolation. This left only the perturbations due to the wake generator (most notably the wakes) on the rotor mesh. The final step was to interpolate the APNASA rotor flow field on the MSU-TURBO rotor mesh.

The time-shift boundary method requires that additional flow field time information of be stored [26,29]. The time-shift boundary information contains the time history of what happened on the passage boundaries during the previous blade passing.

Once the initial solution of the rotor was obtained, the same procedure was used to create a flow field on the wake generator MSU-TURBO mesh thus completing the initial solution for a simulation.

### **SMI Simulations**

Simulations were run at operating points based on an APNASA solution near peak efficiency at 100% corrected speed for the close and far spacing 24-wake generator configurations. In a separate research effort using the SMI rig, Digital Particle Image Velocimetry (DPIV) data was acquired between the wake generator and transonic rotor blade-rows. The MSU-TURBO simulations were run on the 24 wake generator configurations because the majority of DPIV data was also obtained at that configuration. A comparison of the unsteady velocities measured with DPIV with the MSU-TURBO results will serve as an important evaluation of the codes' capabilities, strengths, and weaknesses.

Time-shift boundaries were calculated for 100 time planes. Each blade pass period was split into 180 time steps. The time step must be less

than the time between time planes in the boundary condition. The choices made for these parameters have an impact on the solution accuracy and the computer time necessary to perform the calculation. The SMI simulations used the  $k-\epsilon$  turbulence model.

MSU-TURBO Version 4.1 was designed to run most efficiently on a Cray supercomputer with a Secondary Storage Device (SSD). Two computers at the Naval Oceanographic Office (NAVO) Major Shared Resource Center (MSRC) were used for these simulations. The first was a Cray-T90 with SSD and the second a Cray-SV1. During the course of the research the Cray-T90 was replaced by the Cray-SV1 thus necessitating a change in platforms.

**Solution Convergence.** Convergence was determined by monitoring static surface pressures of each blade-row and the mass flow rate at the exit of the wake generator and entrance to the rotor. The solution was considered converged when the surface pressures were periodic and the difference in mass flows rates between blade-rows was less than 0.5%. Figure 45 shows a history of the first 3600 iterations for the close spacing solution. Pressures are plotted at mid span on the leading and trailing edge suction and pressure surfaces for each blade row. One pressure is also plotted for the mid span, mid chord suction surface. Figure 45 shows that not only is there a difference in mass flow rate at the exit of the wake generator and entrance of the rotor, but the magnitude of the mass flows is decreasing.

Figure 46 shows the last 900 iterations as the close spacing solution reaches convergence. The static pressures are now periodic and the difference in mass flow rates is approximately 0.2%. The magnitude of the mass flow rate is now changing only slightly. It is important to note that the scales on the mass flow plots are different between Figures 45 and 46.

Phase-lag boundary conditions, solving equations in rotating frame of reference, and building the initial solution from an APNASA model reduce

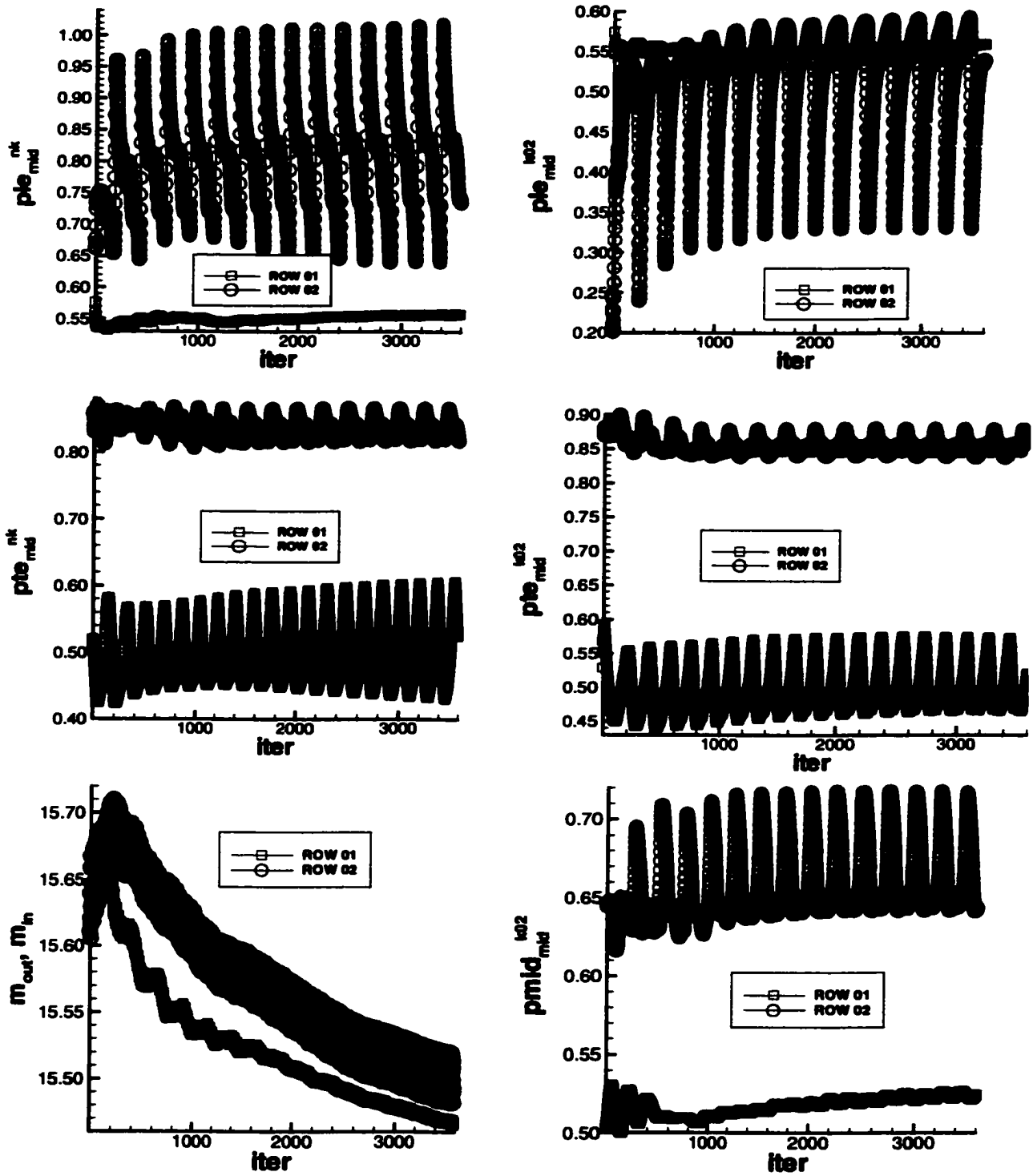


Figure 45. Convergence History of Iterations 1-3600

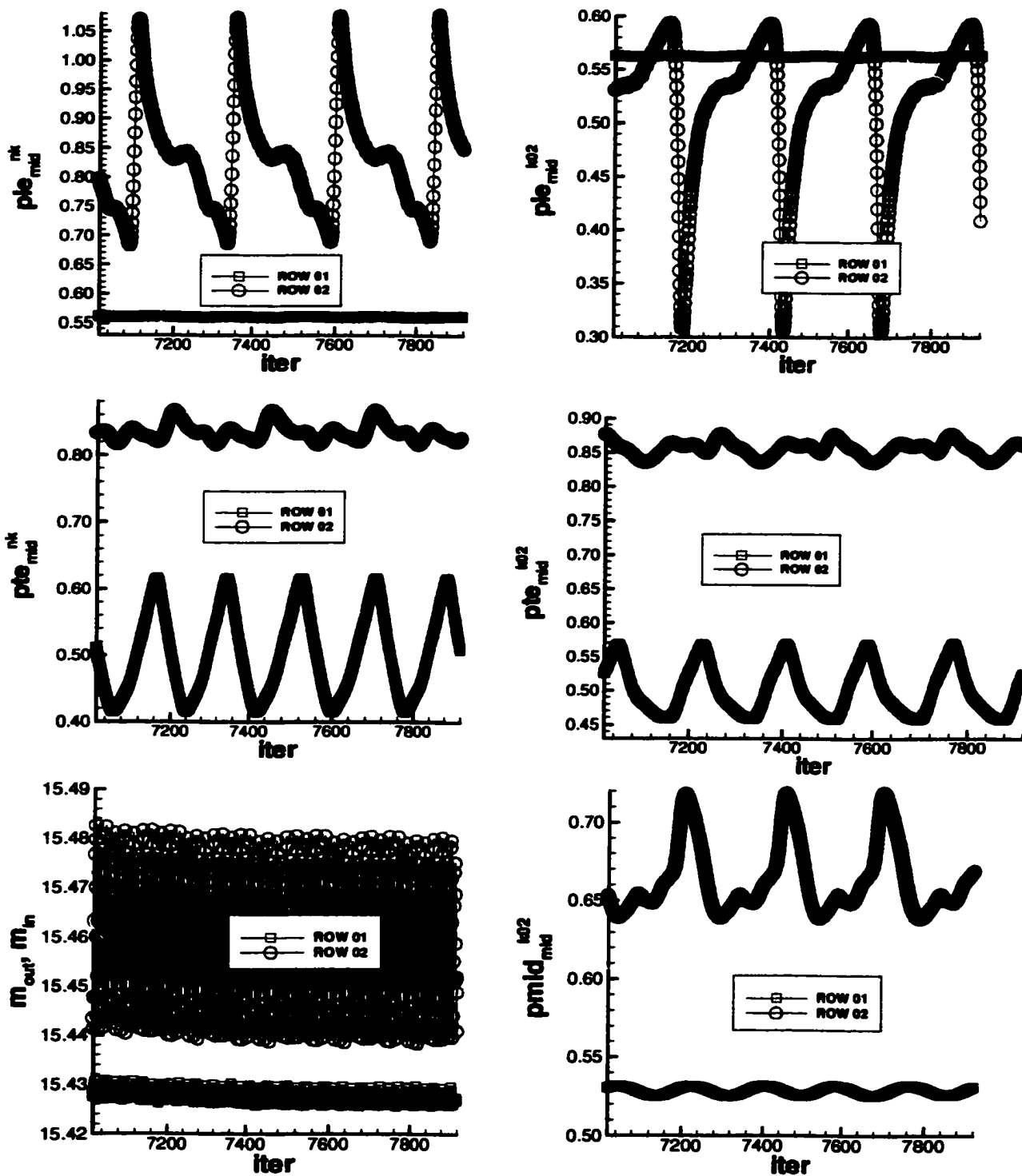


Figure 46. Convergence History of Iterations 7020-7920

the required computational time by several orders of magnitude. The close spacing simulation was run on the Cray-T90 with SSD and required 120 Megawords (Mw) of memory and 86 CPU hours to obtain a converged solution. The far spacing simulation was run on the Cray-SV1 and required 170 Mw of memory and 228 hours of CPU time to reach convergence. The large difference in CPU time is due to the Cray-SV1 not having a SSD as well as the far solution needing 66 blade passes for convergence versus 44 for the close simulation. The far solution also has more nodes in the axial plane, 238 versus 223, which accounts for some increase in computational time required. The far spacing convergence history was similar to the close spacing solution, the only exception being it took more iterations to reach converge.

The output of the MSU-TURBO simulations includes the momentum and total energy  $\rho u$ ,  $\rho v$ ,  $\rho w$ ,  $\rho e$ , and the density and static pressure,  $\rho$  and  $p$ . From these variables all other flow properties were calculated during post-processing of the solutions.

## **NUMERICAL RESULTS**

Analysis of the SMI and rotor-alone experimental data demonstrated that interactions between the wake generator blade-row and the transonic rotor blade-row were most likely responsible for the observed change in performance when the axial spacing between the two blade-rows was varied. Comparison and analysis of the far and close spacing MSU-TURBO simulations make it possible to pinpoint exactly where the increased loss production occurred at close spacing and what unsteady flow mechanism created the loss.

The advantage of a three-dimensional time-accurate Navier-Stokes code is not just the accuracy of the solution, but its ability to present visually the rotation of the rotor and the resulting complex flow fields inherent to transonic compressors. The challenge in analyzing the unsteady CFD results is the large volume of data produced by a simulation. The numerical results were analyzed with a focus on blade-row interaction loss and the flow mechanisms producing the loss. This section will begin by comparing the time-average results of the close and far spacing MSU-TURBO simulations followed by analysis of the time-accurate loss and static pressure results.

### **Time-Average Results**

The time-average results of the close and far spacing MSU-TURBO simulations were compared to show that MSU-TURBO was capable of accounting for the changes in performance observed experimentally. Once a converged simulation was obtained, the time steps from multiple solution files were overlaid on a common grid and averaged. Each solution file consists of the flow field for a specified number of time steps written over one rotor blade pass period. The time-average results presented here are based on 4 solution files, each containing 20 time steps. Ideally it would be desirable to average all 33 blade-passes for one rotor revolution. However,

the change in rotor mass flow rate, inlet and exit total pressure, and efficiency between an average of three rotor blade-passes and four were less than 0.15%. A comparison of the time-averaged MSU-TURBO results with near peak efficiency experimental data is shown in Table 9 for the 24 wake generator far and close spacing configurations.

**Table 9. Comparison of Time-Average MSU-TURBO with Experiment near Peak Efficiency**

	Experiment Close Spacing	Experiment Far Spacing	MSU-TURBO Close Spacing	MSU-TURBO Far Spacing
Mass Flow Rate lbm/s	33.317	33.529	34.111	34.420
Pressure Ratio	1.7378	1.7452	1.8373	1.8388
Efficiency %	82.924	83.814	88.506	89.323

To be consistent, the isentropic efficiency of the MSU-TURBO time-average simulations was calculated in a similar manner as the experimental data using the equation

$$\eta = \frac{H_{2s} - H_{inlet}}{H_2 - H_{inlet}}$$

where  $H = C_p T$ . The value of  $C_p$  was determined from a polynomial equation as a function of the total temperature. The inlet conditions were defined as the reference total temperature and total pressure. At the grid exit  $C_p$  was calculated from the time-average total temperature at each node. The total enthalpies  $H_2$  and  $H_{2s}$  were then calculated and area averaged to determine the overall isentropic efficiency.

It is not surprising that the magnitudes shown in Table 9 are greater for the MSU-TURBO results. To start with the APNASA solutions used as boundary conditions were biased higher than the experimental results. For example, at close spacing the APNASA model of all three blade rows showed an increase of approximately 2% in choking mass flow rate, 7 % in pressure ratio, and 4.3 points in efficiency. The MSU-TURBO simulations were only run on the first two blade rows to reduce computational time while the experimental results of Table 9 are for the three-blade-row SMI configuration. Thus the losses that would be present from the downstream stator are not included in the overall numerical performance results. Another contributing factor may be because the MSU-TURBO grid did not extend very far downstream of the rotor trailing edge, once again to reduce computation time. If the grid were extended further downstream the exit flow would continue to mix out most likely resulting in lower efficiency and pressure ratio.

The purpose of Table 9 is to show that MSU-TURBO was able to capture the change in efficiency between far and close spacing. The magnitude of the efficiency is not as important as the change in efficiency between the two spacings. The change in experimental efficiency for the data point presented in Table 9 was observed to be 0.890 points. The MSU-TURBO simulations had a difference of 0.817 points in efficiency that suggests the numerical model was able to account for changes in performance between far and close spacing to a level very close to that observed experimentally. The difference in pressure ratio between the far and close spacing experimental data was less than the repeatability (0.008) of the measurement. Similarly, the MSU-TURBO simulations showed very little change in pressure ratio (0.0015). Since the operating point of the two spacings are at different flow coefficients for the same exit condition, it is possible to have very little change in pressure ratio even though the pressure rise characteristic is higher for far spacing. Another words, if data

were acquired at a consistent mass flow rate, the far spacing pressure ratio would be greater than the close spacing. The mass flow rate for the experiment increased by 0.64% from close to far spacing for the experiment while numerically it increased by 0.91%. The best comparison between the experiment and MSU-TURBO would be based on the choking mass flow rate, however, a numerical model at this operating condition was not performed.

**Time-Average Loss Comparison.** To check if the change in efficiency between the close and far spacing simulations was a result of blade row interactions the time-average loss at the entrance to the rotor blade-row was compared. Denton suggested in reference [24] that the most informative measure of loss is entropy production. For the loss analyses presented in this section the entropy flux per unit area normalized by  $C_p$  ( $\rho u \Delta s / C_p$ ) was chosen. This term will hereafter be used synonymously with loss. The change in entropy between two states is defined as

$$\Delta s = \ln\left(\frac{T}{T_{ref}}\right) - R \ln\left(\frac{P}{P_{ref}}\right)$$

Using the time-average solution, the loss was calculated at each node and then averaged to obtain a single value for the close and far spacing simulations. Taken from the exit of the wake generator grid the close spacing loss was 12.34% greater than far spacing. If measured from the rotor grid at the rotor leading edge the close spacing loss was 22.49% greater than far spacing. The reason for the difference in measured loss between the two locations will be discussed when the time-accurate numerical results are presented. The time-average loss was also calculated at the exit of the rotor grid. At that position the close spacing loss was 9.01% greater than far spacing. This confirms that indeed an unsteady loss producing mechanism exists for close spacing that is not found at far spacing. Increased loss exists because the blade-row spacing was reduced.

This also demonstrates that the change in efficiency between MSU-TURBO simulations was not a numerical artifact of the solution algorithm.

### **Time-Accurate Results**

The simulations were set up to output the flowfield at twenty time-steps as the rotor blade moved one blade pass. Figures in this section contain a few time-steps while movies of the complete simulation are found on a compact disk in Appendix C.

A comparison of the close and far spacing simulation at time-step 5 is shown in Figure 47. The figures are contour plots of loss at 75% span. Plotting the loss highlights features such as shed vortices from the wake generator trailing edge, wake chopping and transport of the wake through the rotor, rotor bow shock, rotor passage shock, and boundary layers on the rotor blade surface. These features are seen on both the close and far spacing solutions. When the transonic rotor is spaced farther from the wake generator, more shed vortices are visible and the wake widens as it migrates downstream before reaching the rotor.

It was noticed on both simulations that the wake appears to expand as it passed through the sliding interface between the blade-row meshes. This has been observed in other cases with MSU-TURBO and is a general feature of unsteady periodic or phase-lag boundary simulations using a sliding interface between meshes. It is felt that the expansion of the wake through the present interface would have at most a secondary effect on the observations made upstream at the wake generator trailing edge. It is because of this interface issue that the time-average loss presented previously is different when measured at the exit of the wake generator grid versus the rotor leading edge. At far spacing the wake has mixed out more before entering the rotor and is wider. As the wake passes through the sliding interface in the far spacing simulation it does not expand as much through the interface as it did with the close spacing simulation.

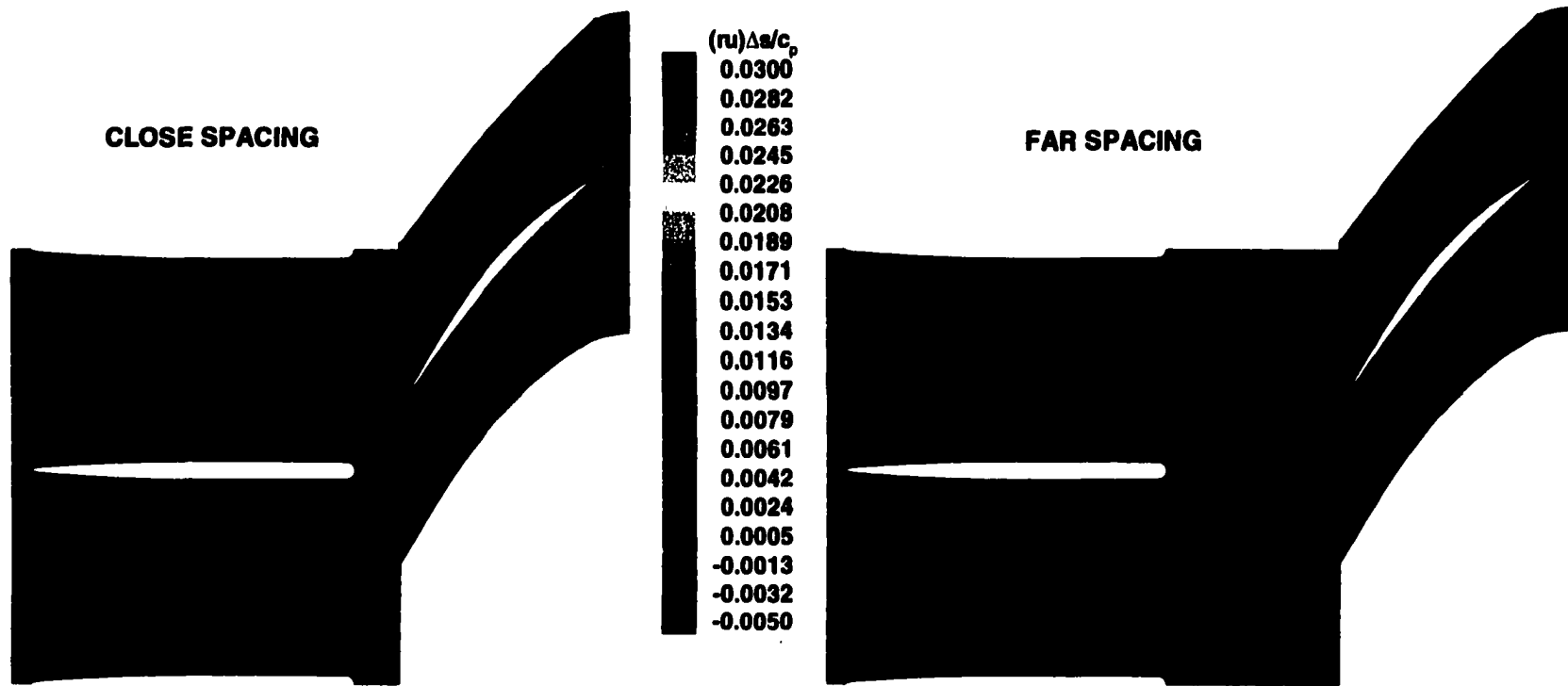


Figure 47. MSU-TURBO Flow Field Loss Comparison, 75% Span, Time-step 5

The biggest difference between the close and far spacing contour plots presented in Figure 47 is a region of loss found in the close spacing flow field not found in the far spacing flow field. This region is located near the trailing edge of the wake generator on the upper blade surface.

**Close spacing loss.** All twenty time-steps from the solution at 75% span have been combined to form a movie named 24wg\_close\_loss.avi found in Appendix C. Flow fields at six equally spaced time steps from the simulation are shown in Figure 48. The legend for Figures 48 and all subsequent loss contour plots is the same as that presented in Figure 47. From the close spacing loss movie important insights are gained by analyzing the losses between the wake generator trailing edge and the rotor leading edge. During time-steps 1-3 a loss associated with the rotor bow shock is observed upstream of the middle rotor blade. This loss region covers about 50% wake generator pitch and extends upstream to the axial plane of the wake generator trailing edge. A similar loss region is evident from the lower rotor bow shock but the loss extends up to the lower surface of the wake generator trailing edge. Examination of the wake generator trailing edge upper surface shows a region of additional loss. This loss region has a peak located near 95% wake generator chord and extends into the flowpath 14 to 16% wake generator pitch for all time-steps. Loss from this peak convects downstream above the wake generator wake. From time-steps 4-7 the loss peak moves forward on the wake generator upper surface and the loss downstream of the peak and above the wake thickens. At time-step 5 the peak is centered at 92% wake generator chord. As the rotor blade-row continues to rotate the bow shock loss from the lower rotor blade moves also and no longer intersects the lower blade surface of the wake generator. There is little change in the bow shock loss upstream of the middle rotor blade and by time-step 7 the bow shock loss of the middle and lower rotor blades are similar in shape.

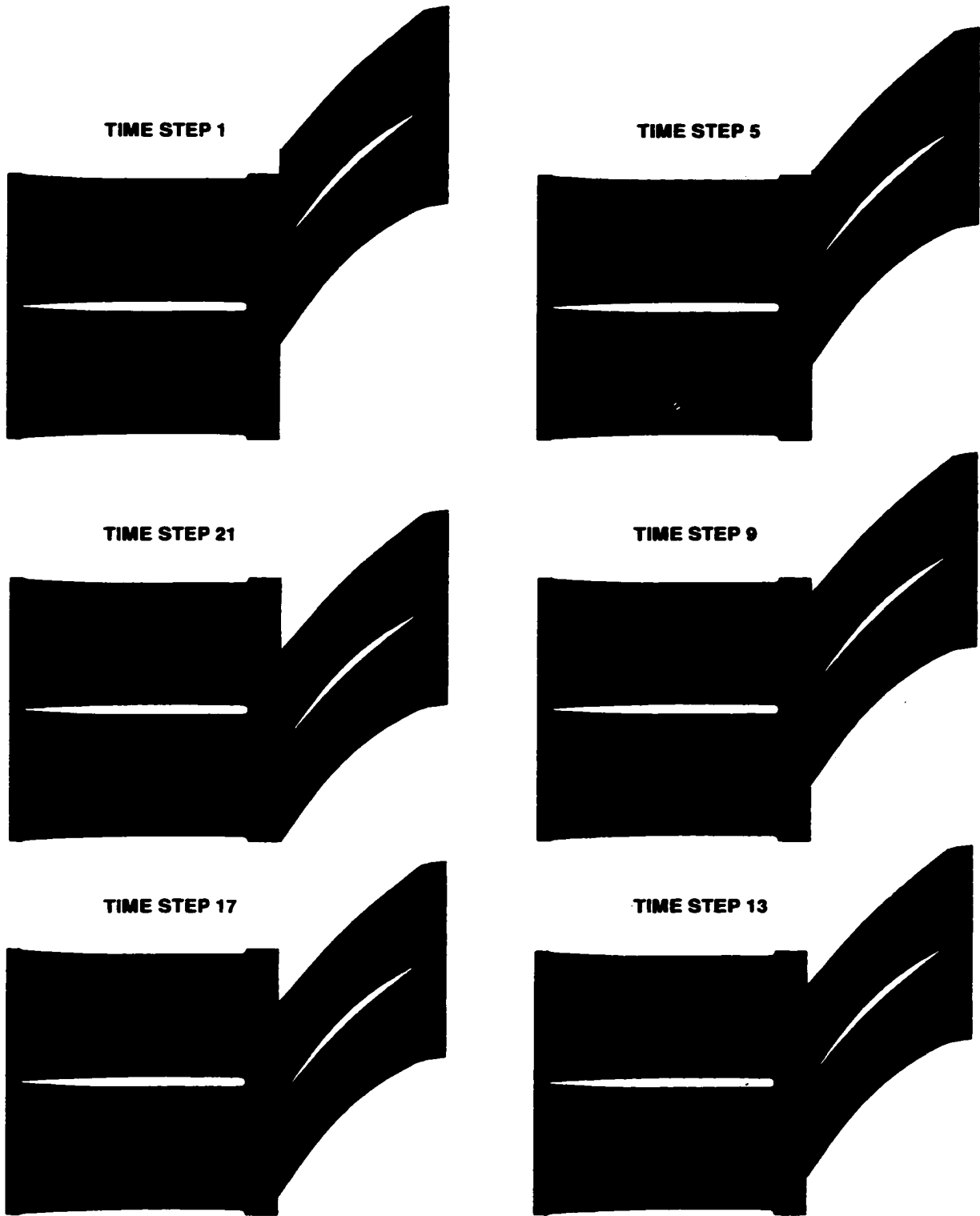


Figure 48. MSU-TURBO Close Spacing Loss Contours, 75% Span

Between time-steps 8-10 the loss region on the wake generator upper surface continues to propagate forward and thicken. By time-step 9 the peak has reached 88% wake generator chord. At time-steps 8-10 the loss region on the wake generator upper surface has formed two peaks. The bow shock loss region of the middle rotor blade changes shape and forms two distinct branches. From time-steps 11-13 the wake generator wake and convected loss from the wake generator upper surface interacts with the bow shock branches. The bow shock loss covers less area upstream of the rotor in the pitchwise direction. The loss peak on the wake generator upper surface is now nearly stationary. Between time-steps 10-12 the forward peak on the wake generator upper surface disappears leaving only one peak at 93% wake generator chord. From time-steps 13-16 the rotor chops the wake generator wake. The bow shock loss of the lower rotor splits into two branches as was observed previously for the middle rotor at time steps 8-10. Between the wake generator upper surface and the rotor leading edge the two waves interact with the loss convected downstream from the loss peak of the wake generator upper surface. At time step 14 a wave pattern is evident with three peaks between the wake generator trailing edge to the rotor leading edge. By time-step 16 there is one peak on the wake generator upper surface and one just downstream of the wake generator trailing edge. On the wake generator upper surface the single peak is present but the convected loss region is only present downstream of the second peak. The first peak is associated with the lower rotor blade and the second is associated with the middle rotor blade.

For time-steps 17-20 the upstream peak produced from the lower rotor blade is centered about 91% wake generator chord and disappears by time-step 20. The loss peak from the middle rotor propagates forward and interacts with the wake generator trailing edge. Time-step 21 is the same flow field as time-step 1 with the rotor blade at a different position. The

process then repeats itself. The magnitude of the loss changes very little over time. It is the shape and area covered by the loss region that changes.

**Far spacing loss.** For comparison the same six time steps for the far spacing simulation movie are shown in Figure 49. Review of the movie 24wg\_far\_movie.avi shows that the losses associated with the rotor bow shock do not interact with the upstream wake generator at all and consequently there is no loss region on the wake generator trailing edge upper surface nor above the wake boundary. At time-steps 1-2 the loss from the lower rotor bow shock extends to the wake lower boundary. By time-step 3 this bow shock loss no longer reaches the wake generator wake. Similarities to the 24wg\_close\_movie.avi are seen between time-steps 6-10. At these times the bow shock loss changes from one large area to two small branches. However the branches are not as long as those observed at close spacing. At time-steps 11-13 two peaks are seen interacting with the wake upper surface. The peaks are smaller than those observed at close spacing and they don't propagate upstream very far. The wake is chopped by the rotor between time steps 12-16. Similar to close spacing the loss magnitude of the bow shock is nearly constant.

**Static Pressure Contours.** Having established that the close spacing configuration produced additional loss on the upper surface of the wake generator trailing edge not found at far spacing, the numerical model was used to decipher what fluid dynamic process produced the loss. Shock-boundary layer interaction has been shown [30] to produce boundary layer separation that results in higher loss. Axial velocity profiles along the wake generator upper surface showed no such phenomena. Static pressure contours have proven helpful in understanding the fluid dynamics of blade-row interactions. Figure 50 compares static pressure contours at 75% span for both close and far spacing simulations at time-step 5. Pressure waves such as the bow shock and passage shock across which flow properties change rapidly are characterized by tightly packed contour lines.

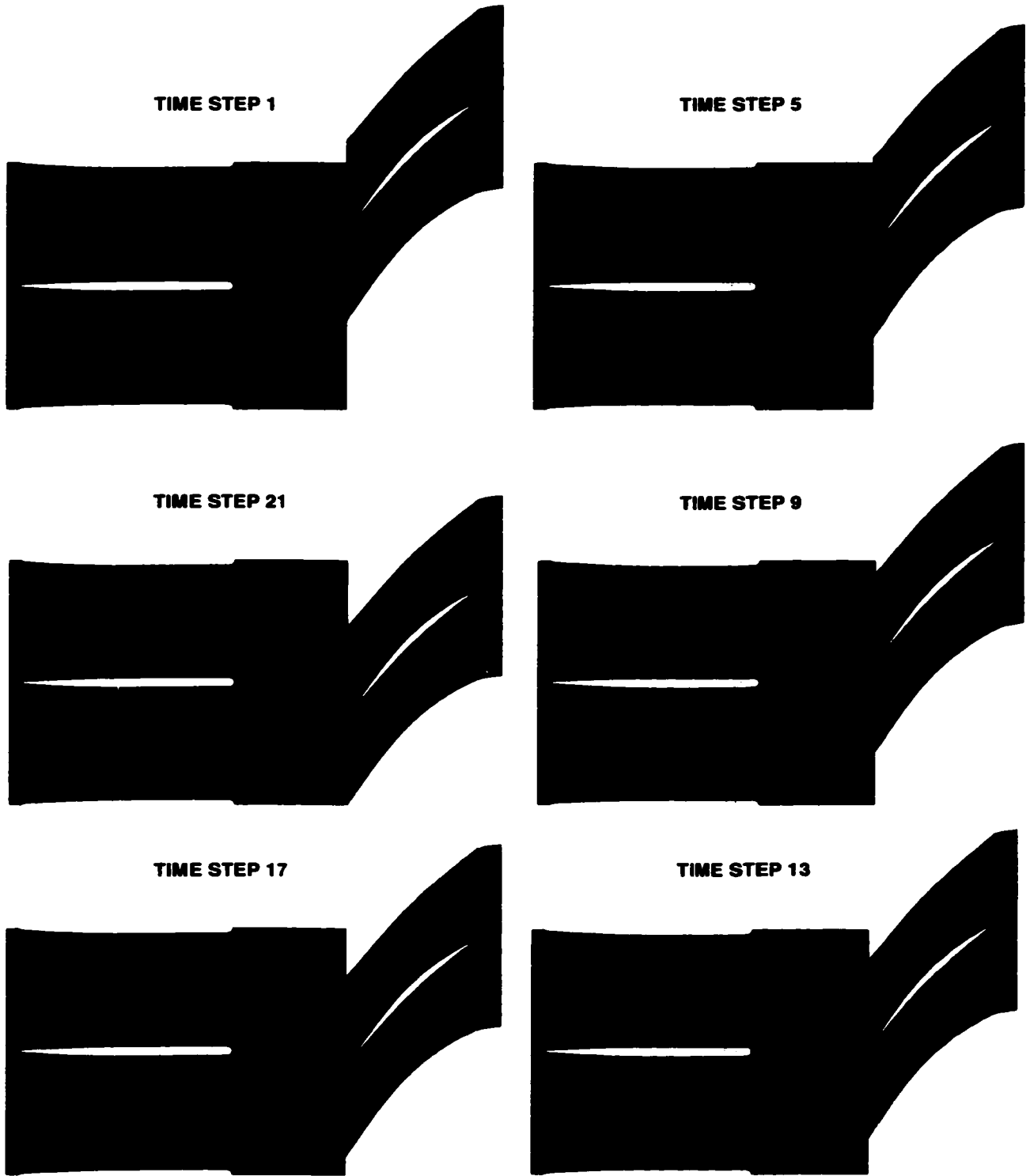


Figure 49. MSU-TURBO Far Spacing Loss Contours, 75% Span

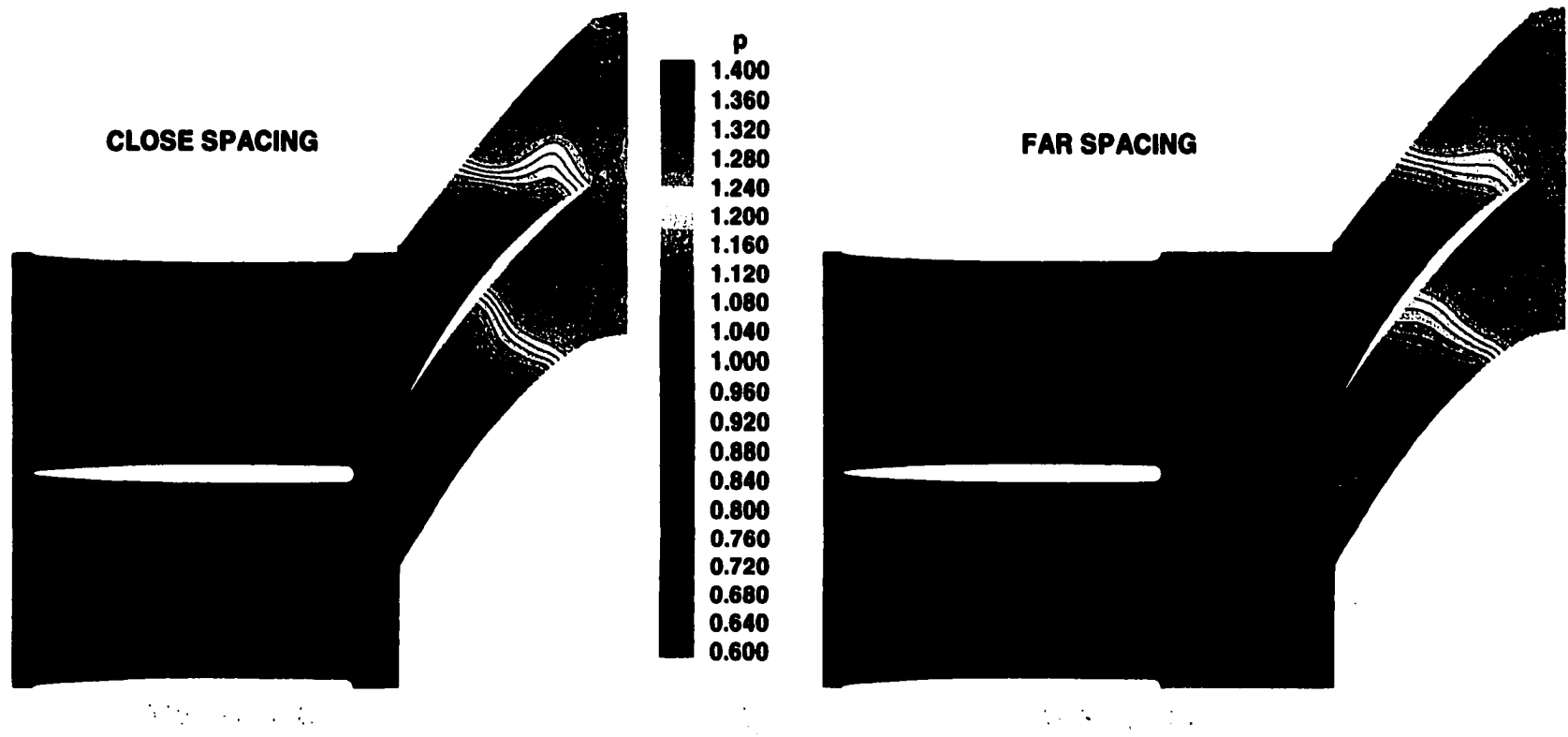


Figure 50. MSU-TURBO Static Pressure Comparison, 75% Span, Time-step 5

A shock wave varies in strength from strong to weak depending on the flow properties upstream and downstream of the shock and the orientation of the shock wave to the flow. The passage shock for both spacings shown in Figure 50 is considered strong as the static pressure increases greatly in a small distance. The flow across the shock goes from subsonic to supersonic. The passage shock is oriented slightly oblique to the rotor blade-to-blade flow.

The bow shock is oblique and detached from the rotor leading edge. Figure 50 shows the bow shock is strongest near the rotor leading edge and extends into the wake generator flow field. The farther away from the rotor leading edge the weaker the shock becomes. Except for very near the rotor leading edge the Mach number across the bow shock remains supersonic. The changing strength of the bow shock is visible in Figure 50 as the pressure contours are very close together near the rotor leading edge but are fewer and farther apart as the bow shock approaches the lower surface of the wake generator. The passage shock is similar for close and far spacing as is the bow shock near the rotor leading edge. However, at far spacing the bow shock dissipates quicker than at close spacing. Thus, closer spacing appears to affect the strength of the bow shock away from the rotor leading edge. At close spacing it is the stronger portion of the bow shock wave that interacts with the wake generator trailing edge. What little interaction takes place between the bow shock and the wake generator at far spacing takes place on the weak part of the bow shock wave.

From Figure 50 it is observed that the upper surface of the wake generator trailing edge has islands defined by numerous contour lines. There is a low pressure region followed by a pressure wave related to the rotor bow shock, followed by another low pressure region. These three zones will be defined as the leading low pressure region, the wake generator pressure wave, and the trailing low pressure region. These regions vary in strength during the simulation. For future reference weakening and

strengthening of these islands simply means the pressure magnitude changes and more contours lines are visible. The pressure magnitude and the density of the contour lines are directly related. The magnitude of the static pressure and the density of the contour lines define the wave strength. These zones are analyzed in the movie 24wg\_close\_p\_movie.avi. Six time-steps from the simulation are presented in Figure 51.

At time-step 1 a low pressure island is centered on the wake generator upper surface at 92% wake generator chord and extends into the flow about 25% wake generator pitch. This is the leading low pressure region. At 96% chord a very high gradient region is found where the bow shock from the lower rotor blade has been chopped by the wake generator trailing edge. This is similar to what happens when a rotor blade chops a wake. The remnants of the bow shock wave, hereafter referred to as the wake generator pressure wave, also extend into the wake generator pitch about 25%. This is the amount the bow shock extended into the wake generator pitch at the time it was chopped by the wake generator. From time-steps 1-14 the leading low pressure region moves forward and loses strength. As it loses strength its pressure increases to that of the upstream flow. As the magnitude changes so does the density of the contour lines. By time-step 14 the leading low pressure region has moved forward to 77% chord and by time-step 20 it is no longer visible.

From time-steps 1-5 the wake generator pressure wave moves forward to 95% wake generator chord. Recall that the bow shock wave was chopped to form the wake generator pressure wave. Similar to the bow shock the static pressure increases across the pressure wave. As the oblique bow shock is chopped by the wake generator trailing edge the resulting wake generator pressure wave is oriented normal to the wake generator surface. As the wave moves forward the high pressure is still evident but the gradients between the wave and the upstream low pressure region are not as large. The pressure wave is oriented nearly normal to the wake generator

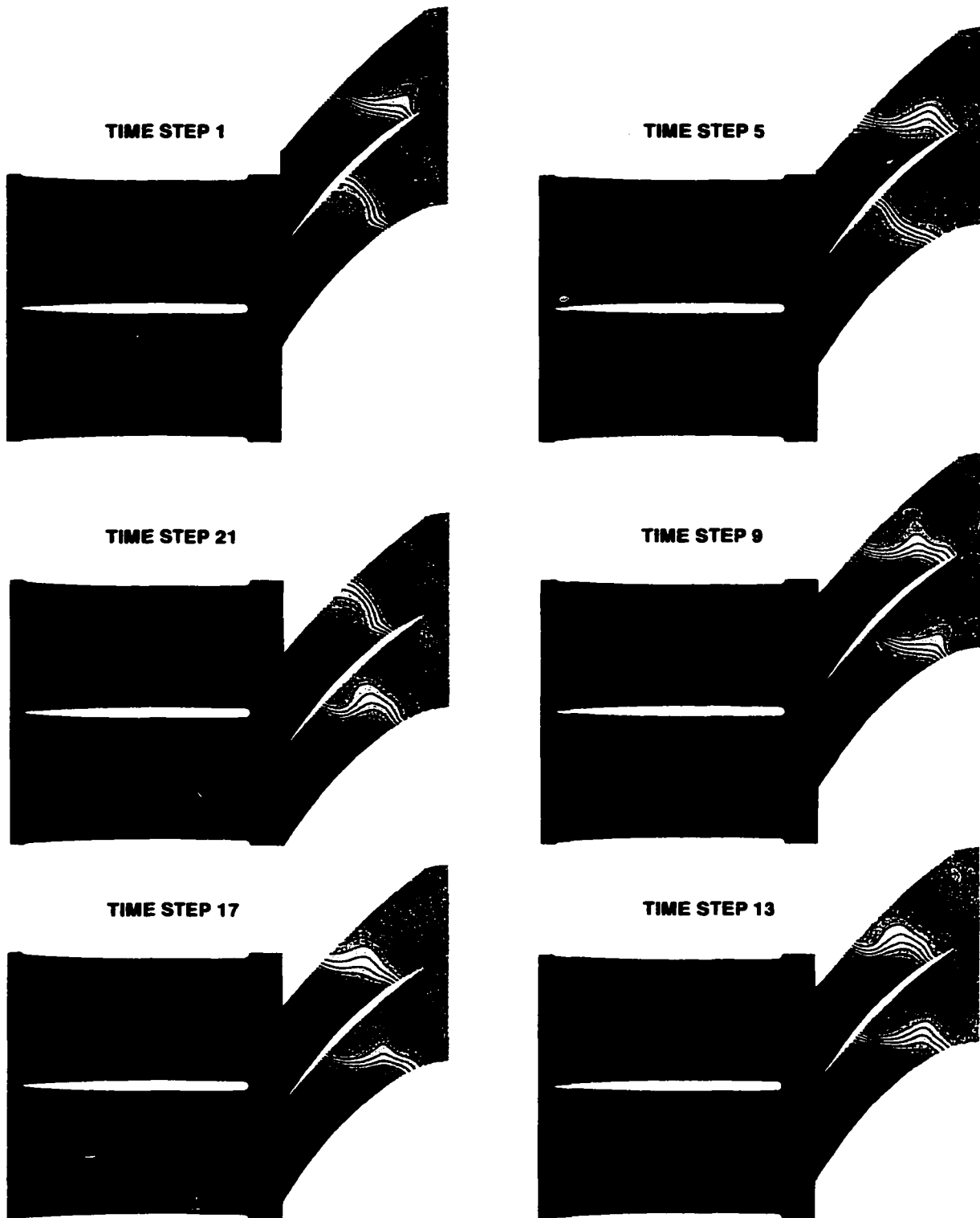


Figure 51. MSU-TURBO Close Spacing Static Pressure Contours, 75% Span .

surface and extends to 22% of the wake generator pitch. At time-step 4 a new low pressure region fills in behind the wave. This is the trailing low pressure region. From time-steps 4-13 the trailing low pressure region curls around the wake generator trailing edge while decreasing in magnitude. At time-step 9 the trailing low pressure region is at 98% chord and the wake generator pressure wave is centered at 92% wake generator chord. Between time-steps 5-9 this wave loses strength. By time-step 13 the wake generator pressure wave is at 87% chord. The trailing low pressure region is at 97% chord. The wake generator pressure wave moves with the rotor bow shock but is normal to the wake generator blade surface. The pressure wave continues to weaken as it propagates forward. Between time-steps 6-13 a low pressure region also forms on the lower surface of the wake generator trailing edge.

During time-steps 13-17 the wake generator pressure wave continues to move forward and weaken. By time-step 17 this wave has propagated upstream to 83% chord. The trailing low pressure region on both surfaces of the trailing edge doesn't move forward but is nearly stationary. At time-step 17 the trailing low pressure region is centered at 96% chord. The bow shock from the next rotor blade now approaches the wake generator trailing edge and begins to interact with the trailing low pressure region. The trailing low pressure regions on both surfaces react to the interaction by tilting in the upstream direction. During time-steps 18-21 the bow shock is chopped by the wake generator trailing edge. The new pressure wave from the bow shock begins to push the trailing low pressure region upstream. The cycle then repeats itself with the trailing low pressure region becoming a new leading low pressure region and a new wake generator pressure wave forming on the wake generator upper surface.

**Far spacing static pressure.** The static pressure results of the far spacing simulation at 75% span are found in Appendix C in the file 24wg\_far\_p\_movie.avi. Six time-steps from the simulation are presented in

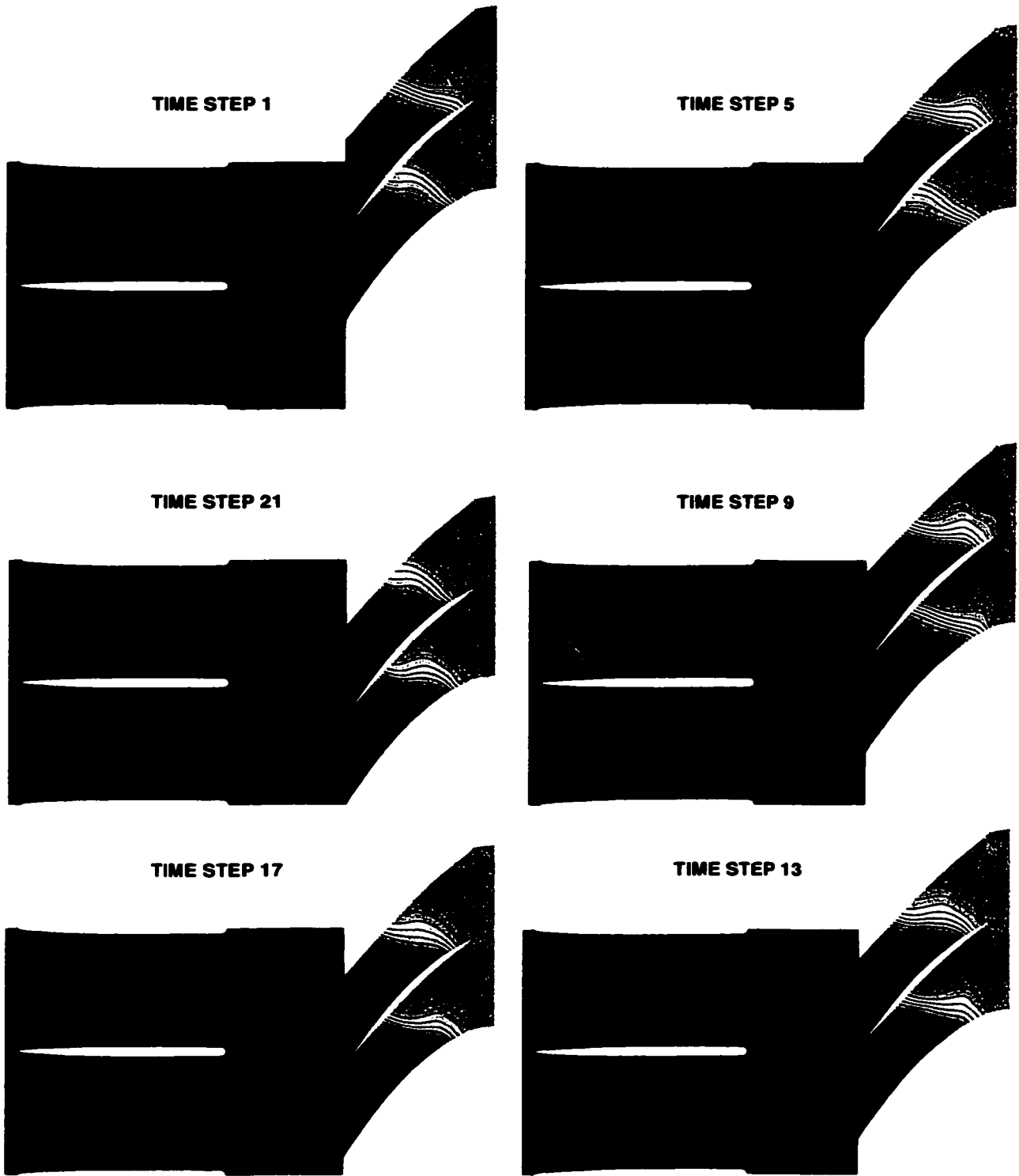


Figure 52. MSU-TURBO Far Spacing Static Pressure Contours, 75% Span

Figure 52. It is immediately apparent that due to the larger axial gap between blade-rows only a weak remnant of the rotor bow shock interacts with the wake generator trailing edge, hereafter referred to as a bow wave. At no time does a pressure wave form on the upper surface of the wake generator. At time-step 1 a bow wave exists in both of the wake generator passages. From time-steps 1-11 the bow wave extending to the upper passage sweeps past the wake generator trailing edge. As the wave makes contact with the wake generator it no longer protrudes into the passage. By time-step 11 the bow wave that existed in the upper wake generator passage has vanished. Between time-steps 12-21 the next bow wave proceeds to move toward and enter the upper wake generator passage.

At time-step 1 there are three low pressure regions on the wake generator blade surface. Two are located on the upper surface of the blade. A small low pressure region is located at 78% wake generator chord. This forward low pressure region disappears by time-step 5. The other two regions are found on each surface of the wake generator, extending from the trailing edge upstream to 97% chord.

From time-steps 1-4 the low pressure regions at the wake generator trailing edge strengthen and grow in size, eventually peaking at time-step 4. Between time-step 5-11 these low pressure regions grow in the chordwise direction while weakening. As the low pressure regions move forward they tilt in the upstream direction from their original orientation. Between time-steps 12-21 the low pressure regions become stronger. The formation of the low pressure regions coincides with the bow shock wave passing the wake generator trailing edge.

### **Close and Far Spacing Comparison**

In summary, the MSU-TURBO simulations demonstrate that important differences exist between the close and far spacing flow fields that explain the difference in measured overall performance when blade-row spacing varies. Figures 47-49 highlight that the blade-row interactions at

close spacing produce increased loss on the wake generator trailing edge upper surface. The lower efficiency, pressure ratio, and mass flow rate measured in the close spacing configuration compared to the far spacing configuration is a result of this extra loss.

Figures 51 show that at close spacing the rotor bow shock is actually chopped by the wake generator trailing edge. The shock diffracts around the blunt trailing edge forming a pressure wave on the upper surface of the wake generator that propagates upstream until it weakens. Below the wake generator the bow shock follows the rotor blade and thus no pressure wave is formed on the lower surface. The bow shock is oblique as it interacts with the wake generator trailing edge, but the resulting wake generator pressure wave that forms is oriented normal to the wake generator blade surface.

At far spacing the rotor bow shock has degenerated into a pressure wave when it interacts with the wake generator. This weaker wave is not chopped by the wake generator and therefore no pressure wave forms on the wake generator upper surface. In this case the wake generator blocks the bow shock at the lower surface of the wake generator and it disappears.

A common feature observed in both the close and far spacing simulations is the formation of a low pressure region after the bow shock is chopped. For close spacing and to some extent far, the low pressure regions are stationary until driven upstream by the bow shock or wake generator pressure wave. At far spacing the low pressure regions formed are not as strong as those observed at close spacing. The low pressure regions are driven forward by wake generator pressure wave on the upper surface of the rotor bow shock on the lower surface. The low pressure regions exist in both the close and far spacing simulations and are therefore not a product of reduced blade-row spacing. They are simply the result of the flow accelerating downstream of the rotor bow shock. This expansion zone in the flow was also observed by Ottavy et al [12, 13].

With time-accurate simulations there is almost an unlimited amount of data available for analysis. Although much may be learned about the flow physics of blade-row interaction through a more in-depth analysis, the results presented here were limited to the scope of the research effort which was to concentrate on explaining the loss produced at close spacing.

### **Numerical Model Improvements**

The MSU-TURBO simulations do a very good job of showing where the additional loss is produced at close spacing and in describing the fluid dynamics of the blade-row interaction. As with any CFD model improvements can be made with finer meshes. A finer mesh would better resolve the bow shock, passage shock, and pressure wave. The width of the shocks and pressure wave would be narrower with a finer mesh. Although a finer mesh is more accurate it is also more susceptible to numerical instability. The general observations about loss production would not change but a finer grid would be beneficial for analyzing details of the flow kinematics and comparing with DPIV results.

The consequences of the sliding interface were examined previously in this section. The effects of the sliding interface can be reduced through grid refinement. Van Zante [29] has suggested adding more cells tangentially in the rotor grid and unpacking the mesh so there is equal spacing at the interface.

## **BLADE-ROW INTERACTION LOSS PRODUCTION**

In this section a mechanism for loss production is proposed based on the numerical results. It is validated with unsteady static pressure measurements made on the wake generator blade surfaces. The spanwise extent of the blade-row interaction loss at close spacings is also investigated. Finally, the implications of blade-row interaction loss on compressor designed is discussed followed by suggestions for future research.

### **Relationship Between Loss and Wake Generator Pressure Wave**

Reviewing the loss and static pressure results for close spacing (Figures 48 and 51) it is observed that the wake generator pressure wave is directly related to the production of loss on the wake generator upper surface. The loss peaks on the blade surface coincide with the location of the wake generator pressure wave in time. As the pressure wave propagates forward so does the loss. When the pressure wave weakens due to viscous effects the loss disappears. The multiple loss peaks observed at time-step 13 of Figure 48 are due to a pressure wave chopped from the lower rotor blade bow shock and the bow shock from the middle rotor blade. At time-step 17 the forward peak is from the pressure wave produced when the lower rotor bow shock was chopped and the peak near the wake generator trailing edge is from the incoming bow shock being chopped to form a new wake generator pressure wave. By time-step 21 the forward pressure wave has weakened sufficiently such that it no longer produces loss.

There exists a pressure wave traveling along the wake generator upper surface that produces loss as it moves upstream until it reaches 91% chord. It is proposed that in the reference frame relative to the wake generator pressure wave, the flow is supersonic and a moving shock wave normal to the freestream flow is formed that produces loss.

### Wake Generator Unsteady Static Pressure Measurements

To validate this theory, unsteady static pressure measurements made with Kulite high-response transducers were analyzed and compared with the MSU-TURBO results. Details of the static pressure measurements were reported by Koch et al [31]. Figure 53 from reference [31] shows the location of the Kulites on the wake generator. Two wake generators were instrumented, one on the upper surface and the other on the lower surface. The transducers were located at 50% and 75% wake generator span at 95%, 89%, 83%, 70%, and 50% wake generator chord.

Figures 54-55 compare the experimental Kulite measurements with MSU-TURBO static pressures predicted from the close spacing simulation at 75% span. Two blade passes are plotted in each figure. In order to directly compare both data sets the numerical results from the 95% chord node were shifted in time until its peak lined up with the peak from the experimental data. The data from the remaining locations were then shifted in time the same amount. This allowed the phase as well as the frequency and magnitude of the data sets to be compared.

The peak-to-peak pressure measured by the Kulites was greater than that predicted by MSU-TURBO. One of the reasons the MSU-TURBO static pressures are lower than the Kulite measurements is because the mass flow rate of the simulations was greater than the mass flow rate of the SMI rig at

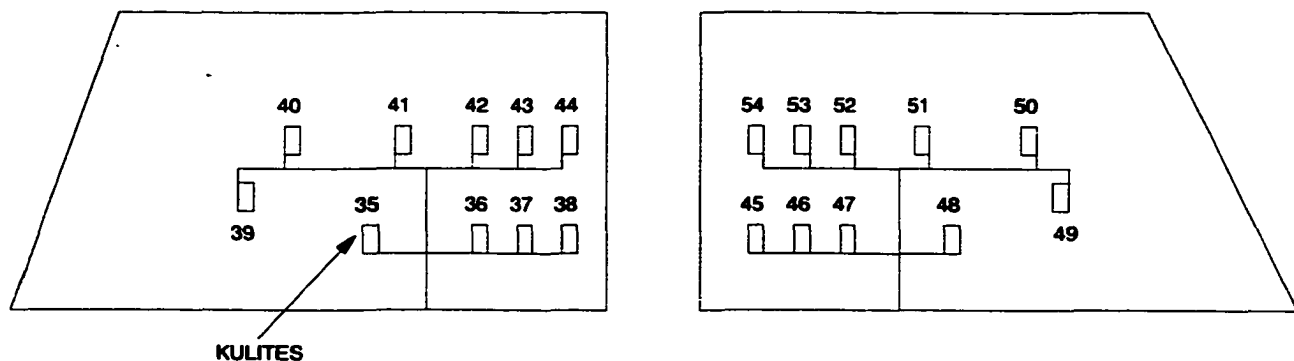


Figure 53. Wake Generator Kulite Measurement Locations

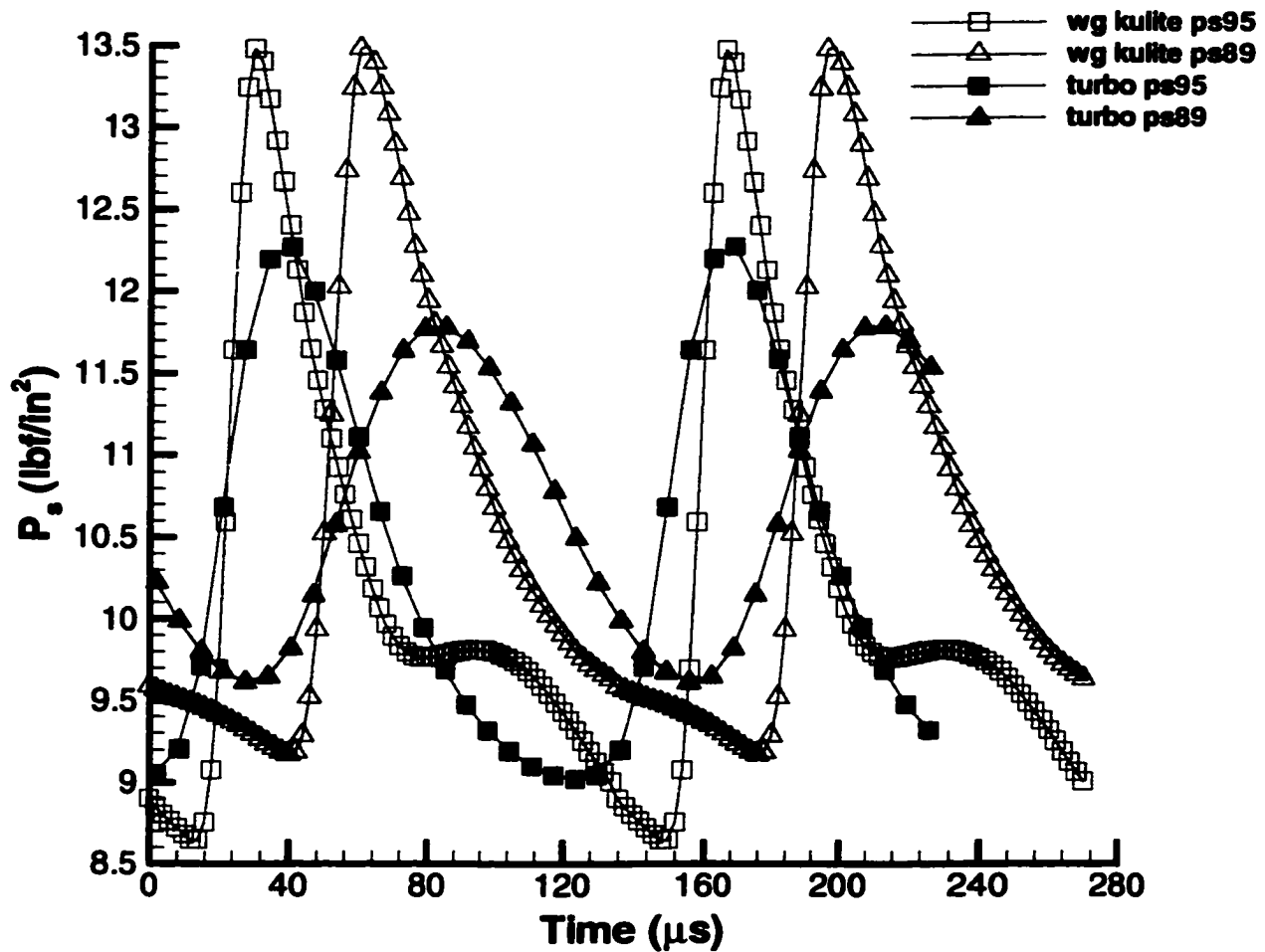


Figure 54. Static Pressure Comparison at 95% and 89% Chord

a similar operating point. Higher velocities through the wake generator result in lower static pressures. The numerical results show a reduction in the peak-to-peak magnitude as the wave travels upstream. However, the experimental data suggest the weakening of the pressure wave is not so drastic as the wave does not begin to weaken until it has reached 70% chord. As expected the pressure wave measured by the Kulites is sharper than that predicted by MSU-TURBO. A finer grid would produce a narrower wave. The experimental results and the 95% chord computation data show the upstream side of the pressure wave is steeper than the downstream side. As the wave moves upstream it dissipates and widens.

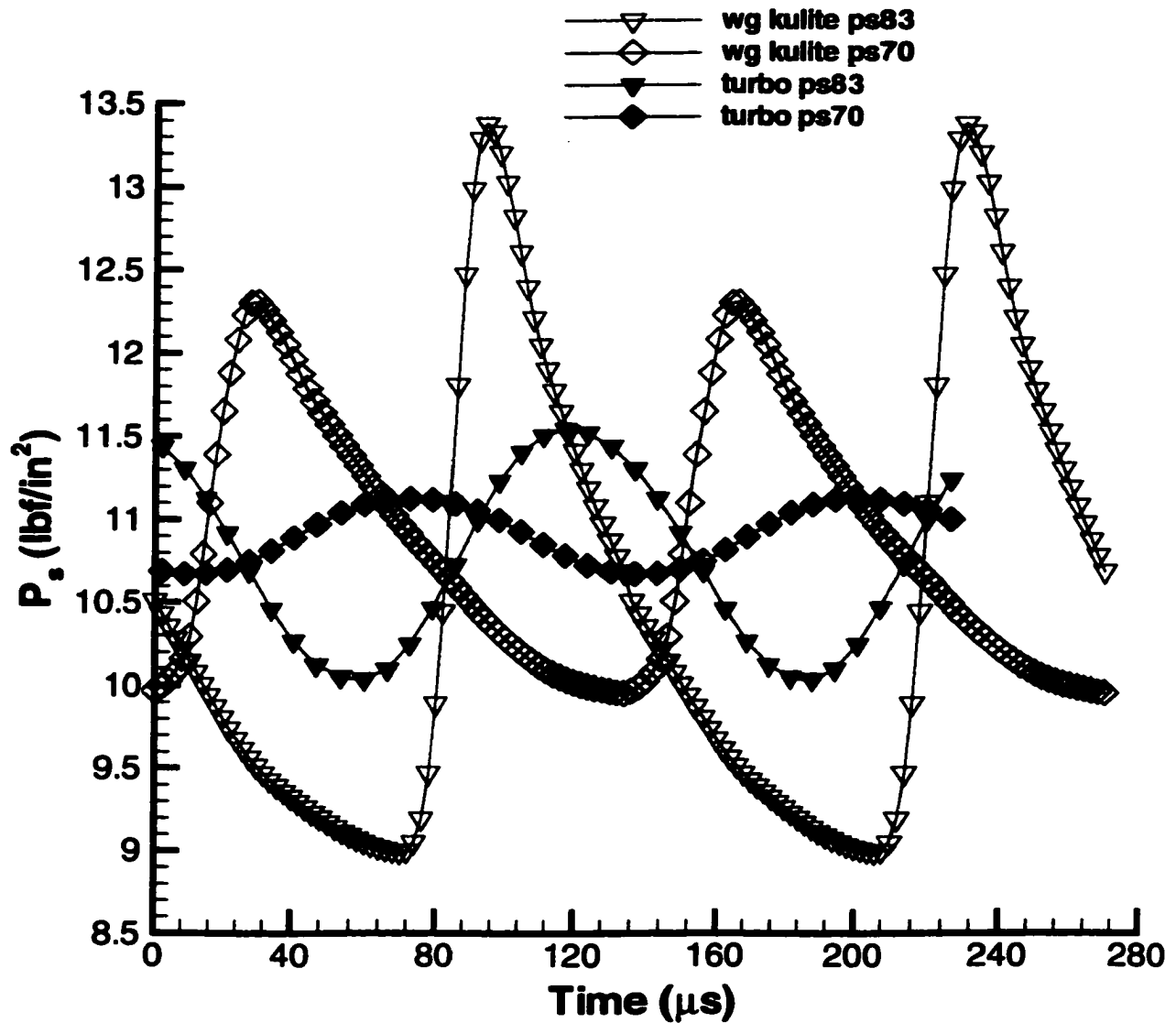


Figure 55. Static Pressure Comparison at 83% and 70% Chord

The frequency of the pressure signals changes little as the wave propagates upstream. The experimental average was 7.355 kHz and the MSU-TURBO was 7.794 kHz. The small difference is most likely a result of the SMI rig not rotating at exactly 100% design speed during the experiment. At 95% chord the numerical results are nearly in phase with the Kulite measurements. At 89% chord the computation begins to lag the experiment and the phase lag increases further at 83% and 70% chord.

The propagation velocity of the wake generator pressure wave,  $V_{\text{wave}}$ , was determined from the time it took the wave to travel the distance between two static pressure measurements. The Mach number of the pressure wave in its relative frame is defined as

$$M_{\text{wave}} = \frac{V_{\text{wave}} + V_{\infty}}{a_{\infty}}$$

The velocity and speed of sound of the flow into which the pressure wave propagates are  $V_{\infty}$  and  $a_{\infty} = \sqrt{\gamma R t_{\infty}}$ . The static temperature upstream of the wave is determined from

$$t_{\infty} = T_{\infty} - \frac{V_{\infty}^2}{2C_p}$$

Using data from the experimental tests,  $V_{\infty}$  was determined from the 6.44% span pressure measurements described in the Wake Calibration section of this report. The specific heat at constant pressure and total temperature ( $C_p$ ,  $T_{\infty}$ ) was obtained from conditions at the SMI rig inlet (see Figure 5). With  $V_{\text{wave}}$  determined between 95% and 89% wake generator chord  $M_{\text{wave}}$  was calculated as 1.113. Using the same values for  $V_{\infty}$ ,  $C_p$ , and  $T_{\infty}$ , but calculating  $V_{\text{wave}}$  between 89% and 83% wake generator chord  $M_{\text{wave}}$  was slightly lower at 1.093.

Based on the computational results at time-step 3 the wake generator pressure wave Mach number was 1.181. Comparing the experimental and numerical data used to determine  $M_{\text{wave}}$  two important observations were made. The propagation velocity of the wave,  $V_{\text{wave}}$ , was lower for the MSU-TURBO simulation and the low pressure region immediately upstream of the wave resulted in higher  $V_{\infty}$  and lower  $a_{\infty}$ . For the experimental calculation the conditions upstream of the wave were estimated from measurements made downstream of the wake generator during the wake calibration phase of the research program and thus would not account for any local changes in the flowfield due to neighboring blade-rows.

These calculations confirm that relative to the wake generator pressure wave a shock is formed as the wave propagates upstream on the wake generator upper surface. The loss produced on the wake generator upper surface is a consequence of the entropy rise across the shock wave. The blade-row interaction loss predicted by MSU-TURBO is likely a conservative estimate because the pressure wave is weaker than that measured experimentally and does not propagate as far upstream as the Kulite measurements suggested. The wake generator pressure wave velocity,  $V_{\text{wave}}$ , was also higher in the experiment than that predicted numerically.

### **Spanwise Extent of Loss Production**

Having determined how the wake generator and rotor flow fields interact at 75% span to produce additional loss at close spacing, it is logical to investigate this phenomenon over the entire span. Since the extra loss produced is dependent on the presence of a shock wave at close spacing the majority of the span would be expected to produce the loss. From reference [18] the sonic radius of the SMI rotor is approximately 25% span. Figure 56 presents six time-steps from the movie 24wg\_close\_pitch2\_movie.avi. This movie shows the unsteady flow field in the pitchwise plane at 93.74% wake generator chord. The view is from downstream looking up and the analysis will focus on the middle wake generator.

Initially at time-step 1 the loss from the upper surface of the wake generator blade is seen on the right side of the wake generator. The loss region is defined by a higher magnitude loss than the freestream that is not part of the endwall or tip clearance losses. The loss is nearly two-dimensional and extends from 32% to 86% span and 12% to 18% wake generator pitch. Above 90% span and below 10% span the endwall losses exist and change very little with time. Below 3% pitch profile losses are always evident and are also independent of time.

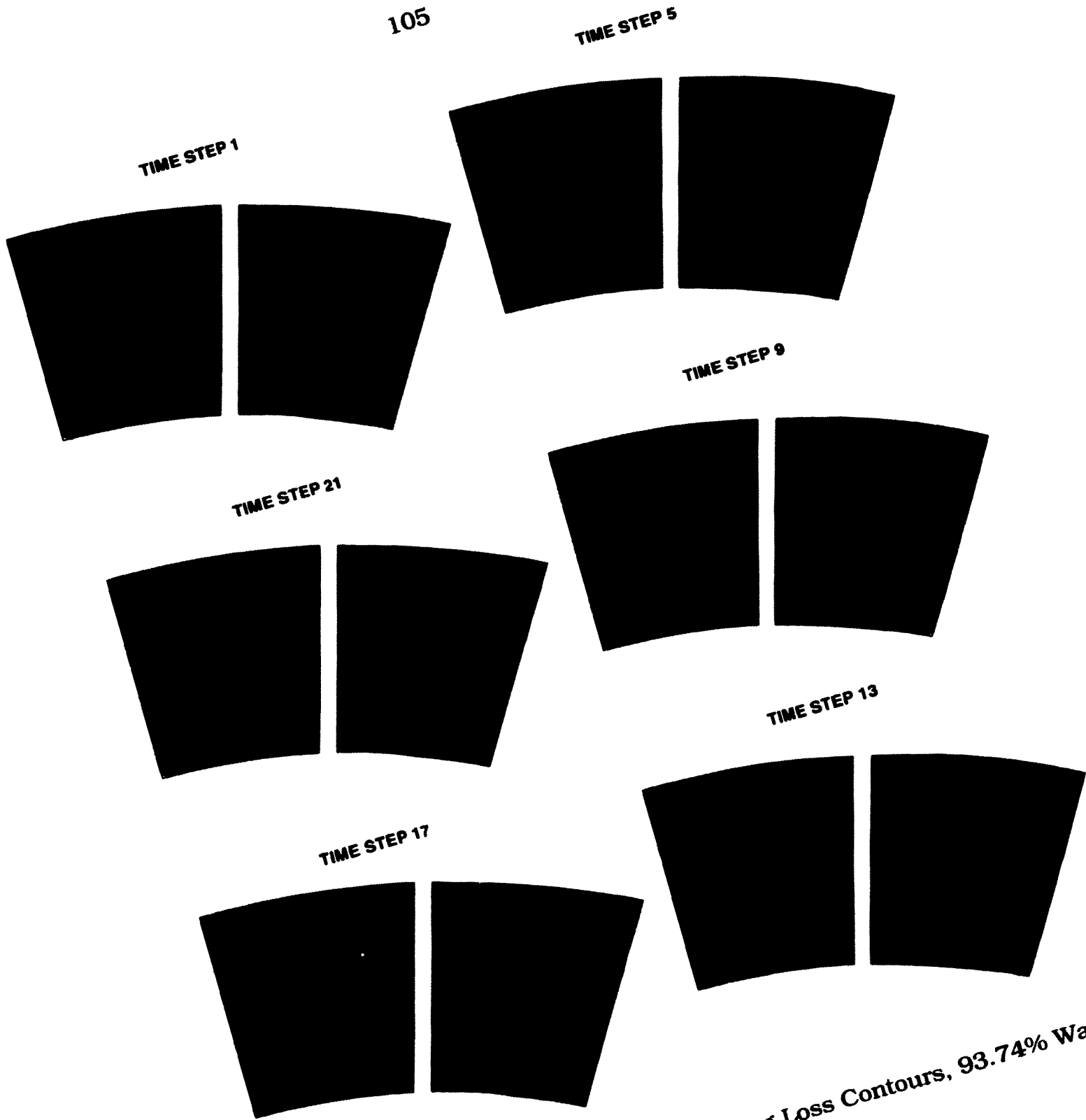


Figure 56. MSU-TURBO Close Spacing Loss Contours, 93.74% Wake Generator Chord

From time-steps 1-4 the loss region moves up towards the case. At time-step 3 the loss magnitude increases at 80% span near the blade surface and grows toward the case by time-step 4. By time-step 5 this higher loss region starts to diminish and the magnitude of the loss region is constant by time-step 6. At time-steps 5-6 the loss region is narrower but longer. At time-step 5 the loss is located between 39% and 87% span and from 5% to 14% pitch.

During time-steps 7-8 the loss region thickens and is nearly constant in thickness from 28% span to 95% span. From time-steps 9-11 the loss region continues to thicken in the pitchwise direction and moves toward the case. At time-step 9 the loss extends from 29% to 88% span and 6% to 13% pitch. Between time-steps 12-15 the loss region narrows and its spanwise extent shrinks. At time-step 13 the loss region covers 48% to 88% span and 5% to 16% pitch. At time-step 16 the loss region near the wake generator tip continues to diminish but a new loss bubble begins to form at 28% span.

During time-steps 17-18 this new loss region nearer the hub grows in width and by time-step 18 the loss near the tip is no longer present. At time-step 17 the loss region covers 19% to 42% span and its width extends from 4% to 11% pitch. Between time-steps 19-20 the new loss region continues to grow in length and move up the span of the wake generator blade.

This analysis shows that losses from the blade-row interaction exist from as low as 19% span all the way to the blade tip. Depending on the position of the rotor blade in time, the loss region varies. Two observations explain this phenomena. The first is that the relative Mach number of the flow decreases with span. Thus at lower spans the wake generator pressure wave formed when the rotor bow shock is chopped may not be as strong as at higher spans (higher relative Mach number). If the pressure wave is weaker to start off with it will not propagate as far upstream and will thus produce less loss. Furthermore the stagger angle of the rotor blade changes

with span. Figure 57 plots the rotor blade profile at 29% span and 75% span. At 29% span the rotor blade is staggered less than at 75% span. A bow shock at 29% span will therefore interact with the wake generator sooner than the bow shock at 75% span. Thus at time-step 17 only a small loss area results from the blade row interaction because the wake generator pressure wave at higher spans are not strong enough to produce loss at that time. Similarly the pressure wave may not exist on the wake generator blade surface over all spans at the same time. In other words, since the wake generator will chop the bow shock at different times, the pressure wave formed at different spans will not be in phase with each other. Furthermore, since the wake generator pressure wave strength varies with span, loss produced by the pressure wave will not extend upstream along the wake generator trailing edge the same amount.

### **29% Span Analysis**

The movies 24wg\_close\_29\_movie.avi and 24wg\_close\_29\_p\_movie.avi in Appendix C show the loss and static pressure contours at 29% span. Twenty nine percent span was chosen as it is the location at which the initial loss bubble (Figure 56, time-step 17) forms. Figure 58 presents loss and static pressure results at 29% span for three time-steps. Inspection of

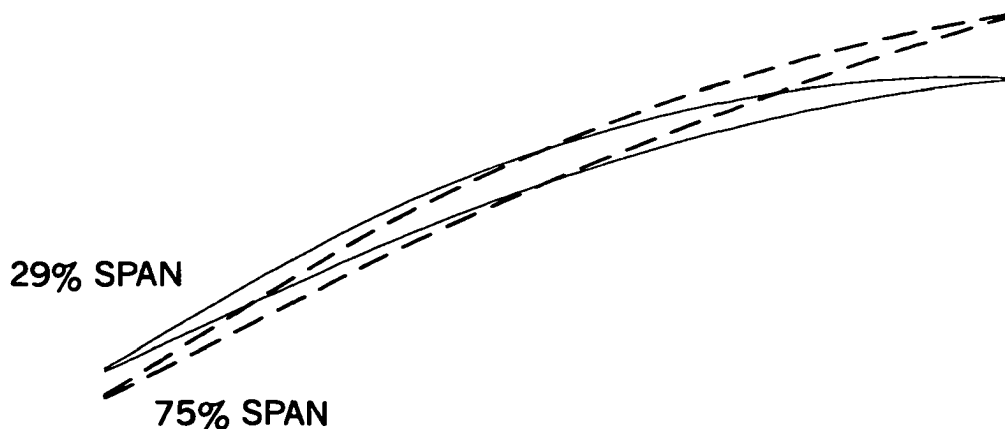


**Figure 57. SMI Rotor Blade Profile at 29% Span and 75% Span**

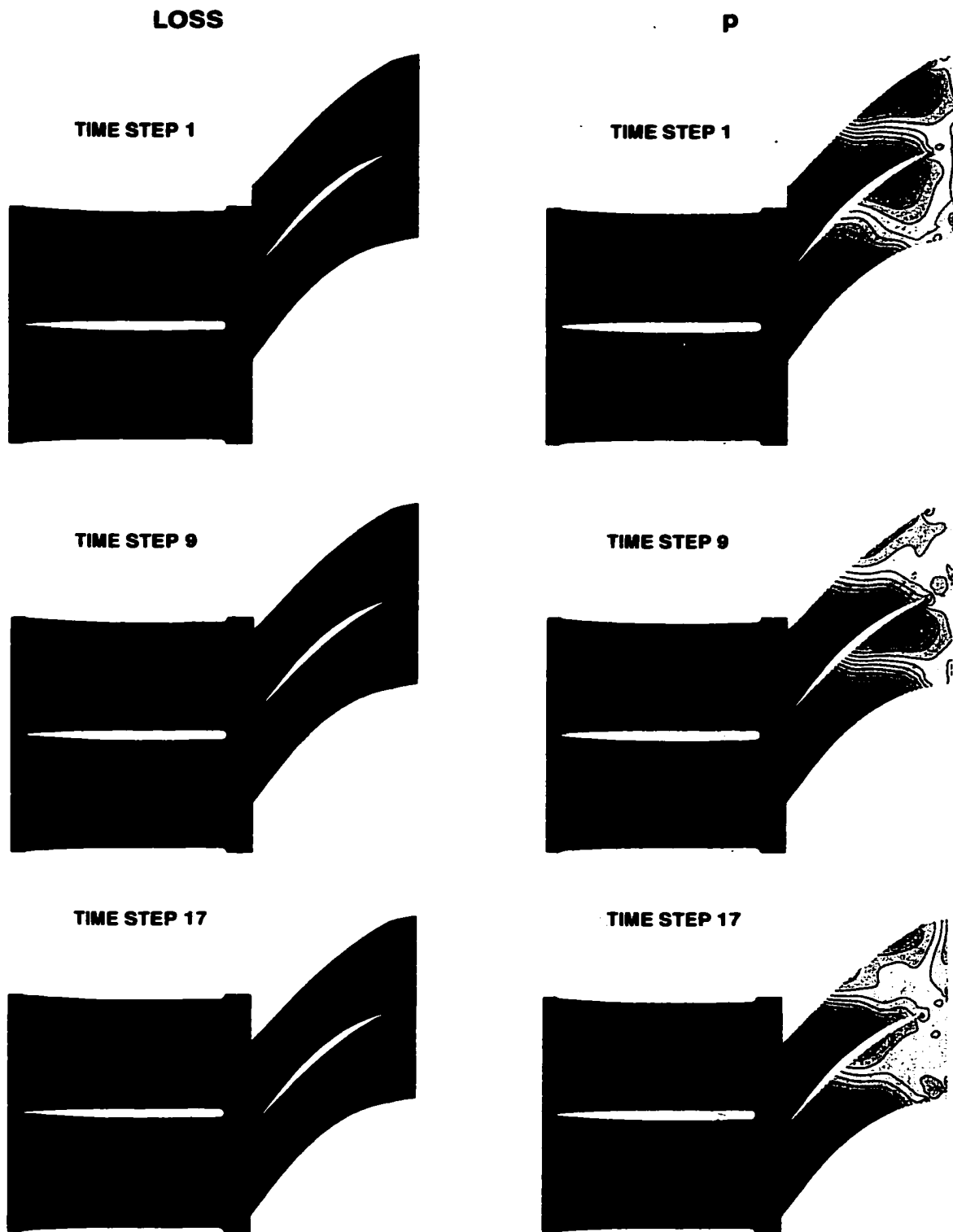


Figure 58. MSU-TURBO Loss and Static Pressure Contours at 29% Span

the loss contours reveals the effects from the bow shock are still present near the rotor blade leading edge. At time step 1 there exists a small loss peak at the wake generator trailing edge. This loss propagates forward a small distance before disappearing by time-step 8. At time-step 5 a loss peak forms downstream of the wake generator trailing edge. It moves forward on the wake generator upper surface until time-step 20 when the peak reaches 88% wake generator chord. The loss region is largest between time-steps 15-18 and extends into the blade pitch 12%. Compared to the loss results at 75% span the loss peaks are not as large and the loss region does not convect downstream above the wake generator and wake boundary.

Analysis of the static pressure contours at 29% span shows the bow shock and passage shock are not narrow and appear more like a potential field. At time-step 1 the three islands observed at 75% span are visible but they are weaker. The leading low pressure region moves forward in time and weakens significantly by time-step 8. The high pressure region at the wake generator trailing edge at time-step 1 also propagates forward eventually dissipating by time-step 9. A wake generator pressure wave is not well defined between time-steps 1-8 and thus the corresponding loss on the wake generator upper surface is very small. The bow shock is chopped by the wake generator trailing edge between time-steps 8-16. Because the bow wave is wider than at 75% span, it takes more time-steps for it to be completely chopped. An interesting observation is that starting with time-step 5 the interaction of the bow shock with the wake generator causes the bow shock to change shape. A pressure wave forms on the wake generator upper surface at time-step 12. It propagates forward and weakens by time-step 20. The pressure wave formed by the middle rotor produced the loss peak observed between time-steps 8-20.

At 29% span the interaction between the wake generator and rotor is still present although not as much loss is produced as at 75% span. The

wake generator pressure wave and the rotor bow shock chopped to produce the wave are significantly weaker than at 75% span as evidenced by fewer gradients defining the disturbance. The weak bow shock is detached a greater distance from the rotor leading edge. The wake generator pressure wave still orients itself normal to the wake generator upper surface as at 75% span. The low pressure region and expansion zone behind the bow wave are very clear.

Taken together, the loss and static pressure results of 75% and 29% span suggest that the magnitude of loss production is affected by the strength of the bow shock at the location it interacts with the trailing edge of the wake generator. Recall also in Figure 56, time-step 5 that the loss magnitude increased above 80% span. Thus at lower spans where the bow shock is weak less loss is produced while at higher spans where a stronger bow shock is present more loss is created.

### **Design Implications**

Based on the experimental and numerical results presented here and the previous chapter, a loss producing mechanism between a stator and transonic rotor has been described and validated for the SMI rig. This new discovery of a rotor bow shock being chopped by an upstream stator to form a moving shock wave on the stator suction surface has not been previously published. As demonstrated by the SMI rig this blade-row interaction has a significant effect on the performance of the compressor stage.

General principles that apply to transonic stator-rotor design can be suggested based on the insight gained from this research effort. The loss produced is a function of the properties of the wake generator pressure wave. For a moving wave the ratio of downstream to upstream static pressure is the major parameter governing change in fluid properties across the wave, including entropy. Based on the equation presented previously defining the Mach number of the pressure wave in the relative frame, the velocity and speed of sound upstream of the wave along with the

propagation velocity of the wave define the wave strength. Thus higher velocity and lower speed of sound upstream of the moving wave, and higher pressure wave propagation velocity will all increase the pressure wave strength. To minimize the interaction loss the ideal stator blade would create lower velocity and higher speed of sound conditions upstream of the propagating wave.

The strength of the wake generator pressure wave is directly related to the strength of the rotor bow shock at the location it interacts with the wake generator trailing edge. Factors that affect this are the spacing between blade-rows, the bow shock strength, and its orientation.

As demonstrated with the SMI results there exists a spacing between blade-rows at which blade-row interactions are insignificant. The question naturally arises as to what spacing is sufficient to minimize loss production due to blade-row interactions. This research has shown that an axial gap is desired so that the rotor bow shock is not chopped at all or if chopped only a weak pressure wave forms that is not supersonic in the relative frame. If a strong pressure wave forms because the spacing is too close, additional loss can be produced.

The orientation of the rotor bow shock to the stator can effect the strength of the shock when the two blade-rows interact. Since the bow shock dissipates away from the rotor leading edge it may be possible to optimize the stator and rotor stagger angles so that the weaker part of the rotor bow shock interacts with the stator trailing edge.

Returning to the equation for  $M_{\text{wave}}$ , it was shown that the propagation velocity,  $V_{\text{wave}}$ , was determined by the rotor rotational speed. Thus a reduction in blade speed would decrease the pressure wave propagation velocity and strength of the moving shock wave. If the pressure wave is not normal to stator blade suction surface then the bow shock angle would also affect  $V_{\text{wave}}$ . The smaller the angle between the stator blade and bow shock the higher the propagation velocity would be. The angle of the moving wave

affects the magnitude of the loss production as an oblique shock generates less loss than a normal shock. For the SMI rig the pressure wave was oriented normal to the blade surface however a cambered stator may be oriented differently.

The operating point of the compressor stage could have an effect on the strength of the chopped pressure wave. Higher back-pressure would cause the bow shock to detach further from the rotor leading edge putting it closer to the upstream blade-row. Perhaps balancing this out, the velocity upstream of the wave,  $V_\infty$ , is also affected by the operating condition. Once the stage is unchoked,  $V_\infty$  could decrease with increased back-pressure. Based on the SMI performance characteristics the operating point affected the interaction only slightly.

The number of stator and rotor blades and the pitch ratio of both blade rows will determine how much loss is produced by the blade-row interaction. Obviously the more interactions that occur between blade-rows the greater the overall loss due to this phenomena. The higher the blade solidity the more loss is produced. In addition, as shown in the 24 wake generator, close spacing simulation, it is possible to have multiple pressure waves on the stator blade suction surface if the solidity of the rotor blade-row is greater than the solidity of the stator blade-row.

### **Additional Research**

To better understand this loss production mechanism some suggestions for supplementary research are provided. There remains a substantial amount of research that can be accomplished with additional MSU-TURBO simulations of the SMI rig. These simulations should be run with a finer grid to better resolve the details of the shocks and pressure waves. An analytical calculation suggests that at 85%  $N_c$  the SMI rotor is subsonic for the entire span. A numerical simulation at this speed and close spacing would show if the wake generator could chop the rotor potential wave and produce a moving shock. Under certain conditions a

pressure wave may form even if a rotor bow shock is not present. The absence of loss production on the wake generator upper surface at 85%  $N_c$  would explain why the experimental data at that speed (Figure 29) showed little change in performance with blade-row spacing.

A very important piece of research to be accomplished is the comparison of MSU-TURBO solutions with the DPIV data that have been acquired [28, 32-34]. The unsteady kinematic flow field obtained with DPIV is a rare data set available for comparison and validation of time-accurate CFD codes capable of modeling blade-row interactions. Furthermore, by comparing the numerical simulations with DPIV data at various spacings and operating conditions, it would be possible to study how blade-row interactions affect wake fluid dynamics.

This research has identified the most significant factor that produces additional loss at close spacing, but others may exist. The MSU-TURBO simulations can be studied in greater detail to determine if there exist other loss sources in addition to the shock-blade interaction, such as passage shock motion, that contributes to the overall stage loss.

Finally, experimental results presented in the Steady-State Data Analysis section suggested that the efficiency at the tip actually increased at close spacing. The MSU-TURBO solutions should be analyzed to try and explain this observation.

This research program has proved the existence of a loss producing mechanism resulting from blade-row interactions. It is now important to investigate this interaction with more realistic hardware, i.e., a cambered stator. The process of the rotor bow shock being chopped and forming a pressure wave on the upstream blade-row would still occur with a cambered stator. The question is how a loaded stator will affect the propagation of the pressure wave and will the magnitude of loss produced be different. A few options are available to try and answer these questions. One possibility is to modify the SMI wake generators to better simulate a loaded stator and

this is being investigated. It would be helpful to duplicate the SMI test with more realistic stator hardware. However, the cost and complexity of building a transonic research compressor with variable spacing makes this unlikely. A numerical study may accomplish the same thing, as it is possible to model an existing multistage fan or compressor and change the spacing in the numerical simulation.

As reference [30] has shown a shock wave interacting with a blade row can also cause boundary layer separation. While not observed for the SMI rig it is still a possibility in other transonic compressors. It is not known how boundary layer separation would affect the propagation of a pressure wave on the stator suction surface.

If this phenomenon is found to exist in other hardware it would be important to understand how to design the stator or rotor to try and minimize the loss produced when the bow shock interacts with the stator trailing edge. Some ideas were discussed previously in this chapter. To test these ideas an experimental or numerical simulation should be undertaken with the objective of varying the bow shock strength and angle and the stator trailing edge geometry to determine if the loss production could be reduced without sacrificing performance and operability.

Finally, an important question to be answered is what level of design tool is necessary in order to account for blade-row interactions in the design process of transonic fans and compressors. A time accurate viscous simulation such as MSU-TURBO takes too much time to be used during aerodynamic design iterations. However, models such as APNASA that model deterministic stresses are used today in the design cycle. Research has been started to compare the time-average MSU-TURBO solutions with APNASA solutions to see if the deterministic models in APNASA can account for the blade-row interaction loss observed with the SMI rig.

## **CONCLUSIONS**

**The effect of stator-rotor blade-row interactions on the performance of a transonic compressor stage using both experimental measurements and time-accurate computational simulations has been investigated. Conclusions based on analysis of the experimental and numerical results are now presented.**

**Experimental results from the SMI and wake generator/rotor only tests document that the spacing between an upstream stator and downstream transonic rotor has a significant effect on stage performance. Mass flow rate, pressure ratio, and efficiency all decreased as the spacing between the wake generator and rotor was reduced. For the 40 wake generator configuration, 100%  $N_c$ , reductions as much as 3.29% in pressure ratio and 1.26 points efficiency were observed as spacing was changed from far to close. The number of blades in the wake generator blade-row also affected the stage performance. The higher the wake generator blade-row solidity the lower the pressure ratio and efficiency. This performance reduction was evident throughout the flow range of the pressure ratio and efficiency characteristics. Performance reduction with decreased spacing was most evident at design speed. As the corrected speed was reduced to 85% and 70%  $N_c$ , the difference in performance with changes in blade-row spacing became insignificant.**

**The flow capacity experiment of Chriss et al [21] revealed that loss in addition to wake mixing loss is present when the blade-rows are close together. Analysis of the CTA rake measurements made downstream of the rotor suggested that the increased loss was a result of blade-row interactions between the wake generator blade-row and transonic rotor blade-row.**

**To determine the blade-row interaction mechanism responsible for the increased loss production unsteady CFD simulations were carried out using**

MSU-TURBO for the 24 wake generator configuration at close and far spacings. The MSU-TURBO model was able to account for the change in efficiency observed experimentally between far and close spacing at an operating point near peak efficiency. The numerical simulations confirmed that additional loss was produced between blade-rows at close spacing and that this additional loss was produced at the wake generator trailing edge upper surface.

Analysis of the MSU-TURBO simulations and high-response static pressure measurements acquired on the wake generator blade surface revealed the fluid dynamics of this additional loss producing mechanism. At close spacing the rotor bow shock is actually chopped by the wake generator trailing edge. The shock diffracts around the blunt trailing edge forming a pressure wave on the upper surface of the wake generator that propagates upstream until it weakens. The bow shock is oblique as it interacts with the wake generator trailing edge, but the resulting wake generator pressure wave that forms is oriented normal to the wake generator blade surface. In the reference frame relative to the wake generator pressure wave, the flow is supersonic and a moving shock wave exists that produces an entropy rise. At far spacing the rotor bow shock has degenerated into a bow wave where it interacts with the wake generator trailing edge and is not chopped, therefore no pressure wave forms on the wake generator upper surface. The lower efficiency, pressure ratio, and mass flow rate measured in the close spacing configuration compared to the far spacing configuration is a result of this extra loss.

This analysis shows that additional loss generation from the blade-row interaction exist from as low as 19% span all the way to the blade tip. The magnitude of loss production is affected by the strength of the bow shock at the location it interacts with the trailing edge of the wake generator. At lower spans where the bow shock is weak, less additional loss

is produced while at higher spans where a stronger bow shock is present more additional loss is suffered.

The research has revealed a new loss producing mechanism that has a significant effect on stage performance and should be considered when designing transonic fans and compressors. Factors affecting the strength (and consequently loss produced) of the moving shock wave are the velocity and speed of sound near the stator suction surface upstream of the propagating wave, blade-row spacing, and rotor bow shock strength. Lower velocity and higher speed of sound conditions upstream of the propagating wave would decrease the strength of the moving wave. An axial gap is desired so that the rotor bow shock is not chopped at all or if chopped only a weak pressure wave forms that is not supersonic in the relative frame. Orienting the stator and rotor stagger angles so that the weaker part of the rotor bow shock interacts with the stator trailing edge would also reduce loss production. Finally, the number of stator and rotor blades and the pitch ratio of both blade-rows will determine how much loss is produced by this blade-row interaction. The higher the blade solidity the more loss is produced due to this phenomenon.

There still remains some important research to be done. Additional simulations using MSU-TURBO with finer meshes should be compared to the available DPIV data set. There exists very little data suitable for comparison and validation of time-accurate CFD codes capable of modeling blade-row interactions. More and more research is being undertaken with unsteady Navier-Stokes codes but there is not enough understanding of how accurate a code is or what its limitations are.

Future efforts should focus on investigating the impact of a pressure wave chopped from a rotor bow shock on a loaded upstream stator. This can be done numerically or experimentally. Experimental research should be undertaken to understand how to design the stator or rotor to try and minimize the additional loss produced when the rotor bow shock interacts

**with the stator trailing edge. The comparison of APNASA steady simulations to the MSU-TURBO time accurate simulations will demonstrate whether deterministic stress models in APNASA are sufficient to account for the transonic stator-rotor interactions presented in this report.**

**APPENDIX A. CTA RAKE DRAWINGS**





**APPENDIX B. 24 WAKE GENERATOR PERFORMANCE PROFILES**

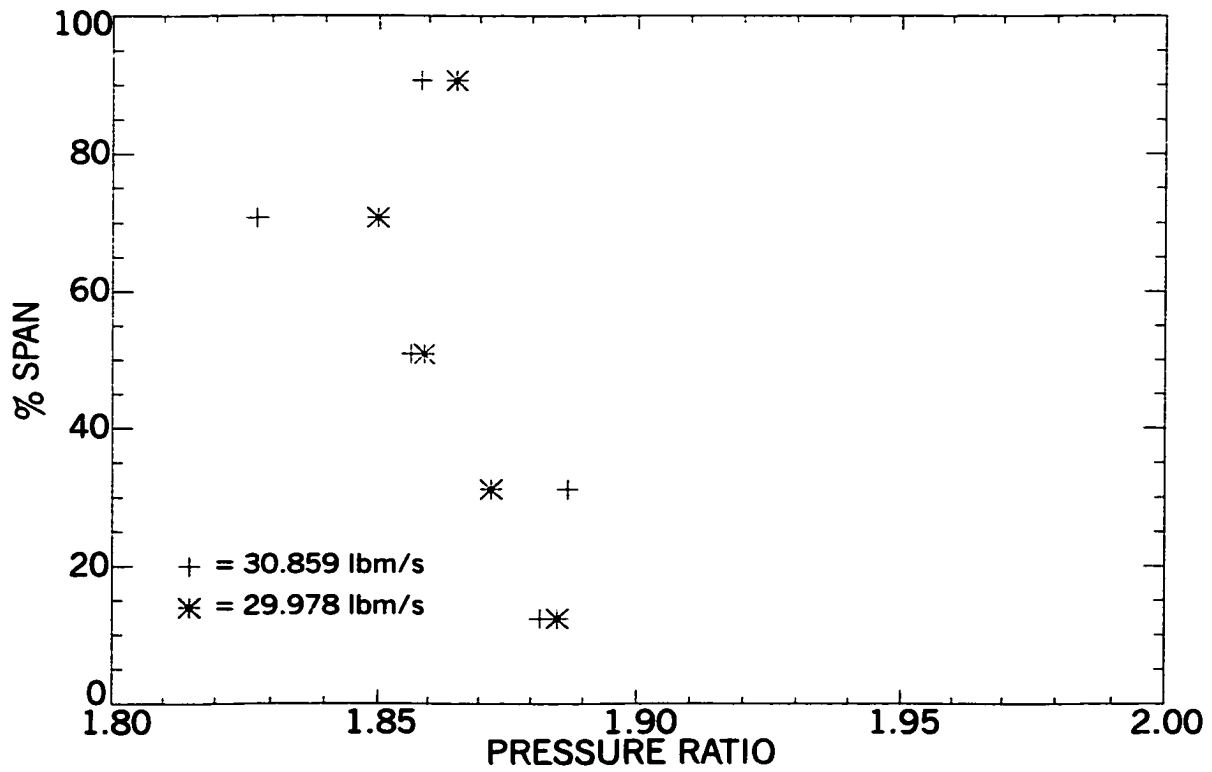
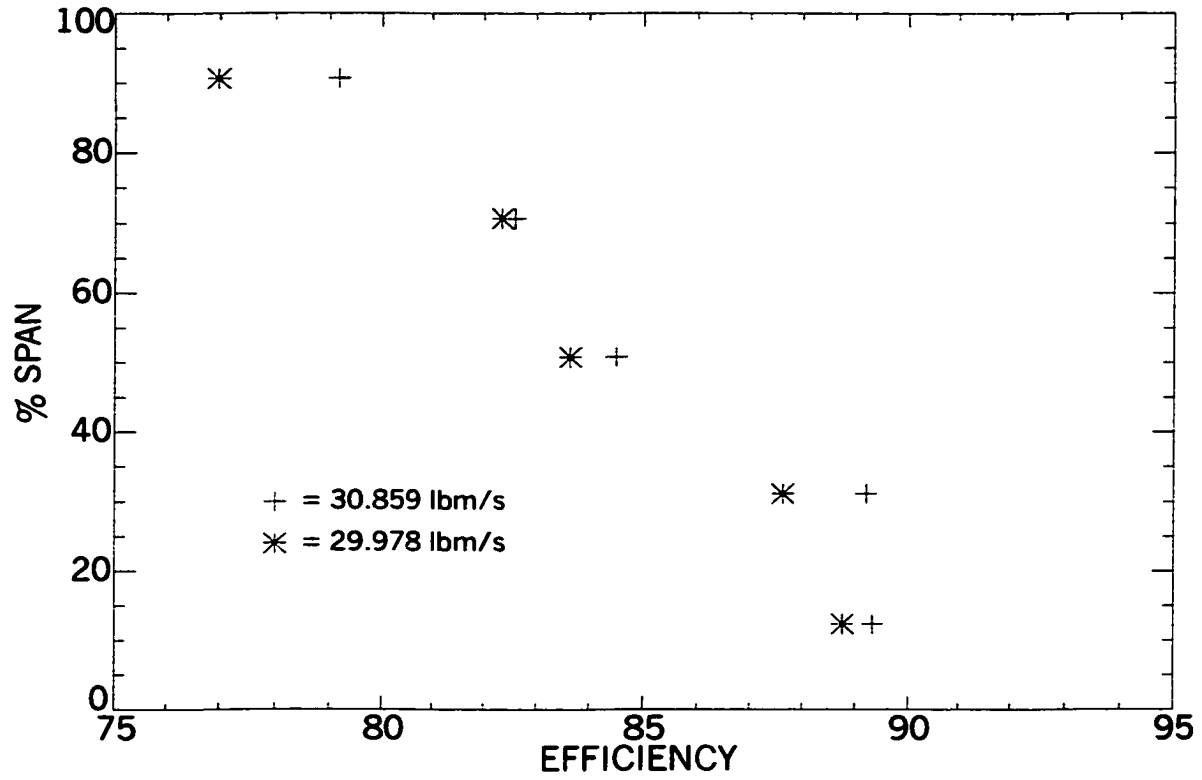


Figure 61. 24 Wake Generator Performance Profiles at Close Spacing

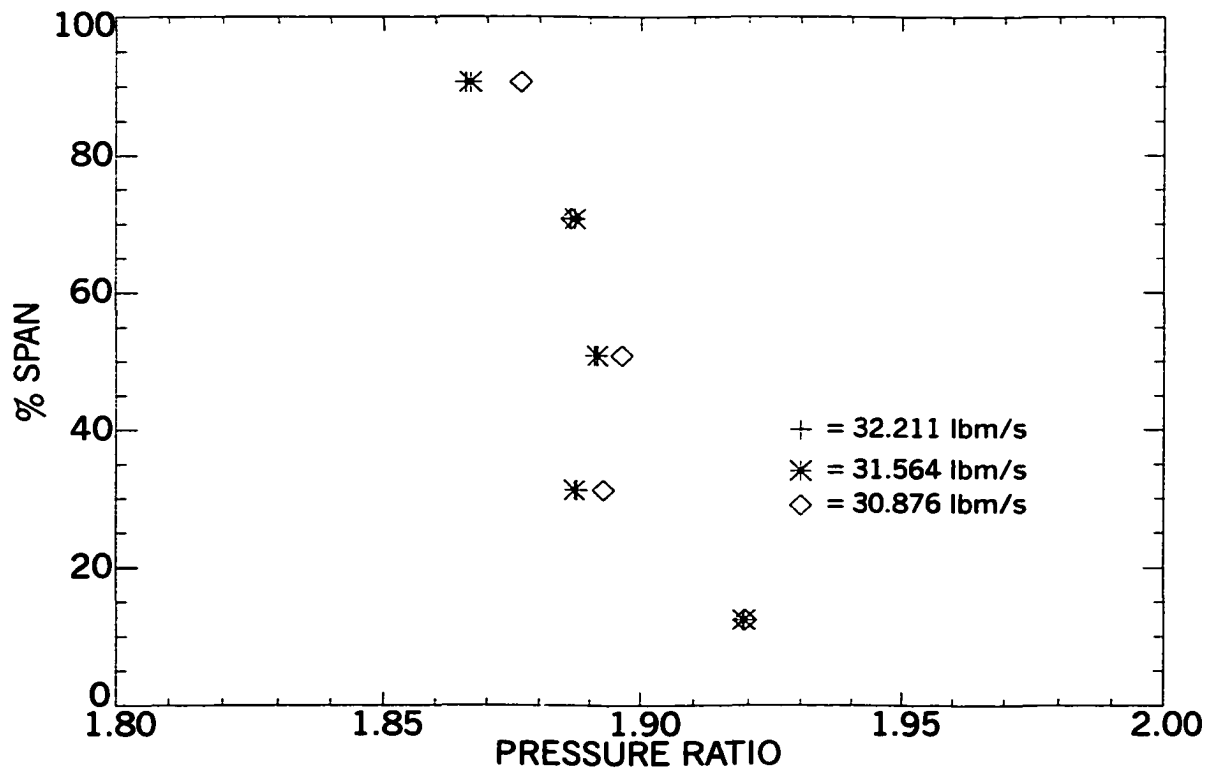
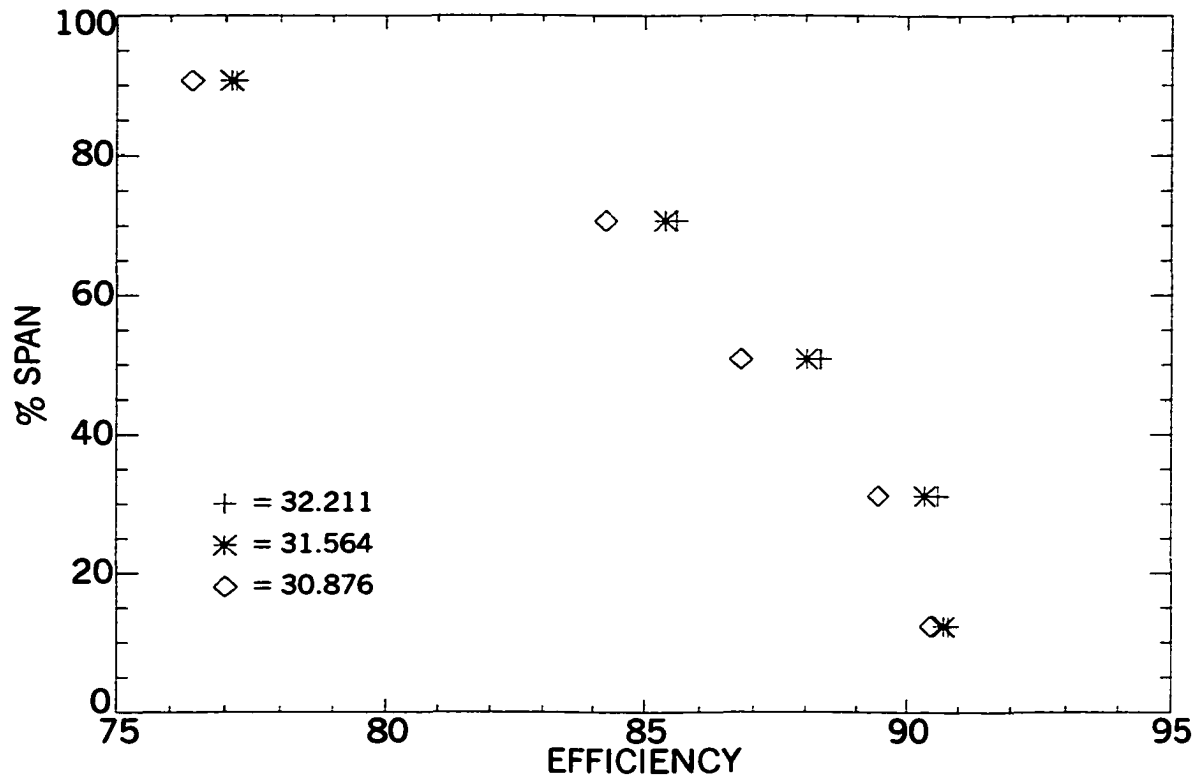


Figure 62. 24 Wake Generator Performance Profiles at Far Spacing

**APPENDIX C. MOVIES COLOR FIGURES FROM MSU-TURBO  
SIMULATIONS**

**System requirements for computer disks: Windows, Apple or UNIX-based systems with software that supports AVI video format and reads Word 8 documents; Windows 98 or higher; Windows Media Play Version 7 or higher.**

**CD-R Containing avi Files of MSU-TURBO Simulations**

<b>24wg_close_29_p_movie.avi</b>	<b>static pressure contours, close spacing, 29% span</b>
<b>24wg_close_29_movie.avi</b>	<b>loss contours, close spacing, 29% span</b>
<b>24wg_close_movie.avi</b>	<b>loss contours, close spacing, 75% span</b>
<b>24wg_close_p_movie.avi</b>	<b>static pressure contours, close spacing, 75% span</b>
<b>24wg_close_pitch2_movie.avi</b>	<b>loss contours, close spacing, 93.74% wake generator chord</b>
<b>24wg_far_movie.avi</b>	<b>loss contours, far spacing, 75% span</b>
<b>24wg_far_p_movie.avi</b>	<b>static pressure contours, far spacing, 75% span</b>

**CDR Containing Microsoft Word 97 Document of Color Figures From MSU-TURBO Simulations**

**Figure 47. MSU-TURBO Flow Field Loss Comparison, 75% Span, Time-Step 5**

**Figure 48. MSU-TURBO Close Spacing Loss Contours, 75% Span**

**Figure 49. MSU-TURBO Far Spacing Loss Contours, 75% Span**

**Figure 50. MSU-TURBO Static Pressure Comparison, 75% Span, Time-Step 5**

**Figure 51. MSU-TURBO Close Spacing Static Pressure Contours, 75% Span**

**Figure 52. MSU-TURBO Far Spacing Static Pressure Contours, 75% Span**

**Figure 56. MSU-TURBO Close Spacing Loss Contours, 93.74% Wake Generator Chord**

**Figure 58. MSU-TURBO Loss and Static Pressure Contours at 29% Span**

**REFERENCES**

- [1] Adamczyk, J. J., 1985, "Model Equation for Simulating Flows in Multistage Turbomachines," ASME paper 85-GT-226.
- [2] Adamczyk, J. J., 2000, "Aerodynamic Analysis of Multistage Turbomachinery Flows in Support of Aerodynamic Design," ASME Journal of Turbomachinery, **122**, pp. 189-217.
- [3] Smith, L. H., 1970, "Casing Boundary Layers in Multistage Axial Flow Compressors," *Flow Research in Blading*, edited by L. S. Dzung, Elsevier Publishing Company, Amsterdam.
- [4] Mikolajczak, A. A., 1976, "The Practical Importance of Unsteady Flow," AGARD CP 177, *Unsteady Flow Phenomena in Turbomachinery*.
- [5] Smith, L. H., 1966, "Wake Dispersion in Turbomachines," ASME Journal of Basic Engineering, Series D, No. 3, pp. 688-690.
- [6] Smith, L. H., 1993, "Wake Ingestion Propulsion Benefit," AIAA Journal of Propulsion and Power, **9**, No. 1, pp. 74-82.
- [7] Deregai, P., and Tan, C. S., 1996, "Impact of Rotor Wakes on Steady-State Axial Compressor Performance," ASME paper 96-GT-253.
- [8] Adamczyk, J. J., 1996, "Wake Mixing in Axial Flow Compressors," ASME paper 96-GT-29.
- [9] Van Zante, D. E., Adamczyk, J. J., Strazisar, A. J., and Okiishi, T. H., 1997, "Wake Recovery Performance Benefit in a High-Speed Axial Compressor," ASME paper 97-GT-535.
- [10] van de Wall, A. G., Kadambi, J. R., and Adamcayk, J. J., 2000, "A Transport Model for the Deterministic Stresses Associated With Turbomachinery Blade Row Interactions," ASME Journal of Turbomachinery, **122**, pp. 593-603.
- [11] Rose, M. G., and Harvey, N. W., 2000, "Turbomachinery Wakes: Differential Work and Mixing Losses," ASME Journal of Turbomachinery, **122**, pp. 68-77.
- [12] Ottavy, X, Trebinjac, I., and Vouillarmet, A., 2001, "Analysis of the Interrow Flow Field Within a Transonic Axial Compressor: Part 1 –

- Experimental Investigation," *ASME Journal of Turbomachinery*, **123**, pp. 49-56.
- [13] Ottavy, X, Trebinjac, I., and Vouillarmet, A., 2001, "Analysis of the Interrow Flow Field Within a Transonic Axial Compressor: Part 2 – Unsteady Flow Analysis," *ASME Journal of Turbomachinery*, **123**, pp. 57-63.
- [14] Sanders, A. J., and Fleeter, S., 1999, "Transonic Rotor-IGV Interactions," Presented at the thirteenth International Symposium on Air Breathing Engines, Chattanooga, TN, (ISABE 99-7029).
- [15] Liamis, N., Bacha, J. L., and Burgand, F., 1996, "Numerical Simulations of Stator-Rotor Interactions on Compressor Blade Rows" in: *Loss Mechanisms and Unsteady Flows in Turbomachines* AGARD CP-571, North Atlantic Treaty Organization.
- [16] Eulitz, F., Engel, K., and Pokorny, S., 1996, "Numerical Investigation of Inviscid and Viscous Interaction in a Transonic Compressor" in: *Loss Mechanisms and Unsteady Flows in Turbomachines* AGARD CP-571, North Atlantic Treaty Organization.
- [17] Arnone, A., and Pacciani, R., 1998, "IGV-Rotor Interaction Analysis in a Transonic Compressor Using the Navier-Stokes Equations," *ASME Journal of Turbomachinery*, **120**, pp. 147-155.
- [18] Law, C. H., and Wennerstrom, A. J., 1989, "Two Axial Compressor Designs for a Stage Matching Investigation," AFWAL-TR-89-2005.
- [19] Creason, T., and Baghdadi, S., 1988, "Design and Test of a Low Aspect Ratio Fan Stage," AIAA paper 88-2816.
- [20] 1990, *Recommended Practices for Measurement of Gas Path Pressures and Temperatures for Performance Assessment of Aircraft Turbine Engines and Components* AGARD-AR-245, edited by H. I. H Saravanamuttoo, North Atlantic Treaty Organization.
- [21] Chriss, R. M., Copenhaver, W. W., and Gorrell, S. E., 1999, "The Effects of Blade-Row Spacing on the Flow Capacity of a Transonic Rotor," ASME paper 99-GT-209.
- [22] Brookfield, J. M., Waitz, I. A., and Sell, J., 1996, "Wake Decay: Effect of Freestream Swirl," ASME paper 96-GT-495.

- [23] Raj, R., and Lakshminarayana, B., 1973, "Characteristics of the Wake Behind a Cascade of Airfoils," *Journal of Fluid Mechanics*, **61**, pp.707-730.
- [24] Stauter, R. C., Dring, R. P., and Carta, F. O., 1991, "Temporally and Spatially Resolved Flow in a Two-Stage Axial Flow Compressor: Part 1 – Experiment," *ASME Journal of Turbomachinery*, **113**, pp. 219-226.
- [22] Copenhaver, W. W., 2001, Personal Communication.
- [23] Cumpsty, N. A., 1989, *Compressor Aerodynamics*, Longman Scientific & Technical, England.
- [24] Denton, J. D., 1993, "Loss Mechanisms in Turbomachines," *ASME Journal of Turbomachinery*, **115**, pp. 621-656.
- [25] Chen, J. P., Celestina, M. L., and Adamczyk, J. J., 1994, "A New Procedure for Simulating Unsteady Flows Through Turbomachinery Blade Passages," ASME paper 94-GT-151.
- [26] Chen, J. P., and Barter, J. W., 1998, "Comparison of Time-Accurate Calculations for the Unsteady Interaction in Turbomachinery Stage," AIAA paper 98-3292.
- [27] Barter, J. W., Vitt, P. H., and Chen, J. P., 2000, "Interaction Effects in a Transonic Turbine Stage," ASME paper 2000-GT-0376.
- [28] Estevadeordal, J., Gogineni S., Goss, L., Copenhaver, W., and Gorrell, S., 2001, "DPIV Study of Wake-Rotor Synchronization in a Transonic Compressor," AIAA paper 2001-3095.
- [29] Van Zante, D. E., 2000, Personal Communication.
- [30] Delery, J, and Marvin, J. G., 1986, *Shock-Wave Boundary Layer Interactions*, AGARD-AG-280, North Atlantic Treaty Organization.
- [31] Koch, P. J, Probasco, D. P., Wolff, J. M., Copenhaver, W. W., and Chriss, R. M., 1999, "Transonic Compressor Influences on Upstream Surface Pressures with Axial Spacing," ASME paper 99-GT-385.
- [32] Estevadeordal, J., Gogineni, S., Goss, L., Copenhaver, W. and Gorrell, S., 2000, "Study of Flow-Field Interactions in a Transonic Compressor Using DPIV," AIAA paper 00-0378.

- [33] Gogineni, S., Estevadeordal, J., Copenhaver, W., and Gorrell, S., 2001, "Investigation of Wake-Shock Interactions in a Transonic Compressor Using DPIV," Presented at the fifteenth International Symposium on Air Breathing Engines, Bangalore, India, (ISABE 2001-1196).
- [34] Copenhaver, W., Estevadeordal J., Gogineni, S., Gorrell, S., and Goss, L., 2001, "DPIV Study of Near-Stall Wake-Rotor Interactions in a Transonic Compressor," Presented at the 4<sup>th</sup> International Symposium on Particle Image Velocimetry, Gottingen, Germany.